

**INVESTIGATING FORMATION AND
EVOLUTION OF Z(3) WALLS
AND FLOW ANISOTROPIES IN
RELATIVISTIC HEAVY-ION COLLISION**

By

RANJITA KUMARI MOHAPATRA

PHYS07200604027

INSTITUTE OF PHYSICS

BHUBANESWAR, INDIA

A THESIS SUBMITTED TO THE
BOARD OF STUDIES IN PHYSICAL SCIENCES
IN PARTIAL FULFILLMENT OF REQUIREMENTS
FOR THE DEGREE OF
DOCTOR OF PHILOSOPHY
OF
HOMI BHABHA NATIONAL INSTITUTE



MARCH 21, 2013

Statement by Author

This dissertation has been submitted in partial fulfillment of requirements for an advanced degree at Homi Bhabha National Institute (HBNI) and is deposited in the Library to be made available to borrowers under rules of the HBNI.

Brief quotations from this dissertation are allowable without special permission, provided that accurate acknowledgement of source is made. Requests for permission for extended quotation from or reproduction of this manuscript in whole or in part may be granted by the Competent Authority of HBNI when in his or her judgment the proposed use of the material is in the interests of scholarship. In all other instances, however, permission must be obtained from the author.

(Ranjita Kumari Mohapatra)

Declaration

I, Ranjita Kumari Mohapatra, hereby declare that the investigations presented in the thesis have been carried out by me. The work is original and has not been submitted earlier as a whole or in part for a degree/diploma at this or any other Institution/University.

(Ranjita Kumari Mohapatra)

To My Family

Acknowledgements

It is a great pleasure for me to thank those people who helped me in various ways during my work here. I would like to thank my advisor, Prof. Ajit M Srivastava for his guidance and help for this thesis work. I have been inspired by his innovative thoughts and intuitive way of looking at problems in physics.

My sincere thanks to all the faculty members of the institute for their beautiful lectures, invaluable help and guidance during my stay here. It is my great pleasure to thank Prof. A. Khare, Prof. S.C. Phatak, Prof. A.M. Jayannavar, Prof. P. Agarwal, Prof. S. Mukherjee, Prof. Alok Kumar, Prof S. Verma, Prof. S.K. Patra, Prof. P.K Sahoo and Prof G. Tripathy. I would like to take the opportunity to thank my Msc teachers Prof. N. Barik, Prof. L.P. Singh, Prof. P. Khare, Prof. N.C. Mishra, Prof. K. Maharana and Prof. S. Mohapatra for their wonderful teaching and motivating me for research.

I would like to thank Prof. Jun Takahashi for various discussions during my stay in Brasil. Its a great pleasure to thank Prof S. Digal for interesting discussions on physics. Its really great pleasure and wonderful experience to work with him. I also would like to thank Prof. R. Bhalerao, Prof. H. Mishra and Prof. B. Mohanty for nice discussions on QGP.

I would like to thank all my collaborators. My special thanks to Ananta and Umashankar for various discussion on QGP and many other branches of physics. I would like to express my hearty thanks to Ajay, Anant, Partha and Arpan for interesting discussions on physics and many other topics and providing a homely atmosphere during my stay at IOP. My sincere thanks to Trilochan, Sourabh, Sudhanwa, Sudipta, Sabita, Chitrasen, Rama, Anjishnu, Abhisek, Ambresh, Jaya, Sankha, Subrat, Jim, Sailesh and Anjan for their beautiful company and various interesting discussions.

I would like to thank all the library, administrative and computer centre staff of

this institute for their help at every stage.

Finally, its my great pleasure to thank my beloved family, whose love, affection and best understanding, have helped me a lot in different stages of my life. My deepest gratitude goes to my parents and my sisters Sabita and Rasmi for their unconditional love, and support. Its a great pleasure for me to thank my husband for all his love, moral support and best understanding.

Date:

Ranjita Kumari Mohapatra

Contents

Statement by Author	ii
Declaration	iii
Acknowledgements	v
Synopsis	1
List of Publications/Preprints	6
1 Introduction	8
1.1 Our Universe	8
1.2 QCD Phase Transition	13
1.3 Space-time Evolution of QGP in RHICE	16
1.3.1 Bjorken's Longitudinal Boost Invariance	19
1.3.2 Transverse Expansion	21
1.4 Signatures of QGP, a brief discussion	23
1.5 Outline of the Thesis	26
2 Phase Transition and Topological Defects	28
2.1 Introduction	28
2.1.1 Spontaneous Symmetry Breaking	32
2.1.2 First Order Phase Transition	34
2.1.3 False Vacuum Decay	35
2.1.4 Thin-Wall Approximation	36
2.1.5 Thick wall calculation	39

2.1.6	Finite Temperature Effect on False Vacuum Decay	39
2.2	Topological Defects	40
2.2.1	Kibble Mechanism	41
2.2.2	Domain Wall	42
2.2.3	String	44
2.3	Z(N) Symmetry, Polyakov Loop, Domain walls and Strings	46
3	Simulation of Z(3) Walls and Strings in a First Order Quark-Hadron Transition	51
3.1	Introduction	51
3.2	The Effective Potential	54
3.3	Domain Wall And String Formation Via Kibble Mechanism	56
3.4	Critical Bubble Profile and Nucleation Probability	59
3.5	Numerical Techniques	67
3.6	With Quarks	69
3.7	Results of the Simulation	71
3.7.1	formation and motion of extended walls	72
3.7.2	Formation and collapse of a closed wall	78
3.8	Possible experimental signatures of Z(3) walls and strings	85
4	Domain Growth and Fluctuations during Quenched Transition to QGP in Relativistic Heavy-ion Collisions	89
4.1	Introduction	89
4.2	Effective Potential Based on Polyakov Loop	93
4.3	Numerical Simulation	94
4.4	Bubble like Structures during Quench	98
4.5	Strong Explicit Symmetry Breaking and Large Field Oscillations	100
4.6	Effects of Large l Oscillations on Flow Anisotropy	103
5	Bubble Formation During Spinodal Decomposition in Heavy-Ion Collisions	112
5.1	Introduction	112
5.2	Effective Potential	114

5.3	Numerical Techniques	115
5.4	Bubble Formation during Spinodal Decomposition	115
5.5	Results	119
5.5.1	Bubble formation in heavy-ion collision	120
5.5.2	(ii) Bubble formation in general potentials	122
5.6	Discussion	123
6	Analyzing Elliptic Flow Anisotropy with Excursion Sets in Relativistic Heavy-Ion Collisions	127
6.1	Introduction	127
6.2	Different methods to measure elliptic flow anisotropy	129
6.2.1	Event Plane Method	129
6.2.2	Particle Correlation Method	130
6.3	Our method: Construction of Excursion Sets	130
6.4	Results	132
6.4.1	Determination of Event Plane	135
6.5	Discussion	136
7	Summary	140

Synopsis

It is believed that there exists a new state of matter called “Quark Gluon Plasma” (QGP) at very high temperature or high baryon density. Due to asymptotic freedom in QCD, quarks and gluons are deconfined in this state. It is believed that Universe existed in this state when it was few microseconds old. Search for the QGP at relativistic heavy-ion collision experiments (RHICE) has reached a very exciting stage with the ongoing experiments at Relativistic Heavy-Ion Collider (RHIC) and the Large Hadron Collider (LHC) [1]. Another important aim of these experiments is to study dynamical details of the quark-hadron phase transition. No one doubts that the QGP phase has already been created at RHIC but conclusive evidence for the same is still lacking. Many signatures have been proposed for the detection of the transient QGP phase and these have been thoroughly investigated both theoretically and experimentally. Along with continued investigation of these important signatures of QGP, there is a need for investigating novel signals exploring qualitatively non-trivial features of the QGP phase.

The theory of strong interaction in between quarks and gluons is described by $SU(3)$ color gauge symmetry. $SU(3)$ pure gauge theory, without dynamical quarks, has $Z(3)$ global symmetry which is restored below T_c in the confined phase and spontaneously broken in the deconfined phase giving rise to three degenerate vacua. Topological defects are inevitably produced in this symmetry breaking phase transitions. These defects are localized regions in which the system is locked in symmetric phase while the whole system is in symmetry broken phase. The formation of different types of topological objects depends upon the vacuum manifold. In confinement-deconfinement phase transition, $Z(3)$ domain walls and the QGP strings (forming at the junctions of three $Z(3)$ walls) are produced. Since, it is the topology of the vacuum manifold which determines the formation of defects, formation of these defects shows

certain universal features, independent of the symmetry breaking scale or, the detailed dynamics of the phase transition. Domain walls, cosmic strings and monopoles are some of the topological defects that could have been formed during the cosmological phase transitions. Among these defects, cosmic strings are the most thoroughly studied defect because of its various important cosmological and astrophysical consequences. Also, there are different examples of topological defects in condensed matter systems like flux tubes in Type II superconductor, vortex line in superfluid Helium and line defects in liquid crystals. Kibble proposed a mechanism for the production of topological defects in the context of early universe [2]. Subsequently it was realized that this mechanism is applicable to any spontaneous symmetry breaking phase transition. We study the formation of defects via this mechanism in confinement-deconfinement phase transition in RHICE where $Z(3)$ symmetry is spontaneously broken. These defects can lead to non-trivial consequences in heavy-ion collisions.

The expectation value of Polyakov loop $l(x)$ which is related to the free energy of an isolated heavy test quark behaves as an order parameter for confinement deconfinement phase transition. This order parameter transforms non-trivially under $Z(3)$ symmetry and thus gives rise to 3 degenerate vacua in the high temperature phase of $SU(3)$ gauge theory. Using an effective potential based on Polyakov loop order parameter for QCD proposed by Pisarski [3], we carry out numerical simulations of the evolution of $Z(3)$ walls and strings in RHICE in a first order phase transition. It is known that quark-hadron transition is likely to be a first order transition at large values of baryon chemical potential. Our results are then applicable to such situations, e.g. high baryon density, low energy heavy-ion collisions. Further, as emphasized above, due to universal features of topological defect network produced in a phase transition, even for low values of chemical potential (as for ultra-relativistic heavy-ion collisions at RHIC and LHC) where the transition is expected to be a cross-over, our results of first order transition may capture qualitative features of defect production.

Since strong elliptic flow at RHIC hints towards early thermalisation, the phase transition may not be an equilibrium transition but more likely a quench. During this quench also where the transition proceeds via spinodal decomposition, these defects are produced. We further see bubble like structure in this spinodal decomposition. This is a surprising result because these bubbles are produced even if there is no

meta-stable barrier for bubble nucleation between the false vacuum (confined phase) and the true vacuum (deconfined phase). This suggests a new type of phase transition dynamics which needs to be studied in greater detail.

So far we discussed the case where $Z(3)$ symmetry is spontaneously broken leading to degenerate $Z(3)$ vacua. However, real QCD involves dynamical quarks and $Z(3)$ symmetry is explicitly broken due to quarks giving rise to $\theta = 0$ being the true vacuum while the other two $Z(3)$ vacua are lifted. $l = 0$ vacuum also shifts towards nonzero value along $\theta = 0$. When the symmetry breaking is large, the Polyakov loop order parameter field rolls to the true vacuum everywhere in the system. In such a situation we find that there are huge oscillations of the field before it settles in the true vacuum. This huge oscillation of the field may affect the elliptic flow. We study this possibility and find that the elliptic flow coefficient (v_2), as well as the spatial eccentricity undergo huge oscillations in this quench scenario compared to the equilibrium transition situation. These results point out that it is important to take effect of quench induced oscillations of the order parameter field in hydrodynamical simulation to calculate elliptic flow anisotropy.

As we mentioned above, irrespective of the nature of the dynamics of the confinement-deconfinement phase transition (equilibrium, quench, first order via bubble nucleation), topological $Z(3)$ walls and associated QGP strings are always produced. There are important implications of these defects in relativistic heavy-ion collisions. Domain walls and strings melt away when the temperature drops below T_c . However, they may leave their signatures in the distribution of final particles due to large concentration of energy density in extended regions as well as nontrivial scatterings of quarks and antiquarks with these objects. Also, quarks and antiquarks have nonzero reflection coefficients when traversing across these domain walls. The collapsing domain wall will then concentrate any excess baryon number enclosed, leading to formation of baryon (or antibaryon) rich regions. Due to quark/antiquark reflection inside a collapsing wall, each reflection increases the momentum of the enclosed particle. This leads to a specific pattern of P_T enhancement of quarks with heavy flavors. The modification of P_T spectrum of resulting hadrons can be calculated and the enhancement of heavy hadrons at high P_T can be analysed for the formation of $Z(3)$ walls. Domain walls are extended along z direction. Hence the correlation of particle production

over a large range of rapidity are expected from such extended regions. $Z(3)$ walls and strings may not only provide qualitatively new signatures for the QGP phase, but may provide the first laboratory study of such topological objects in a relativistic quantum field theory system.

Elliptic flow is one of the most important signatures of QGP [4]. Since the system thermalises locally in less than 1 fm time, there is larger pressure gradient along X-axis compared to Y-axis making larger flow along X-axis. The second Fourier coefficient of the azimuthal distribution of hadrons is known as elliptic flow coefficient. There are different methods like event plane method, particle correlation method to measure elliptic flow coefficient. Here we show that elliptic flow anisotropy in relativistic heavy-ion collisions can be analyzed using a certain technique of shape analysis of excursion sets recently proposed by us for CMBR fluctuations to investigate anisotropic expansion history of the universe [5]. The technique analyzes shapes (sizes) of patches above (below) certain threshold value for transverse energy/particle number (the excursion sets) as a function of the azimuthal angle and rapidity. Angles with maximum difference in the two distributions identify the event plane, and the magnitude of difference in the two distributions relates to the magnitude of momentum anisotropy, i.e. elliptic flow. This is an important analysis technique which quantifies the elliptic flow anisotropy.

Bibliography

- [1] J.W. Harris and B. Muller, Ann. Rev. Nucl. Part. Sci. **46**, 71 (1996), B. Muller and J.L. Nagle, Ann. Rev. Nucl. Part. Sci. **56**, 93 (2006).
- [2] T.W.B. Kibble, J. Phys. **A 9**, 1387 (1976).
- [3] R.D. Pisarski, Phys. Rev. **D 62**, 111501R (2000); *ibid*, hep-ph/0101168.
- [4] J.-Y. Ollitrault, Phys. Rev. **D 46**, 229 (1992).
- [5] R.K. Mohapatra, P.S. Saumia and A.M. Srivastava, Int. J. Mod. Phys. **A 27**, 1250144 (2012).

List of Publications/Preprints

- [1] “Super-horizon fluctuations and acoustic oscillations in relativistic heavy-ion collisions”, A.P. Mishra, R.K. Mohapatra, P.S. Saumia and A.M. Srivastava; *Phys. Rev. C* **77**, 064902 (2008).
- [2] “Using CMBR analysis tools for flow anisotropies in relativistic heavy-ion collisions”, A.P. Mishra, R.K. Mohapatra, P.S. Saumia and A.M. Srivastava; *Phys. Rev. C* **81**, 034903 (2010).
- *[3] “Simulation of Z(3) walls and string production via bubble nucleation in a quark-hadron transition”, U.S. Gupta, R.K. Mohapatra, A.M. Srivastava and V.K. Tiwari; *Phys. Rev. D* **82**, 074020 (2010).
- [4] “Enhancement of flow anisotropies due to magnetic field in relativistic heavy-ion collisions”, R.K. Mohapatra, P.S. Saumia and A.M. Srivastava; *Mod. Phys. Lett. A* **26**, 2477 (2011).
- *[5] “Analyzing flow anisotropies with excursion sets in heavy-ion collisions”, R.K. Mohapatra, P.S. Saumia and A.M. Srivastava; *Mod. Phys. Lett. A* **27**, 1250168 (2012).
- [6] “Probing the anisotropic expansion history of the universe with cosmic microwave background”, R.K. Mohapatra, P.S. Saumia and A.M. Srivastava; *Int. J. Mod. Phys. A* **27**, 1250144 (2012).
- [7] “Effects of quarks on the formation and evolution of Z(3) walls and strings in relativistic heavy-ion collisions”, U.S. Gupta, R.K. Mohapatra, A.M. Srivastava and V.K. Tiwari; *Phys.Rev. D* **86**, 125016 (2012).

- *[8] “Domain growth and fluctuations during quenched transition to QGP in relativistic heavy-ion collisions”, R.K. Mohapatra and A.M. Srivastava; arXiv:1210.4718. (Communicated to the journal)
- *[9] “Bubble formation during spinodal decomposition in heavy-ion collisions”, S. Digal, R.K. Mohapatra; Pre-print in preparation.

Conference Proceedings

- [1] “Using CMBR tools for flow anisotropies in relativistic heavy-ion collisions”, R.K. Mohapatra, P.S. Saumia and A.M. Srivastava; **Nucl. Phys. A** **862**, 283-285 (2011).
- [2] “Superhorizon fluctuations and acoustic oscillations in relativistic heavy-ion collisions”, A.P. Mishra, R.K. Mohapatra, P.S. Saumia and A.M. Srivastava; **Indian J. Phys.** **85**, 909-915 (2011).
- [3] “Simulation of first order confinement transition in relativistic heavy-ion collision”, U.S. Gupta, R.K. Mohapatra, A.M. Srivastava and V.K. Tiwari; **Indian J. Phys.** **85**, 115-121 (2011).

(*) indicates papers on which this thesis is based.

Chapter 1

Introduction

1.1 Our Universe

It has been a great curiosity for mankind to understand the origin of our solar system, stars, galaxies and in one word, if we want to say, about our universe. But the birth of modern cosmology started during 1970s. There has been spectacular progress in the development of cosmology both at theoretical and observational fronts. The development of the new era in theoretical cosmology can be associated with the development of the gauge theories of weak, electromagnetic and strong interactions which says that the properties of matter in the early universe were quite different from what we see now. The current understanding of the universe is based on the hot big bang model of modern cosmology. This model is usually known as the standard model of cosmology. However, one has to go beyond standard model of cosmology to understand the universe better. The standard model of cosmology is based on three observational pillars, namely the Hubble law exhibiting expansion of the universe [1], the black body radiation left over from a stage 300,000 years after the beginning of universe, called as the cosmic microwave back ground radiation (CMBR) [2] and light element abundances which are in accordance with big bang nucleosynthesis (BBN) calculations [3]. The beyond standard model cosmology includes mainly the study of inflation, dark matter and dark energy, various models of baryogenesis etc.

According to the big bang model, the universe started from a singularity where the energy density and temperature of the universe were infinitely large. Around

Planck era, when the age of the universe is of the order of 10^{-43} sec, the energy density of the universe is of the order of 10^{93} gm cm^{-3} . One can compare the orders of magnitude difference with respect to nuclear density of about 10^{14} gm cm^{-3} . At this high energy density corresponding to the Planck stage, it is expected that all four fundamental forces of nature may be unified. According to the big bang model, the universe has been expanding from the beginning upto now, with the present age of the Universe being about 13.6 billion years. Due to the expansion of the universe, it becomes cooler. It is believed that during its early expansion history, the Universe went through several phase transitions like Grand Unified Theory (GUT), electroweak, and QCD phase transitions. The time line of the early universe which shows important stages of the early universe is presented in Fig.(1.1). It is believed that a grand unified theory stage existed above the energy scale of 10^{16} GeV where strong and electroweak forces are unified into one interaction and only gravity remaining a separate force. However, the energy scale of GUT phase transition remains out of the reach of present and upcoming collider experiments and hence directly inaccessible in the laboratories (with the exception of the proton decay experiment). So, it is very difficult to test these models against observations. However, one of the important aspects of these phase transitions is that they may leave imprints on the universe, which could subsequently have affected the evolution of the universe. During GUT phase transition, a certain gauge group representing the unified theory (e.g. $SU(5)$ or $SO(10)$) is spontaneously broken into standard model gauge group $SU(3)_c \times SU(2)_L \times U(1)_Y$. Such a spontaneous symmetry breaking phase transition might have lead to the formation of topological defects e.g monopoles, and cosmic strings. (Domain walls also could be produced, however, for such high energy scales, these are inconsistent with observations.) The study of these topological defects in the context of early universe is of great interest as it can provide an observational window into the very high energy scale physics of the early stages of the universe.

The topological defects are solitonic solutions of the field equation which arise when a symmetry of the theory is broken spontaneously giving rise to nontrivial topology of the vacuum manifold. These objects are produced inevitably during corresponding phase transitions in the early universe [4]. The different types of topological defects produced in the symmetry breaking transitions depends on the topology of

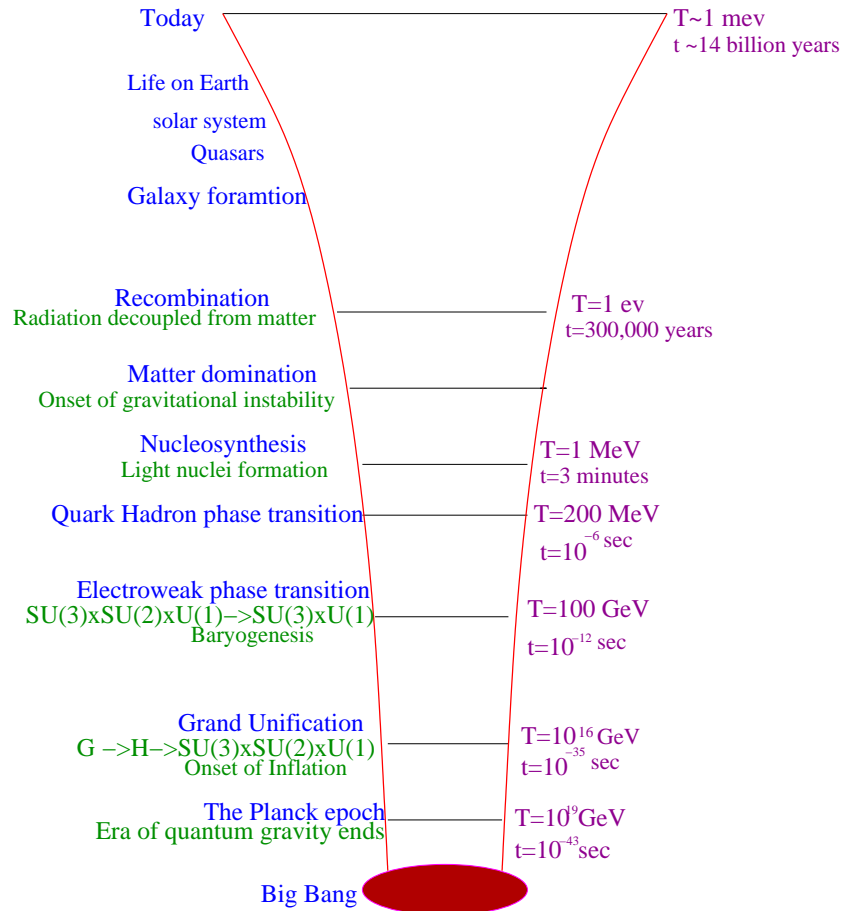


Figure 1.1: Time line of the Universe

the vacuum manifold. If the vacuum manifold is a circle after spontaneous symmetry breakdown, then cosmic strings are produced. If the vacuum manifold is a 2-sphere S^2 , then point like defects i.e monopoles are produced and if the vacuum manifold has disconnected components, then sheet like defects i.e domain walls are produced. The detailed study of these objects in different models and its comparison to the observations, puts constraints on the parameters of the theory and restricts different models.

The abundance of monopoles produced during GUT transition is so large that the energy density would be at least 10^{13} times the critical energy density of the universe now. So, the presence of these monopoles would be a cosmological disaster. Solving this *monopole problem* was one of the main motivations which led Guth to propose

the idea of inflation [5]. During inflation which took place after GUT transition, the universe expanded exponentially (by a factor of e^{60} or more) during a very short period of time. During this inflationary phase, the universe underwent an accelerated expansion because of repulsive nature of the vacuum energy (with negative pressure) of a scalar field. The inflationary expansion of the Universe dilutes the density of monopoles drastically. So, the monopole problem is neatly solved by the idea of inflation. The theory of inflation also solves the so called horizon and flatness problem of cosmology [5].

The cosmic strings are the most fascinating and most thoroughly studied defects in the context of the early universe [4]. Initially it was believed that cosmic strings play the dominant role in the structure formation. By now it is clear from the analysis of CMBR anisotropies from WMAP, that the contribution of cosmic strings and other topological defects for structure formation is insignificant. The seeds for structure formation originated during the inflationary period. The quantum fluctuations in the inflaton field of the order 10^{-5} is the main reason for the formation of structures i.e galaxies, clusters that we see around us today. The theory of inflation which predicts the beautiful acoustic peaks in CMBR spectrum is in very good agreement with WMAP data. These acoustic peaks are produced due to the coherent nature of the perturbations, i.e the perturbations which go out of the horizon during inflation are essentially frozen until they re-enter the horizon [6]. But the perturbations produced due to these topological defects are not coherent in nature. So, they don't produce these beautiful acoustic peaks in the CMBR spectrum. However, the presence of cosmic strings can affect the evolution of the universe in many other ways, and as we mentioned above, their observation itself will provide a direct window to GUT scale physics.

The models which produce domain walls in very early universe are discarded because at least one domain wall per horizon is produced during cosmological phase transition. The resulting mass of the domain wall exceeds the mass of matter within the present horizon by many orders of magnitude. Therefore, domain walls are cosmologically admissible only if the corresponding symmetry breaking scale is extremely low.

Since it is the topology of the vacuum manifold which determines the possibility

of formation of different types of defects, formation of these objects shows features which are universal, irrespective of the symmetry breaking scale and details of the phase transitions. The best known examples of defects formation in condensed matter systems are flux tubes in Type II superconductor [7], vortex line in liquid Helium, and line and point defects in liquid crystals [8]. Kibble proposed a mechanism for the production of topological defects in the context of early universe [9]. However, this mechanism is now applied to study defect production in all systems with spontaneous symmetry breaking phase transition [10].

When the universe is 10^{-12} sec old, it undergoes Electroweak phase transition where the standard model gauge group $SU(3)_c \times SU(2)_L \times U(1)_Y$ spontaneously breaks to $SU(3)_c \times U(1)_{em}$. Due to the spontaneous breaking of symmetry, W and Z gauge bosons get their masses by Higg's mechanism [11] and Yukawa couplings to the Higgs field gives masses to the fermions. It is also believed that during the electroweak phase transition, the baryon-antibaryon asymmetry may have been generated leading to the present Universe being matter (baryon) dominated.

The phase transition which is of most importance to our discussion is the QCD phase transition and the universe undergoes this transition when its temperature is of the order of 200 MeV. The age of the universe is few micro seconds at this stage. This happens to be the only phase transition in Universe which can be studied in the laboratory. This phase transition occurs as the universe cools from a deconfined state of quarks and gluons, called as the quark-gluon plasma (QGP) phase at high temperature, to a low temperature confined phase where quarks are confined into color neutral hadrons. The possibility of investigating this phase transition is being explored in relativistic heavy-ion collision experiments (RHICE) for some time now, and the evidence from various experiments (SPS, AGS, RHIC, LHC) has been mounting that a QGP phase has been created in the laboratory. This possibility is tantalizing as it provides glimpses into a stage of the universe where similar energy density and temperature once existed.

It turns out that the QGP phase of QCD allows for the existence of different types of topological defects. Since structure of QCD is much better understood than, e.g. grand unified theories, the possibility of topological defects in the QGP phase is of great importance. If these defects can be detected in RHICE, it will provide the

first (and may be the only possible) laboratory study of such topological objects in a relativistic quantum field theory system. Thus, it is of great interest to study their existence and their properties in the QGP phase. In this thesis, we will study the details of formation and evolution of these topological defects in QCD phase transition in the context of Relativistic heavy-ion collision experiments (RHICE).

1.2 QCD Phase Transition

The fundamental theory of strong interactions between quarks and gluons is known as quantum chromo dynamics (QCD). QCD is a non abelian gauge theory described by SU(3) color gauge group. The gauge fields in QCD are self interacting in contrast to quantum electro-dynamics (QED). There are two important aspects of QCD, namely the asymptotic freedom and confinement. The celebrated aspect of QCD, the asymptotic freedom, refers to the coupling between quarks and gluons becoming very weak at very high temperature or at very high density [12]. This is in contrast to QED in which the coupling between the charged particles increases with increasing energy. Due to asymptotic freedom of QCD, at very high temperatures and/or density, quarks and gluons are expected to form a plasma of weakly interacting particles, where quarks will be no longer confined into hadrons. At low temperature, the coupling between quarks and gluons is very strong and they are confined in color neutral hadronic states, this is known as color confinement. This strongly interacting matter is described at the fundamental level through the interactions of quarks by the exchange of gluons. The low temperature phase of QCD is poorly understood due to the nonperturbative nature of physics in this regime.

Apart from the SU(3) color gauge symmetry, there is another important symmetry of QCD called chiral symmetry [13] which is a global symmetry. This symmetry arises due to smallness of masses of up (u) and down (d) quarks (and to some level strange (s) quark) compared to the QCD scale. Due to the chiral symmetry left handed and right handed quarks are decoupled from each other. However, in nature we don't see any chiral partners of hadrons (e.g. for pions). The explanation for this is provided by assuming that the chiral symmetry is spontaneously broken in the low temperature hadronic phase where the quarks acquire constituent masses. This chiral symmetry is

restored at high temperature. As the masses of u,d,s quarks are not strictly zero, the chiral symmetry is an approximate symmetry and is explicitly broken by the quark mass terms. Lattice QCD results indicate that the deconfinement and chiral phase transition occurs at approximately the same temperature [14–17].

There are several relativistic heavy-ion collision experiments which have been already carried out at CERN (SPS) and BNL (AGS) in 1980s. These were both fixed-target experiments that, among other things, collided Au+Au at upto 11 GeV per nucleon beam energy (AGS) and Pb+Pb at up to 160 A GeV (SPS).

These experiments revealed tantalizing evidence of a hot and dense state of matter that had not been seen previously. In this energy regime, baryons stemming from projectile and target are partially or fully stopped by each other, forming a fairly baryon rich matter in the middle of the reaction zone. Thus, these reactions provide a tool to study very highly excited baryon rich matter or baryon rich quark gluon plasma. This regime corresponds to the QGP phase at higher baryon chemical potential in the QCD phase diagram. But, it is essential to study the physics of QCD transition at larger energies compared to AGS and SPS to get a clear picture of hot and dense matter produced with temperature clearly above the transition temperature. Further, at higher energies the QGP systems produced has low baryon density (due to asymptotic freedom of QCD), and this system much closely resembles the QGP phase of the universe which undergoes QCD phase transition with almost zero baryon chemical potential. At present, there are two ongoing high energy experiments, one is at RHIC (BNL) with centre of mass energy per nucleon pair $\sqrt{S_{NN}}= 200$ GeV and the other is at LHC (CERN) with centre of mass energy $\sqrt{S_{NN}}= 2.76$ TeV with plans to reach a value of 5.5 TeV. These are collider experiments where two heavy ion beams collide at a very high centre of mass energy. At such high energy collisions at RHIC and LHC the initial baryons from target and projectile are almost transparent to each other. They don't stop each other and almost pass through each other while depositing energy at the centre to form secondary partons. These partons redistribute energy within themselves due to enough rescatterings in between them and produce a locally thermally equilibrated system which is expected to be in the QGP phase. Thus, the QGP state formed in RHIC and LHC at mid rapidity is almost baryon free with small baryon chemical potential. One of the main aims of these experiments is

to study QCD phase transition i.e existence of QGP phase at high energy density or temperature. For a review on the theoretical aspects of QGP formation in these high energy experiments, see [18].

The QCD phase diagram as a function of temperature and baryon chemical potential is shown in Fig.(1.2). The baryon chemical potential is the amount of energy that is added to a system held at constant volume and entropy with the addition of one baryon and can be thought of as a measure of net baryon density. At low temperature, the normal nuclear matter, such as, a *Pb* nucleus, sits at $T = 0$ and $\mu_B = 940$ MeV. In Fig.(1.2), the short line emerging from this blob indicates the nuclear liquid-gas phase transition, with a critical end point at a temperature of about 7.5 MeV. When we go to higher temperatures more and more hadron resonances are excited and we have a hadron resonance gas.

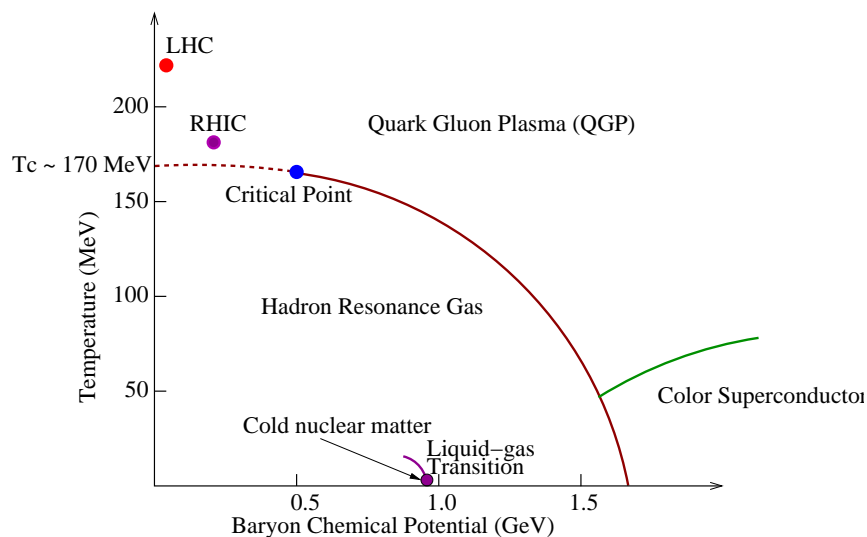


Figure 1.2: QCD phase diagram

Lattice QCD predicts the critical temperature for the transition from the confined hadronic phase to the deconfined QGP phase to be about 170 MeV. It also predicts that it is a first order phase transition for pure SU(3) gauge theory. But for real QCD, involving dynamical quarks, it becomes a crossover [19]. These Lattice QCD calculations are at zero baryon chemical potential. For finite chemical potential, Lattice QCD faces 'fermion sign problem'. However, now there are certain methods

in which calculations are possible for finite chemical potential in Lattice QCD. The physics of RHIC and LHC in central rapidity region mainly corresponds to near zero baryon chemical potential, and the thermodynamic properties of the system studied through lattice QCD provide good approximations. But, in the experiments carried out at SPS and AGS (and at RHIC in the beam energy scan at lower energies), the system produced corresponds to higher baryon chemical potential QGP phase. The properties of such a system need to be studied by different phenomenological models. These phenomenological models (chiral models) predict that QCD phase transition is a first order phase transition at higher baryon chemical potential. This first order line (going towards lower μ_B) ends in a critical point where the transition is a continuous transition, afterwards this is a crossover. This is an active area of research to find QCD critical point as well as determining the critical fluctuations and universality properties at this critical end point.

At low temperatures and asymptotically large baryon densities quarks are still deconfined, although not in a quark-gluon plasma state but in a color superconductor state [20]. When more and more cold nuclear matter is compressed to a small volume, a first order transition in the quark matter is expected to occur at high μ_B . This transition leads to a color superconductor phase due to Cooper pairing of quarks and this is analogous to pairing of electrons into 'quasi-bosons' that is responsible for superconductivity in solid state physics. The superconducting state is separated from the QGP by a first order transition at a critical temperature estimated to be of order 30-50 MeV. This area has astrophysical relevance with neutron stars having dense quark matter core.

In order to understand the formation of QGP state in relativistic heavy-ion collider experiments (RHICE) in detail, we need to understand the space time evolution of this state in RHICE.

1.3 Space-time Evolution of QGP in RHICE

In ultra-relativistic heavy-ion collisions, the two heavy nuclei traveling along z axis opposite to each other collide at very high center of mass energy. The two nuclei

essentially pass through each other due to asymptotic freedom. However, the interaction of partons in the colliding nucleons still deposits a large amount of energy in terms of secondary partons (quarks and gluons) in the central region of the collision. The space time evolution of this system mainly can be divided into three main stages: pre-equilibrium, equilibrium and freezeout stage.

Before we discuss the space time evolution of this system, we will discuss briefly the initial conditions used in RHICE. There are two initial conditions used: color glass condensate (CGC) model and Glauber model.

At very high collision energies particle production at midrapidity (particles with small longitudinal momenta in the center of momentum frame) probes the nucleon structure functions at small x where x is the fraction of the beam momentum carried by the partons whose collision produces the secondary partons. At small x gluon distribution functions becomes very large and gluons fill the transverse area of colliding nuclei densely [21, 22], leading to gluon saturation. The initial gluons can be effectively described by a classical gluon field in which the coupling is weak but nonlinear density effects are important [23, 24]. This model is known as 'color glass condensate'. This model is used to create initial condition for hydrodynamical evolution. In this model, the gluon distribution for each nucleon is computed and the nuclear collision is modeled as interactions between these coherent color fields.

Glauber model is also widely used to generate initial condition for hydrodynamical evolution. This model generates an initial condition by sampling a Woods-Saxon nuclear density distribution for each nucleus. The experimentally measured nucleon-nucleon cross section is used to select which pairs of nucleon interact, and the scale of their interaction [25].

In the very early stages of collision (pre-equilibrium stage), before the bulk of the quanta are produced, from the fraction of the beam energy lost in the collision, "hard" particles are produced with either a large mass or large transverse momenta $P_T \gg 1$ GeV. Their creation involves large momentum transfers, therefore their production can be calculated in perturbative QCD, using factorization theorems, from the nuclear structure functions. High P_T jets from the fragmentation of hard partons have reasonably large cross sections only at RHIC and LHC energies. Once these hard particles are produced, we can use them to probe the soft matter created

by the bulk of soft particles.

In this pre-equilibrium stage direct photons are also produced [26], either real or virtual. In case of virtual photons, they produce lepton-antilepton pairs, generally known as dileptons. Such photons are produced by the electric charges in the medium (i.e. by quarks and antiquarks during the early collision stage). Their production cross section is proportional to the square of the fine structure constant $\alpha = 1/137$ and so it is very small. However, they also reinteract only with this small electromagnetic cross section. Thus, their mean free path even in a very dense quark-gluon plasma is of the order of 50000 fm, much larger than heavy-ion fireball size. In contrast to all hadronic probes, they thus escape from the collision zone without re-interaction and carry pristine information about the momentum distributions of their parent quarks and antiquarks into the detector. However there is a huge background because of the decay of pions to photons, and other resonance decays from the hadronic phase.

After initial parton production, one must describe the rescattering and thermalization of the produced quanta. In the pre-equilibrium stage, this is done with kinetic transport theory (Relativistic Boltzmann equation), also known as parton cascade [27–29]. There is secondary parton production due to rescattering between the initial partons and the system quickly achieves local thermalisation. The thermalisation time for RHIC is less than 1 fm and even smaller for LHC. The critical energy density for QGP formation is expected to be of the order of $1 \text{ GeV}/fm^3$. The initial energy density achieved at RHIC for Au-Au collision at $S_{NN} = 200 \text{ GeV}$ is of the order of $20 \text{ GeV}/fm^3$. This energy density is 100 times larger than the normal nuclear matter density. Initially, it was believed that at such large energy density, an ideal gas of quarks and gluons will be formed where the interaction between the partons is very small. But, the early thermalisation as well as a very small value of $\frac{\eta}{s}$ ratio (extracted from the comparison of elliptic flow measurements and hydrodynamics simulations) at RHIC hints towards a (strongly coupled) perfect fluid behavior of QGP rather than ideal gas behavior. Soon after the system reaches local thermal equilibrium, hydrodynamics is applicable to the system [30]. There is longitudinal expansion as well as transverse expansion of QGP which we will describe below in detail. Due to the expansion of QGP, the temperature and energy density of the system decreases. When the temperature of the system is lower than the critical

temperature $T_c = 170\text{MeV}$, hadronisation takes place.

The time scale of the QGP phase is of the order of 10 fm. After this, hadron formation takes place. These hadrons keep interacting as long as the interaction rate remains larger than the expansion rate. At this point, the chemical freeze out happens after which different particle abundances remain fixed. There is only elastic scattering between the hadrons after the chemical freezeout, apart from decays. When the density of hadrons is very small, kinetic freezeout happens and hadrons are decoupled. Finally, we detect these hadrons in detectors. From the study of the properties of these final hadrons one has to deduce the existence of the transient stage of QGP as well as study its different properties. The space time evolution of QGP in RHICE is presented in Fig.(1.3).

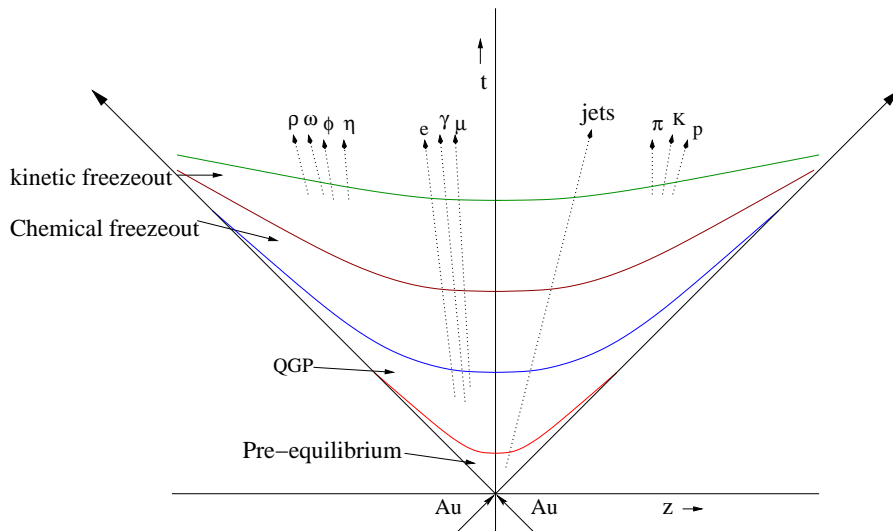


Figure 1.3: Schematic view of space time evolution of QGP in RHICE

1.3.1 Bjorken's Longitudinal Boost Invariance

Utilizing experimental observations for particle multiplicities in high energy collisions, that dN/dy distribution has a constant plateau in the mid rapidity region, Bjorken assumed that at sufficiently high energy the particle production is independent of longitudinal reference frame [31], at least near the central rapidity region. As mentioned in ref. [31], “The essence of this assumption is that the space time evolution of the

system looks essentially the same in all centre of mass like frames i.e in all frames where the emergent excited nuclei are, shortly after the collision, highly Lorentz contracted pancakes receding in opposite direction from the collision point at the speed of light”.

Bjorken used this symmetry property as an initial condition. Energy density $\epsilon(x)$, pressure $p(x)$, temperature $T(x)$ depend locally only on proper time τ and independent of the space time rapidity variable $y = \frac{1}{2} \ln(\frac{t+z}{t-z})$ initially and this condition is satisfied at later times due to longitudinal boost invariance. The longitudinal flow velocity has the scaling form $v_z = z/t$. Under this assumption, space time rapidity is same as momentum space rapidity.

Hydrodynamics equations can be solved analytically for 1+1 dimension under the assumption of Bjorken’s longitudinal boost invariance. This is a good approximation (1+1 dimension) for times small compared to the radius of nucleus. At later times, transverse expansion becomes important and 1+1 dimensional picture is no longer a valid approximation.

From the energy momentum conservation equation in 1+1 dimension

$$\partial_\mu T^{\mu\nu} = 0 \tag{1.1}$$

and using the perfect fluid form of $T^{\mu\nu}$

$$T^{\mu\nu} = (\epsilon + p)u^\mu u^\nu - pg^{\mu\nu} \tag{1.2}$$

where $u^\mu = (t, 0, 0, z)/\tau_0$

one can derive the following equation, using Bjorken’s longitudinal boost invariance and $u^\mu u_\mu = 1$

$$\frac{d\epsilon}{d\tau} = -\frac{(\epsilon + p)}{\tau} \tag{1.3}$$

For an ideal relativistic fluid, $p = \epsilon/3$. With this equation of state, Eq.(1.3) shows that ϵ varies as $\tau^{-4/3}$ and T varies as $\tau^{-1/3}$.

The rapidity distributions are more difficult to analyze theoretically than transverse momentum distributions since they are strongly affected by the pre collision

state memories. However all transverse momenta are generated by the collision itself, initially there is only momentum along longitudinal direction before collision. A huge fraction of the momenta of produced hadrons is due to the initial longitudinal motion of the colliding nuclei. In hydrodynamics simulations it has been found that final rapidity distributions are very sensitive to the initialization along the beam direction. Hence, collective transverse effects are cleaner signatures of reaction dynamics than longitudinal momentum distributions, and the best way to isolate from remnants of the initially colliding nuclei is by considering the central rapidity region.

1.3.2 Transverse Expansion

The system thermalises locally within 1 fm time due to enough rescatterings between the produced partons in ultra relativistic heavy-ion collisions. The driving force for the hydrodynamic expansion are the transverse pressure gradients which accelerate the fireball matter radially outward, building up the collective transverse flow [32]. In a central collision, the radial expansion of fluid is most important and significant. However, in non-central collisions, there is initial spatial anisotropy due to the collision geometry of the two nuclei. However, initially, the momentum space distribution is isotropic in the transverse plane. Due to enough rescatterings between the produced partons, the system achieves local thermal equilibrium rapidly and hydrodynamical evolution starts. The pressure gradient along the impact parameter vector (the x axis) is larger compared to the axis perpendicular to the impact parameter vector in the transverse plane (the y axis) as shown in the Fig.(1.4). According to Euler's equation of fluid motion, the fluid will accelerate more along the x axis, leading to larger flow momentum along x-axis compared to the y axis. This momentum anisotropy increases in time, while the spatial anisotropy decreases. This fluid flow adds to the momentum of hadrons resulting from the hadronisation. Thus, the flow anisotropy results in a momentum anisotropy of hadrons.

This momentum anisotropy is imprinted in final hadrons which we detect in our detector. The strength of anisotropic flow is usually quantified with a fourier decomposition of the azimuthal distribution of observed particles relative to the reaction plane. The differential invariant distribution of particles in the final state in heavy-ion collision is a periodic and even function of ϕ i.e., reflection symmetric with respect

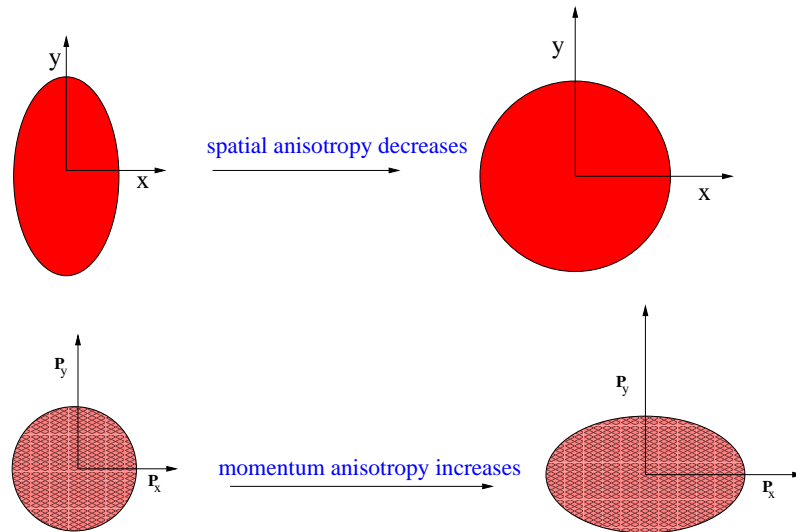


Figure 1.4: Top figure shows the decrease of spatial anisotropy and bottom figure shows the increase of momentum anisotropy as the system evolves.

to the reaction plane (This is the plane containing impact parameter vector and collision axis).

$$E \frac{d^3 N}{d^3 P} = \frac{d^3 N}{2\pi p_t dp_t dy d\phi} = \frac{d^2 N}{p_t dp_t dy} \frac{1}{2\pi} [1 + \sum 2v_n \cos(n\phi)] \quad (1.4)$$

The leading term in the square bracket in the above expression represents azimuthally symmetric radial flow. Here v_1 is the directed flow and second fourier component v_2 is the elliptic flow. In non-central collisions, due to the initial elliptical geometry of overlap region, the elliptic flow coefficient is significantly large compared to other flow coefficients. This coefficient v_2 is proportional to the eccentricity of the initial collision region defined by the overlap of the colliding of two nuclei.

In the above equation, the azimuthal angle ϕ is measured w.r.t the reaction plane. However, it is difficult to experimentally determine the orientation of the reaction plane event by event. Due to this, it is also very difficult to calculate higher order flow coefficients. There are some methods, like two particle correlation method, which avoid the determination of reaction plane while calculating flow anisotropies. There is one efficient method of calculating higher order flow coefficients without any determination of event plane. This analysis technique is motivated by the calculation of

CMBR anisotropies analysis technique [33]. In chapter 6 of this thesis, we will describe yet another technique to determine event plane and elliptic flow anisotropy [34].

However, there are nonflow azimuthal correlations from various sources arising from quantum correlation due to HBT effect, and back to back correlation between the momenta of particles due to the total transverse momenta of outgoing particles being zero. Other nonflow correlations are due to resonance decays such as $\Delta \rightarrow p\pi$ and $\rho \rightarrow \pi\pi$. Finally, Coulomb and strong interactions between the pairs of particles with low relative velocities (final state interactions) produce small angle azimuthal correlations. These nonflow correlations have to be subtracted from flow correlations suitably to get final flow coefficients.

However, the v_2 coefficient is also not strictly zero in central collision. This is due to the initial state fluctuations which gives nonzero v_2 for central collision. The initial state fluctuations primarily arise due to the fluctuation in the positions of nucleons inside the nuclei as well as due to localisation of partons inside the nucleons. The possible influence of initial geometry fluctuations resulting from these initial state fluctuations was used to explain the surprising large values of elliptic flow measured for central $Cu + Cu$ collision, where the average eccentricity calculated with respect to the reaction plane angle is small [35]. For a Glauber Monte Carlo event, the minor axis of eccentricity of the region defined by nucleon-nucleon interaction points does not necessarily point along the reaction plane vector but may be tilted. The third Fourier coefficient v_3 (triangular flow) is comparably large again due to the initial state fluctuations.

Now we will briefly discuss a few signatures of QGP which indicate that a transient stage of QGP may be produced in relativistic heavy-ion collisions.

1.4 Signatures of QGP, a brief discussion

The experimental observation and study of the quark-gluon plasma must be based on signals which can provide evidence of its formation and permit a characterization of its properties. Our evolving theoretical insight into the nature of this new state has also led to refinements in our understanding of these signals.

One of the most important signatures of QGP is the observation of elliptic flow

at RHIC in non central collisions proposed by Ollitrault in 1992 [32]. As we have discussed in the previous section about the transverse expansion, there is initial spatial anisotropy of QGP due to the initial collision geometry of nuclei in non central collision. But, it is almost isotropic in momentum space. Due to enough rescatterings between the produced partons, the system achieves a local thermal equilibrium in less than 1 fm time in RHIC. The system has different pressure gradients in different azimuthal directions in the transverse plane. There is larger pressure gradient along the event plane (which is the plane containing impact parameter vector and beam axis) compared to plane perpendicular to it. According to Euler's equation of fluid motion, there is larger flow velocity along the impact parameter direction due to larger pressure gradient.

This initial spatial anisotropy is converted into momentum anisotropy of the final particles due to hydrodynamical evolution of the system. So, we expect an elliptical distribution of final particles in the azimuthal plane. Elliptic flow is defined as the second fourier coefficient of the azimuthal distribution of the produced particles. The large value of elliptic flow at RHIC represents the system goes to a locally thermal equilibrated state called QGP at very early stages i.e time less than 1fm. It is only possible if the system has a lot of degrees of freedom (quarks, antiquarks and gluons) and there is enough rescatterings between them to produce this local equilibrium state at very early times. If it would have been a weakly interacting gas of partons, then it would have expanded isotropically (one should not have expected anisotropic distribution of final particles and large value of elliptic flow coefficient). Further, required shear viscosity of this QGP phase is found to be surprisingly small. This led to the early QGP phase being characterized as strongly coupled QGP phase, or sQGP. However, the most important observation of constituent quark number scaling of elliptic flow at RHIC at higher transverse momentum provides the best evidence for this deconfined phase of QGP [36]. It has been observed that if hadrons are formed via coalescence of the constituent quarks, then there is a region in the transverse momentum space ($2GeV \leq p_t \leq 6GeV$) where particle yield would be proportional to the quark density in the power equal to the number of constituent quarks, 2 for mesons and 3 for baryons. This implies elliptic flow of hadrons is just the sum of elliptic flow of its constituent quarks, leading to larger elliptic flow of baryons

compared to mesons at higher transverse momenta.

The elliptic flow depends on the properties of the system during very early stages ($\tau \leq 3 - 4$ fm). Equation of state (EOS) plays an important role in determining the flow anisotropy coefficients. EOS describes the dependence of the energy density and pressure of the system on temperature. EOS is used as an initial condition in hydrodynamical models. It is also important to know the details of phase transition i.e order of the phase transition whether first order, second order or crossover, as this can affect flow coefficients. For example, we will see later in the thesis that a quenched transition can lead to large fluctuations of flow coefficients.

Another important probe of QGP is the J/Ψ suppression in relativistic heavy-ion collisions [37]. These hadrons are bound state of c and \bar{c} quarks. These particle are produced in the early stages of high energy hadronic collisions. However, if a QGP phase is formed then the color charge of the c and \bar{c} will be Debye screened by the presence of other color charges in QGP. Hence, the strength of interaction between c and \bar{c} decreases and the bound state melts into free c and \bar{c} quarks. These combine with other quarks to form open charm hadrons. Thus, J/Ψ suppression was proposed as a signal for QGP formation in relativistic heavy-ion collisions. However, at higher collision energies like LHC energies, there is a lot of creation of J/Ψ particles. Though they are still Debye screened in QGP, due to their large numbers they can bind with another nearer suitable partner. So at LHC energies, J/Ψ suppression is also found in Pb-Pb collisions compared to corresponding p-p collisions [38]. However, the details of suppression pattern is consistent with a combination of suppression due to Debye screening and enhancement due to regeneration.

Jet quenching is another signature of QGP [39]. Jets are very high momentum particles produced due to hard scattering of partons at the initial stages of collision. When the jets are produced back to back at the edge of the overlap region, the jet near to the edge escapes easily containing all the energy. But the jet which travels in opposite direction has to cross the dense medium of QGP. While traversing through the QGP medium, jet loses its energy due to scattering with partons in QGP. This effect is known as jet quenching. The energy loss is proportional to the density of the medium times the scattering cross section between the probe and the medium constituents, integrated along the probes trajectory. Clear signatures of jet

quenching have been seen in nucleus-nucleus collision experiments pointing towards the formation of a dense compact medium of partons.

Strangeness enhancement is another signature of QGP [40]. The production of strange hadrons in high energy hadronic collisions is suppressed because the initial matter consists of up (u) and down (d) quarks and the large constituent mass of 450 MeV for strange quark makes it hard to create them from the vacuum as the produced partons hadronize. In a heavy-ion collision, if the reaction zone thermalises at energy density greater than ϵ_{cr} such that a deconfined phase is achieved and chiral symmetry is restored, strange quarks are much lighter (mass 150 MeV) and can be relatively easily created by secondary collisions of partons, leading to chemical equilibration between light and strange quarks. Hence, there is strangeness enhancement in relativistic heavy-ion collisions due to the QGP formation. Strong enhancement of strangeness is seen in heavy-ion collision experiments.

All these signatures of QGP give a strong belief that QGP is produced in relativistic heavy-ion collisions.

1.5 Outline of the Thesis

With this brief introduction to QGP state produced in Relativistic Heavy Ion collisions, we will now describe a brief outline of the topics to be discussed in next chapters.

In **chapter 2** of this thesis, we have discussed basic concepts of phase transition and different types of topological defects formation in symmetry breaking phase transitions.

Chapter 3 - 6 consist of our work on which this thesis is based. In **chapter 3**, we discuss the numerical simulation of confinement- deconfinement phase transition as a first order phase transition within Polyakov loop model and study the formation and evolution of $Z(3)$ wall and associated string network [41].

In **chapter 4**, we study the phase transition as a quench and study the evolution of $Z(3)$ domains as the order parameter field rolls down towards different $Z(3)$ vacua of the effective potential [42]. We find bubble like structures without any metastable confining vacuum. Here we also study the explicit symmetry breaking effects due to

quarks. When this effect is large the field will only roll down to the true vacuum. In this case we find that there are large oscillations of the field before it settles in the true vacuum. We have studied the effect of these oscillations on elliptic flow anisotropy.

In **chapter 5**, we present detailed investigations of the bubble like structures appearing during spinodal decomposition [43].

In **chapter 6**, we discuss a new technique to quantify elliptic flow anisotropy which is based on shape analysis of fluctuation patches [34].

Chapter 7 provides a summary of the results with conclusions and discussion.

Chapter 2

Phase Transition and Topological Defects

2.1 Introduction

Phase transitions are beautiful physical phenomena which occur in our day to day life. The changes of phase of the substances from solid to liquid (e.g ice to water) and liquid to gas (water to steam) are few examples of the phase transition which occur in our daily life. The study of phase transitions is an extensive area of research in a broad range of physical systems. An important class of phase transitions is that which corresponds to spontaneous symmetry breaking. One such example is the phase transition from paramagnetic phase to ferromagnetic phase which has been studied extensively in the laboratory. Other important examples of such spontaneous symmetry breaking phase transitions which are studied in the laboratory are λ transition of liquid He^4 from normal to superfluid phase and the superconducting phase transition of normal metal to super conductor at low temperatures. In the introduction, we discussed that the universe undergoes several phase transitions as it becomes cooler. In this chapter, we will describe various properties of the phase transitions and the formation of topological defects as a result of spontaneous symmetry breaking phase transitions.

The state of a system in thermodynamic equilibrium is represented by thermodynamic variables like pressure, temperature and chemical potentials etc. These

intrinsic parameters specify the phase of the system in equilibrium. According to statistical mechanics a system in equilibrium attains the lowest free energy state at the given values of the intrinsic parameters. A diagram drawn using appropriately chosen parameters for the system, showing its various thermodynamic phases, is called the phase diagram. The free energy of the system, in a particular phase, is analytic over the relevant regions of the phase diagram. Non-analyticity of partition function i.e of free energy over a certain region of parameter space indicates a phase boundary separating two different phases. So, phase transition is usually defined as a singularity in free energy or partition function of the system. The system in equilibrium tries to attain the minimum free energy state at the given values of intrinsic parameters. This tendency of system to attain the minimum free energy at different intrinsic parameters drives it to go from one phase to another phase across the phase boundary.

Phase transitions are usually classified into two types, first order and second order phase transitions. A first order phase transition is the one in which the first derivative of the free energy or partition function is discontinuous at the transition temperature. The second order or continuous phase transition is associated with continuous change of first order derivative of the free energy, but the second order derivative of free energy is discontinuous. The first order phase transition is associated with absorption or release of latent heat. The two phases can co-exist in a first order phase transition. The liquid to vapor transition is of first order in nature where the two phases co-exist. A first order phase transition can proceed through bubble nucleation. In liquid vapor phase transition, the bubbles of vapor phase start appearing when we increase the temperature of liquid through the transition temperature. As more and more heat is absorbed by the system, its temperature does not change until whole liquid is converted into vapor phase. In this chapter, we will describe first order phase transition through true vacuum bubble nucleation using Coleman's technique in the semi-classical theory [44] of quantum tunneling at zero temperature. We will also discuss briefly finite temperature extension of this theory which was developed by Linde [45].

Most of the phase transitions are associated with a change in symmetry of the system. However, it is not essential that the symmetry of the system should change

in the phase transition. For example liquid - vapor phase transition is not associated with any change in symmetry (isotropic in both phases). Phase transitions associated with change of symmetry are described through Spontaneous symmetry breaking (SSB). The phase transitions in the early universe (GUT, Electroweak and QCD) are associated with SSB. We will describe SSB in detail in the next section. In SSB the higher symmetry phase (less ordered) is associated with a unique true vacuum which respects a certain symmetry. That is, the symmetry is respected by the Lagrangian as well as by the vacuum in this less ordered phase. But due to phase transition from less ordered phase to more ordered phase, this symmetry is spontaneously broken. This means that in this ordered phase, the symmetry is respected by the Lagrangian of the system, but not by the ground state (vacuum) of the system. In this phase, the vacuum has degenerate structure and the system can choose any one of the degenerate vacua randomly after the phase transition.

One can define a thermodynamic variable called order parameter which characterizes different phases. The order parameter is usually taken to be zero in the symmetric phase and nonzero in the symmetry broken phase. The values of the order parameter field which minimize the free energy in a particular phase of the system constitute the order parameter space, or the vacuum manifold. The nature of variation of order parameter as a function of control parameters like temperature or pressure defines the order of the transition.

The first order phase transition is associated with a discontinuous change in the order parameter at the transition temperature. The transition occurs when localized fluctuations of order parameter field render a small region of the existing phase unstable against conversion to the other phase because of lower free energy in the later. These are the mainly bubbles of lower free energy state. They either expand or collapse depending on whether their size is larger or smaller as compared to the critical bubble size. The supercritical bubbles expand and coalesce and eventually convert the whole of the old phase to the new phase.

In the second order phase transition the order parameter changes continuously. The phase transition of paramagnetic to ferromagnetic is an example of second order or continuous phase transition. This phase transition is also associated with SSB. The

symmetric phase (paramagnetic) at high temperatures respects the rotational symmetry (magnetic spins are random) and the order parameter i.e net magnetic moment is zero. But below Curie temperature, the ferromagnetic phase appears where the spins are not random completely, but align in a particular direction within domains and the orientation of spin changes from one domain to another. The variation of the orientation of the magnetic moments in these domains spans the entire vacuum manifold in the low temperature phase. In this phase, the rotational symmetry is respected by the Hamiltonian (Lagrangian) of the system but not respected by the ground state of the system. So the symmetry is spontaneously broken in low temperature ferromagnetic phase. The order parameter i.e net magnetic moment is not zero in this phase.

Except these well defined phase transition mechanism where one stable (or metastable) phase is converted into another phase with slow change of control parameters, there is another mechanism called spinodal decomposition where one phase is converted into another phase. A quench provides an example of this where the control parameters are changed so rapidly that the order parameter field does not get time to respond to it and it remains in its original state. As this state is highly unstable for the new values of the parameters, exponential growth of long wavelength fluctuations convert the entire system to the new phase. This situation also arises in a first order phase transition when the order parameter field is trapped in the metastable vacuum while the barrier separating this vacuum from the true vacuum disappears. We will also study this type of dynamics of transition for the case of confinement-deconfinement transition in chapter 5.

Crossover corresponds to the situation when there is no genuine phase transition. There is no singularity in the partition function when one phase is converted into another phase. In the phase diagram, where the phase transition line ends with a critical point, the parameter space beyond this critical point belongs to crossover region. QCD phase transition at high values of μ_B is of first order. With decreasing μ_B , the first order transition line in the phase diagram ends at a critical point and the region for lower μ_B corresponds to a crossover region as shown in Fig.(1.2) in Chapter 1.

In most physical systems, the symmetry is restored at higher temperature and

broken at low temperature. However, this is not always true. We will discuss about $Z(3)$ global symmetry in this chapter which is restored in the low temperature confined phase of QCD and spontaneously broken at high temperatures in the deconfined phase.

2.1.1 Spontaneous Symmetry Breaking

One of the most important concepts in modern particle physics is that of spontaneous symmetry breaking (SSB). The idea that there are underlying symmetries of Nature that are not manifest in the structure of the vacuum appears to play a crucial role in the unification of the forces. In all unified gauge theories including the standard model of particle physics the underlying gauge symmetry is larger than that of our vacuum.

In the early universe, GUT unifies strong and electroweak interactions. In the electroweak theory, a local gauge theory unifying electromagnetic and weak interactions is based on the idea of SSB [47]. The phenomenon of SSB is most often implemented with a scalar field, called Higgs field in the context of particle physics. Due to the spontaneous symmetry breaking of electroweak symmetry, the fundamental gauge bosons i.e W^+ , W^- and Z^0 become massive. This is the famous Higgs mechanism [11]. One of the important challenges of LHC is to find the existence of Higgs boson (which appears to have been discovered). In unified gauge theories, the symmetry of the Lagrangian is broken spontaneously during a phase transition. The effective potential which is the expression of free energy for the fields in the Lagrangian taking into account all quantum corrections basically contains all the information about the phases of the system as well as the order of the phase transition.

In this section, we will describe basic physics of SSB. The essential features of SSB can be illustrated in the following example of a complex scalar field.

Let's consider the Lagrangian density [48]

$$L = \partial_\mu \Phi \partial^\mu \Phi^* - V(\Phi). \quad (2.1)$$

where

$$V(\Phi) = \frac{1}{4}\lambda(|\Phi|^2 - \eta^2)^2 \quad (2.2)$$

Here, Φ is a complex scalar field and λ and η are positive real constants. The Lagrangian is invariant under U(1) global transformation.

$$\Phi(x) \rightarrow e^{i\alpha}\Phi(x) \quad (2.3)$$

The surface plot of the potential is shown in Fig.(2.1).

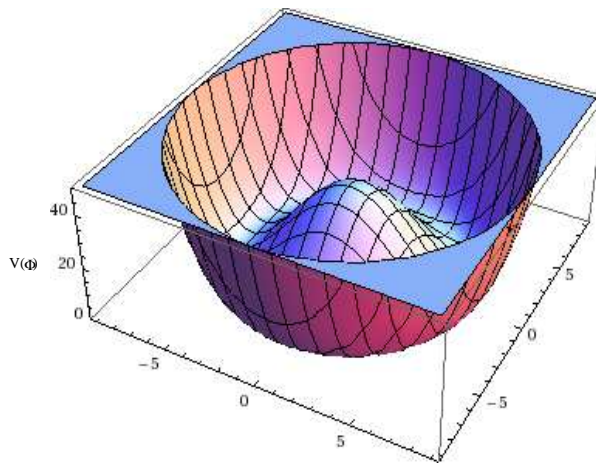


Figure 2.1: 3D potential.

The minimum of the potential $V(\Phi)$ lies on the circle $|\Phi| = \eta$. This circle represents the vacuum manifold of the theory. A particular choice of vacuum state is represented by giving the value of the vacuum expectation value (VEV) of the field operator Φ

$$\langle 0|\Phi|0\rangle = \eta e^{i\beta} \neq 0 \quad (2.4)$$

Here the vacuum is not invariant under the symmetry transformation given by Eq.(2.3). This represents the spontaneous breaking of global U(1) symmetry. Due to the SSB of a continuous global symmetry, massless Goldstone bosons appear in the theory. This can be seen as follows. In order to consider the particle spectrum in this model, we have to consider fluctuations of the field around a particular vacuum.

We choose the vacuum state with vanishing phase $\langle 0|\Phi|0\rangle = \eta$. Expanding the field around this vacuum state yields,

$$\Phi(x) = (\eta + \frac{1}{\sqrt{2}}\rho(x))e^{i\theta(x)} \quad (2.5)$$

Here, ρ and θ are real fields. The Lagrangian in Eq.(2.1) in term of these new fields becomes

$$L = \frac{1}{2}(\partial_\mu\rho)^2 + \eta^2(\partial_\mu\theta)^2 - \frac{1}{2}\lambda\eta^2\rho^2 + L_{int}(\rho, \theta) \quad (2.6)$$

The interaction part of the Lagrangian can be obtained from Eq.(2.1) and Eq.(2.2). The above form of the Lagrangian shows that the field ρ corresponds to a massive particle with mass, $m = \lambda\eta^2$, while the field θ , representing the angular excitation becomes massless. Despite of its simplicity, this model captures the essential physics of SSB. In general case, the number of Goldstone bosons will be equal to the dimension of the vacuum manifold (number of broken generators). In a phenomenological model, a well known example of Goldstone bosons are pions, which appear as a consequence of SSB of chiral symmetry in QCD in the massless limit of quarks.

In Sect. 2.3, we will discuss spontaneous breaking of $Z(3)$ global symmetry which is the centre group of $SU(3)$ gauge theory. As we have already discussed, SSB plays an important role in the study of phase transitions. It is also equally important in the study of topological defects which are the byproduct of SSB phase transitions. Before describing the topological defects, we will describe the dynamics of a first order phase transition through bubble nucleation using Coleman's technique of false vacuum decay in field theory [44].

2.1.2 First Order Phase Transition

Let's consider a first order phase transition with the following effective potential for a single real scalar field.

$$V(\phi) = \frac{\lambda}{4}\phi^2(\phi - \phi_0)^2 - \frac{\lambda}{2}\epsilon_0\phi_0\phi^3 \quad (2.7)$$

The potential is shown in Fig.(2.2). Here the metastable vacuum is at $\phi = 0$ and the unique true vacuum appears at

$$\phi = \sigma = \phi_0 \left[\frac{3(1 + \epsilon_0) + \sqrt{(9(1 + \epsilon_0)^2 - 8)}}{4} \right] \quad (2.8)$$

There is a barrier between metastable and true vacuum which is due to the ϕ^3 term in the effective potential. Note that, as $\epsilon_0 \rightarrow 0$, the global minimum σ approaches ϕ_0 and the minima at $\phi = 0$ and $\phi = \sigma$ becomes degenerate.

In the case of a first order phase transition, the field ϕ evolves from the metastable vacuum $\phi = 0$ (false vacuum) to $\phi = \sigma$ (true vacuum). Transition to the true vacuum state by quantum tunneling occurs through the nucleation of bubbles of the energetically favored phase $\phi = \sigma$, which then expand outward nearly at the speed of light. The semiclassical theory of quantum tunneling at zero temperature was given in [44] and the finite temperature extension of this theory was proposed by Linde [45]. We will discuss below semiclassical theory of false vacuum decay given by Coleman.

2.1.3 False Vacuum Decay

The rate of false vacuum decay is given by

$$\Gamma = Ae^{-S_E(\phi)} \quad (2.9)$$

Here ϕ is a solution of the Euclidean field equation which extremises the Euclidean action S_E given by

$$S_E(\phi) = \int d^3x dt_E \left[\frac{1}{2} \left(\frac{d\phi}{dt_E} \right)^2 + \frac{1}{2} (\vec{\nabla}\phi)^2 + V(\phi) \right] \quad (2.10)$$

The calculation of pre-exponential factor A requires considering fluctuations around the stationary points of action S_E

$$\frac{\delta S}{\delta x} = 0 \quad (2.11)$$

Integrating out the fluctuations one gets

$$A = \left(\frac{S_E(\phi)}{2\pi} \right)^2 \left(\frac{\det'[-\square_E + V''(\phi)]}{\det'[-\square_E + V''(0)]} \right)^{-1/2} \quad (2.12)$$

where prime indicates that zero eigenvalues of the operator are to be omitted when computing the determinant. See ref. [46] for detail.

At zero temperature, the least-action Euclidean solution has $O(4)$ symmetry, in which case ϕ is only a function of r , where $r^2 = |\vec{x}|^2 + t_E^2$ and the $O(4)$ Euclidean equation of motion for $\phi(r)$ is given by

$$\frac{d^2\phi}{dr^2} + \frac{3}{r} \frac{d\phi}{dr} - V'(\phi) = 0 \quad (2.13)$$

and Euclidean action reduces to

$$S_E = 2\pi^2 \int_0^\infty r^3 dr \left[\frac{1}{2} \left(\frac{d\phi}{dr} \right)^2 + V(\phi) \right] \quad (2.14)$$

The boundary conditions for the $O(4)$ solution are $\phi = 0$ at $r = \infty$ and $\frac{d\phi}{dr} = 0$ at $r = 0$. The value of ϕ at $r = 0$ is decided by the two boundary conditions. Starting with $\phi = \phi_e$ and $\frac{d\phi}{dr} = 0$ at $t_E = 0$, ϕ will evolve to $\phi = 0$ at $t_E = \infty$. Here, ϕ_e is somewhere in between $\phi = 0$ and $\phi = \sigma$ as discussed below.

The technique to find the escape point ϕ_e can be illustrated with the negative of the potential as shown in Fig.(2.2). If one interprets ϕ to be the ‘‘position’’ of a particle of unit mass and r to be the ‘‘time’’ variable, then Eq.(2.13) describes the classical motion of a particle under the influence of the inverted potential $-V(\phi)$ with a velocity dependent ‘‘friction’’ force. If ϕ starts at rest from the escape point ϕ_e , it will have just enough energy to overcome the friction force and come to rest at $\phi = 0$ at infinite r . If ϕ is released at rest from the left of the escape point ϕ_e , it will ‘‘undershoot’’ the desired final configuration. That is, after some finite r , ϕ will come to rest and then reverse direction at some point before $\phi = 0$. If ϕ is released at rest from the right of the escape point ϕ_e , it will ‘‘overshoot’’ the point $\phi = 0$ and go to negative ϕ . The escape point ϕ_e can thus be identified by trial, and this is our solution for $\phi(r)$ for the bubble profile. Then we can calculate Euclidean action for this solution.

2.1.4 Thin-Wall Approximation

In general, the analytic solution to Eq.(2.13) is not available. However, in the ‘thin-wall’ approximation, where the difference in energy between the metastable and true vacua is small compared to the height of the barrier, it is possible to find a simple, approximate analytic expression for S_E . In the thin wall limit ($\epsilon_0 \rightarrow 0$), the minima

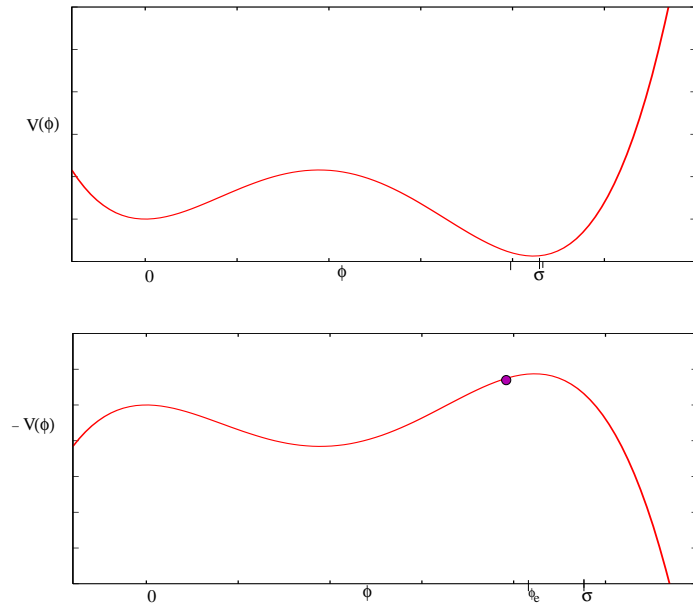


Figure 2.2: Top figure shows the potential for a first order phase transition, bottom figure is the inverted potential

are nearly degenerate. In order to overcome the friction term, ϕ_e must be very close to σ . The form of the solution can be understood by again using the particle analogy. For $\epsilon_0 \ll 1$, the particle sits near $\phi = \sigma$ for a very long time (i.e upto a large value of r) making the dissipation term ineffective. Then, at some large value of r , say $r \sim R$, the particle rapidly makes the transition across the 'dip' in $-V(\phi)$, and finally slowly comes to rest at $\phi = 0$. Here $\phi(r)$ corresponds to the bubble profile, and R to the bubble radius.

To estimate the thickness of the wall we can solve Eq.(2.13) for $r \geq R$. Here it takes longer time (larger r) before the field starts rolling. The friction term in Eq.(2.13) which is proportional to r^{-1} , can be neglected in this limit. The equation of motion is quite simple now

$$\frac{d^2 \phi}{dr^2} = V'(\phi) = V_0'(\phi) \quad (2.15)$$

where V_0 is the potential in the limit of exact degeneracy of the minima

The solution to the equation of motion ignoring damping term, with appropriate boundary condition [44], is

$$\frac{d\phi}{dr} = -2\sqrt{V_0(\phi)}; r = - \int^\phi \frac{d\phi'}{2\sqrt{V_0(\phi')}} \quad (2.16)$$

The thin-wall approximation solution can be summarised as :

$$\begin{aligned} \phi(r) &= \phi_0, r \ll R \\ &= \phi^{TW}(r), r \simeq R \\ &= 0, r \gg R \end{aligned} \quad (2.17)$$

Here $\phi^{TW}(r)$ is the profile of the wall (in the thin wall approximation) which interpolates between the true vacuum at $\phi = \phi_0$ and false vacuum $\phi = 0$.

For $r \ll R$, the first term in the expression for action i.e Eq.(2.14) vanishes and the second term $V(\phi_0) \equiv \epsilon = \frac{-\epsilon_0 \lambda \phi_0^4}{2}$. So,

$$S_{EI} = -\frac{1}{2}\pi^2 R^4 \epsilon$$

For $r \sim R$, the contribution to the action comes only from the wall profile

$$S_{EII} = 2\pi^2 R^3 S_1$$

$$\text{where } S_1 = \int_0^\infty dr \left[\frac{1}{2} \left(\frac{d\phi^{TW}}{dr} \right)^2 + V(\phi^{TW}) \right]$$

For $r \gg R$, both the terms vanishes, so $S_E = 0$

Therefore, Euclidean action can be written as

$$S_E(\phi) = S_{EI} + S_{EII} = -\pi^2 \frac{R^4}{2} \epsilon + 2\pi^2 R^3 S_1 \quad (2.18)$$

We can determine radius R by extremising Euclidean action $\frac{dS_E}{dR} = 0$. From this we find $R_c = \frac{3S_1}{\epsilon}$. In the thin wall limit, bubble radius is much larger than the wall thickness. The extremum action in this limit becomes $S_E = \frac{27\pi^2 S_1^4}{2\epsilon^3}$

The wall profile for the potential of Eq.(2.7) can be shown to be of the form

$$\phi^{TW}(r) = \frac{1}{2}\phi_0 \left[1 - \tanh \frac{r-R}{\Delta} \right] \quad (2.19)$$

Where Δ is the thickness of the wall which is equal to $\phi_0^{-1} \sqrt{8/\lambda}$ and the critical bubble radius is $R_c = (\sqrt{2\lambda\epsilon_0}\phi_0)^{-1}$.

The bubble action in this limit ($\epsilon_0 \ll 1$), is much larger than one as one would expect since the energy difference between the two minima is very small, hence tunneling rate should be suppressed.

2.1.5 Thick wall calculation

For the thick wall bubbles i.e when the difference between energy of two minima is not small compared to the barrier between them, one has to get the bubble profile numerically. One can solve the second order differential equation (Eq.(2.13)) by 4th order Runge Kutta method. There are two boundary conditions for this 2nd order differential equation, $\phi = 0$ at $r = \infty$ and $\frac{d\phi}{dr} = 0$ at $r = 0$. Here, we follow the same approach as Coleman as described above to get the escape point ϕ_e . In this way, it is analogous to a particle moving in an inverted potential. We first take some initial particle position and check whether it undershoots or overshoots. If the particle position is beyond the escape point, then it will overshoot. But if it is within escape point, it will undershoot. We keep on trying this by iteration until we get the escape point. Once we get the escape point, we get the whole profile as the solution of the differential equation.

2.1.6 Finite Temperature Effect on False Vacuum Decay

The phase transitions of interest to us are associated with the change of temperature. The tunneling rate at finite temperature is computed by following the same procedure above, remembering that field theory at finite temperature is equivalent to Euclidean field theory, periodic (anti periodic) for bosons (fermions) in imaginary time with period T^{-1} [45]. Thus, the finite temperature tunneling rate is found by Eq.(2.13) subject to the additional condition $\phi(t_E, x) = \phi(t_E + T^{-1}, x)$ and computing S_E .

In fact, the only modification is that instead of the $O(4)$ symmetric solution of Eq.(2.13) one should look for the $O(3)$ symmetric (with respect to spatial coordinates) solution, periodic in the “time” direction with period T^{-1} . At $T = 0$ the solution of Eq.(2.13) corresponding to the minimal value of the action is the $O(4)$ symmetric bubble with a certain typical radius $r(0)$. At finite temperature, one has to deal with $O(3)$ symmetric bubbles with radius $r(T)$ obeying periodicity in time direction. At $T \ll r^{-1}(T)$ the solution will be a series of similar bubbles placed at a distance T^{-1} from one another in the “time” direction. At $T \sim r^{-1}(T)$, the bubbles become overlapping. At $T \gg r^{-1}(T)$ (and this case is of most interest and importance for us) the solution is a cylinder, whose spatial cross section is the $O(3)$ symmetric bubble

of radius $r(T)$. In this case, the action S_E is reduced simply to

$$S_E = S_3/T \tag{2.20}$$

where $S_3 = \int d^3x \left[\frac{1}{2}(\nabla^2\phi)^2 + V_T(\phi) \right]$

At sufficiently high temperatures, the least action solution has $O(3)$ symmetry, and Eq.(2.13) becomes

$$\frac{d^2\phi}{dr^2} + \frac{2}{r} \frac{d\phi}{dr} - V'_T(\phi) = 0 \tag{2.21}$$

where $r^2 = |\vec{x}|^2$. The solution must satisfy the boundary conditions described earlier. After a simple change of integration variables, the Euclidean action for the $O(3)$ invariant solution is

$$S_3 = 4\pi \int r^2 dr \left[\frac{1}{2} \left(\frac{d\phi}{dr} \right)^2 + V_T(\phi) \right] \tag{2.22}$$

As in the zero temperature case, the ‘‘bounce’’ solution is straightforward to obtain numerically. We will use this method to calculate bubble profile in the confinement deconfinement phase transition in chapter 3.

2.2 Topological Defects

Topological defects are at the heart of most SSB based phase transitions. Whenever there is a phase transition based on spontaneous symmetry breaking, topological defects are produced if they are allowed by the structure of the vacuum manifold as we discuss below. These objects should be produced in high energy particle physics phase transitions just as well as they are routinely seen in low energy condensed matter phase transitions. In this thesis, we will study the production of topological defects in a relativistic quark hadron phase transition. However, production of topological defects is a vast topic of research in condensed matter systems. Common examples of such defects in condensed matter systems are the vortices in liquid He^3 , flux tubes in type II superconductor, and line and point defects in liquid crystals.

In SSB, the vacuum structure is nontrivial in the less symmetric phase. The space spanned by nontrivial degenerate vacua is known as the vacuum manifold and we will

represent it as M . After the phase transition, the order parameter field chooses different vacua from this vacuum manifold in different regions of space. These regions form domains in space. During further evolution of the system, the order parameter may get 'locked' in symmetric state in localized regions whenever neighboring domains cover the vacuum manifold in topologically nontrivial manner. These will be topological defects. Since these defects are produced due to non trivial topology of the vacuum manifold, these are called topological defects. The necessary conditions of the formation of such defects depends on various homotopy groups of the vacuum manifold. A theory may have symmetry breaking pattern with vacuum manifold consisting of two or more disconnected pieces. Such SSB results into the zeroth homotopy group of the vacuum manifold being nontrivial. In such a model, domain walls can form. Domain walls are two-dimensional thin surfaces appearing at the junction of field values belonging to different disconnected sectors of M . Similarly, other topological defects like strings, monopoles may arise when the first and second homotopy group of M are non-trivial, respectively.

Kibble in 1976 proposed the mechanism for the production of topological defects in phase transitions in the context of early universe [9]. Since the thermally produced defects are suppressed by Boltzmann factor in the early universe, Kibble mechanism plays an important role in the production of the defects in this case. However, this mechanism is also applicable for defect formation in condensed matter systems and plays a dominant role in most phase transitions.

2.2.1 Kibble Mechanism

We now briefly describe the physical picture of the formation of topological defects via the Kibble mechanism [9]. After a spontaneous symmetry breaking phase transition, the physical space consists of regions, called domains. In each domain the configuration of the order parameter field can be taken as nearly uniform while it varies randomly from one domain to another. In a numerical simulation where the phase transition is modeled to implement the Kibble mechanism, typically the physical region is divided in terms of elementary domains of definite geometrical shape. The order parameter is taken to be uniform within the domain and random variations of order parameter field within the vacuum manifold are allowed from one domain to

the other. The order parameter field configuration in between domains is assumed to be such that the variation of the order parameter field is minimum on the vacuum manifold (the so-called geodesic rule). With this simple construction, topological defects arise at the junctions of several domains if the variation of the order parameter in those domains traces a topologically non-trivial configuration in the vacuum manifold.

2.2.2 Domain Wall

The formation of different types of topological defects like domain walls, strings, monopole and textures depends on the topology of the vacuum. Domain walls are formed when the vacuum has disconnected components. When a discrete symmetry is spontaneously broken, this gives rise to the formation of domain walls. Domain walls occur at the boundaries between regions of space with values of the field ϕ in different components, with ϕ interpolating between these two values across the wall.

Let's consider a very simple model with a single real scalar field having double well potential. The Lagrangian is given by

$$L = \frac{1}{2}(\partial_\mu\phi)^2 - \frac{\lambda}{4}(\phi^2 - \eta^2)^2 \quad (2.23)$$

This Lagrangian has a discrete $Z(2)$ symmetry under $\phi \rightarrow -\phi$. The potential is shown in Fig.(2.3) (left panel). This potential has two minima at $\phi = \pm\eta$. The Z_2 symmetry is spontaneously broken when the field chooses one of the vacua. The field equation has the analytic solution for the profile of the domain wall.

$$\phi(x) = \eta \tanh \left[\left(\frac{\lambda}{2}\right)^{1/2} \eta x \right] \quad (2.24)$$

This solution is shown in Fig.(2.3) (right panel). This corresponds to a localized 'kink' centered about $x = 0$, which takes ϕ from $-\eta$ at $x \rightarrow -\infty$ to η at $x \rightarrow +\infty$. On the left side, far from the kink, the field lies in one of the ground states of the potential while, on the right side, it lies in the other ground state. The field $\phi(x)$, therefore, maps points at spatial infinity in physical space non-trivially into the vacuum manifold, $\phi = \pm\eta$. The energy of the field configuration is due to the localized departure of field from the disconnected minima as it continuously interpolates between these

two minima, rising over the potential hill of the double-well. The removal of this defect requires infinite cost of lifting all of the field on one side over this separating potential barrier. This renders the domain wall classically stable. The defect can be annihilated by an antidefect which has the opposite topological orientation i.e charge. This ϕ^4 kink arises in this simple model in one space and one time dimension. This becomes a planar wall in 3+1 dimension.

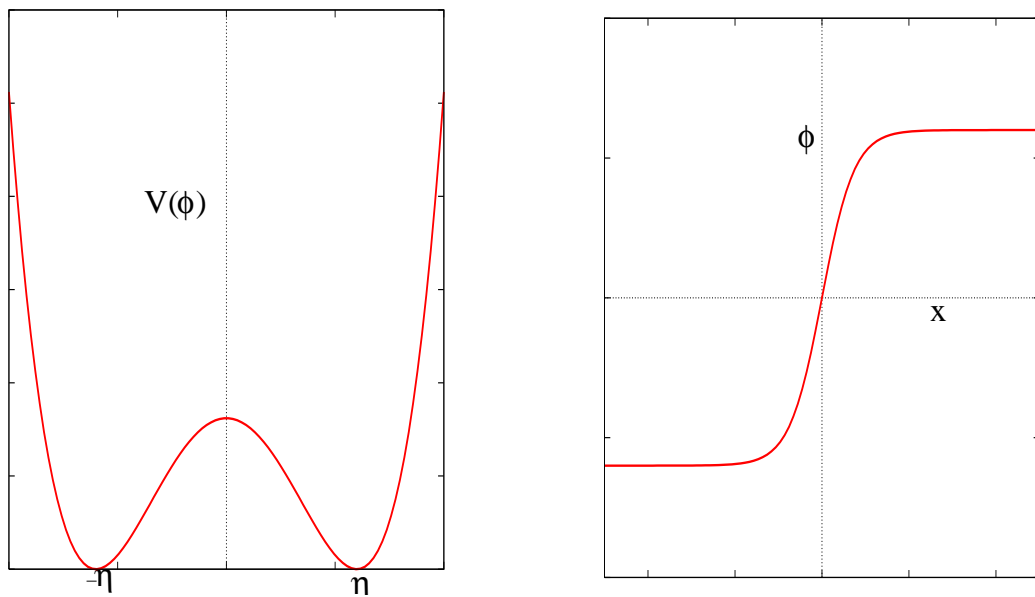


Figure 2.3: The double-well potential (a) gives rise to the ϕ^4 -kink solution which is illustrated in (b).

The finite, but non-zero, thickness of the wall is easy to understand. The terms contributing to the surface energy density include a gradient term, proportional to $\delta \times (\nabla \phi)^2 \sim \frac{\eta^2}{\delta}$, where δ is the wall thickness and a potential energy term, proportional to $\delta \times V(\phi) \sim \delta \lambda \eta^4$. The gradient term is minimized by making the wall as thick as possible, while the potential term is minimized by making the wall as thin as possible. The balance between these terms results in a wall of thickness

$$\delta \sim (\sqrt{\lambda} \eta)^{-1} \quad (2.25)$$

The vacuum energy at the center of the wall is $\rho \sim \lambda \eta^4$, and the surface energy density will be

$$\sigma \sim (\sqrt{\lambda}\eta^3) \quad (2.26)$$

The stability of the kink solution is a consequence of a topological conservation law. In this case, the topological conserved current is

$$j_\mu = \epsilon^{\mu\nu} \partial_\nu \phi \quad (2.27)$$

This contrasts with a current arising from a continuous symmetry of the Lagrangian which is conserved by Noether's theorem. The associated conserved charge of a configuration from Eq.(2.27) is then simply

$$N = \int j^0 dx = \phi|_{x=\infty} - \phi|_{x=-\infty} \quad (2.28)$$

The presence of a ϕ^4 -kink with ϕ in different vacua at $x = \pm\infty$, gives rise to a non-zero charge N and consequently indicates the topological stability of the configuration.

2.2.3 String

Strings appear in a model where a continuous symmetry is spontaneously broken leading to nontrivial first homotopy group of the vacuum manifold. Here, we will consider $U(1)$ global symmetry breaking as discussed in section 2.1.1. The Lagrangian of this theory is described in Eq.(2.1). Here Φ is a complex scalar field and the potential is a 'Mexican hat' potential with degenerate minima at $|\Phi| = \eta$.

When we traverse a closed path L in physical space it is possible for the field Φ to wrap once around the circle of minima of the potential, so, the phase of Φ develops a non-trivial winding, $\Delta\theta = 2\pi$. As indicated in Fig.(2.4), the far field will then take the form

$$\Phi = \eta e^{i\theta} \quad (2.29)$$

If we measure the winding on smaller loops L' bounded by the loop L , we can more accurately specify the actual location of the twist in the phase (see Fig.(2.5). At such a point, however, the phase of Φ varies by 2π and is no longer well-defined. This phase jump can only be resolved continuously if the field Φ rises to the top of

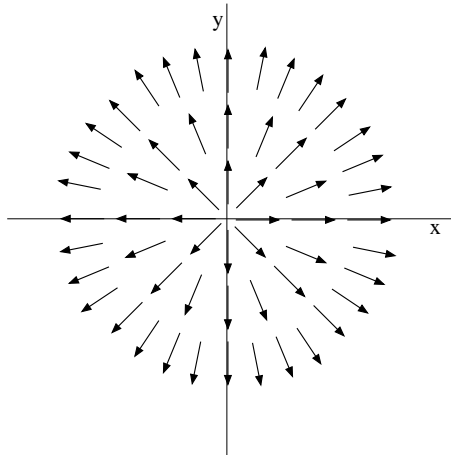


Figure 2.4: Field configuration for a vortex (string in 3 dimension)

the potential where it takes the value $\Phi = 0$. Consequently, there must be a non-zero energy density associated with the phase twist at the vortex core. We can see that such defects are constrained to be linear in three dimensions by noting that we must be able to locate the string core somewhere on any two-surface bounded by the closed path L . Note that string defect here arises as the vacuum manifold S^1 has closed curves which can't be smoothly shrunk to point, i.e, the first homotopy group of S^1 is non-trivial.

If the vacuum manifold is enlarged from a circle to a two-sphere S^2 , say by breaking $SO(3)$ with non-zero vev of a three component vector Φ to $SO(2)$, then non-trivial field configurations correspond to pointlike defects called monopoles. A vacuum manifold which is a three-sphere S^3 can, in turn, give rise to further topological objects called textures. Among a variety of other phenomena, successive symmetry breaking can produce hybrid defect combinations like domain walls bounded by strings or monopoles connected by strings. It is evident that the topology of the vacuum manifold is paramount in determining the nature of the defects that can appear at a symmetry breaking phase transition.

In the next section we will give an introduction to $Z(3)$ symmetry of QCD and the Polyakov loop order parameter for confinement and deconfinement phase transition and briefly discuss about the formation of $Z(3)$ walls and strings in this phase transition.

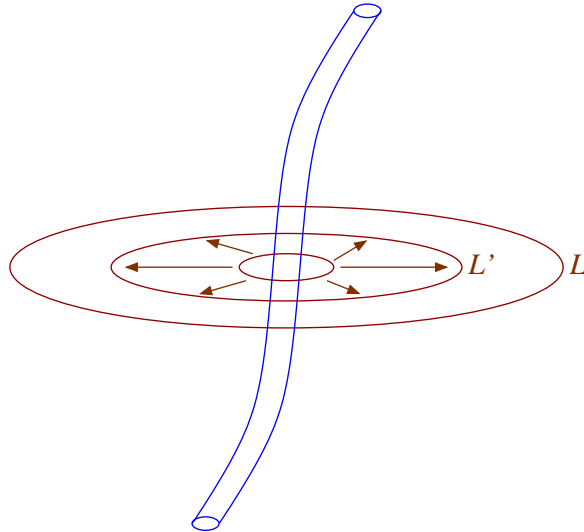


Figure 2.5: The string in three dimensions can always be located by encircling it with a closed loop L . A non-zero winding number in the phase as the loop is traversed discloses a string within.

2.3 $Z(N)$ Symmetry, Polyakov Loop, Domain walls and Strings

$SU(N)$ pure gauge theory has a $Z(N)$ global symmetry and the expectation value of Polyakov loop is the order parameter for $SU(N)$ pure gauge theory. However, Real QCD with dynamical quarks lacks an order parameter. The phase transitions of gauge theories without quarks are of especial interest, since the order parameter (Polyakov Loop), and many other aspects of the phase transition, can be characterized rigorously.

We briefly discuss pure $SU(N)$ gauge theory at finite temperature. We start with Euclidean path integral formulation of pure $SU(N)$ gauge theories and then discuss the $Z(N)$ symmetry [49] and its relationship to confinement and the spontaneous breaking of this symmetry at high temperature deconfined phase.

Consider a system of gluons at a non-zero temperature $T = 1/\beta$. The partition function is given by [50]

$$Z = \text{Tr}[\exp(-\beta H)P] \quad (2.30)$$

Here H is the Yang-Mills Hamiltonian operator and P is a projection operator. It reduces the trace over all states to those that are gauge invariant and hence physical. We note that $\exp(-\beta H)$ is similar to the time evolution operator $\exp(iHt)$, where β plays the role of an imaginary (Euclidean) time interval it . Our starting point is equilibrium thermodynamics which makes no reference to real time evolution and puts us directly into Euclidean space time.

The path integral expression for the partition function is,

$$Z = \int D[A] \exp(-S[A]), \quad (2.31)$$

$$S[A] = \int_0^\beta d\tau \int d^3x \operatorname{Tr} F_{\mu\nu} F^{\mu\nu} \quad (2.32)$$

is the Euclidean action.

$$F_{\mu\nu} = \partial_\mu A_\nu - \partial_\nu A_\mu + ig[A_\mu, A_\nu] \quad (2.33)$$

is the field strength resulting from the vector potential. Here g is the gauge coupling.

$$A_\mu = A_\mu^a \lambda^a / 2. \quad (2.34)$$

As a consequence of the trace in Eq.(2.30), the measure DA of the path integral contains fields that obey periodic boundary conditions,

$$A_\mu(\vec{x}, \beta) = A_\mu(\vec{x}, 0) \quad (2.35)$$

The proper boundary conditions in τ are dictated by the quantum statistics which the fields must satisfy. Though we are discussing pure SU(3) gauge theory without quarks, for latter purpose note that quarks must be anti-periodic in τ .

$$\Psi(\vec{x}, \beta) = -\Psi(\vec{x}, 0) \quad (2.36)$$

The action in Eq.(2.32) is invariant under gauge transformations

$${}^g A_\mu = g(A_\mu + i\partial_\mu)g^\dagger, \quad (2.37)$$

with $g(x) \in SU(N)$, and under this the field strength transforms as

$${}^g F_{\mu\nu} = g F_{\mu\nu} g^\dagger. \quad (2.38)$$

To maintain the boundary condition in Eq.(2.35) for the vector potential, we first consider gauge transformations that are strictly periodic in τ .

$$g(\vec{x}, \beta) = g(\vec{x}, 0) \quad (2.39)$$

Every quantity must be invariant under these gauge transformations. Moreover, there are topologically non-trivial transformations [49] that are periodic up to a constant twist matrix $z \in SU(N)$

$$g(\vec{x}, \beta) = z g(\vec{x}, 0) \quad (2.40)$$

Here, we note that the Euclidean action in Eq.(2.32) is in fact invariant under a larger group of non-trivial gauge transformations given above. The only physically relevant constraint is that $A_\mu(\vec{x}, \tau)$ remain periodic in τ when gauge transformed. Applying the transformations in Eq.(2.40) to periodic vector potential A_μ ,

$$\begin{aligned} {}^g A_\mu(\vec{x}, \beta) &= g(\vec{x}, \beta)(A_\mu(\vec{x}, \beta) + i\partial_\mu)g(\vec{x}, \beta)^\dagger \\ &= z g(\vec{x}, 0)(A_\mu(\vec{x}, 0) + i\partial_\mu)g(\vec{x}, 0)^\dagger z^\dagger \\ &= z {}^g A_\mu(\vec{x}, 0) z^\dagger. \end{aligned} \quad (2.41)$$

The gauge transformed vector potential ${}^g A_\mu$ satisfies the boundary condition in Eq.(2.35) only if

$$z {}^g A_\mu(\vec{x}, 0) z^\dagger = {}^g A_\mu(\vec{x}, 0), \quad (2.42)$$

This is true only if z commutes with ${}^g A_\mu$. This constrains the twist matrices z to be in the center $Z(N)$ of the gauge group $SU(N)$. By definition, the elements of the center commute with all group elements.

$$z = \exp(2\pi i n/N) \mathbf{1} \in Z(N), n \in \{0, 1, 2, \dots, N-1\} \quad (2.43)$$

$Z(N)$ is a cyclic group of order N . The elements are space time independent. The transformations of Eq.(2.40) represent a discrete global $Z(N)$ symmetry of the

action of Eq.(2.32). For QCD with $SU(3)$ gauge group, we have $Z(3)$ symmetry. Thus to conclude, finite temperature $SU(N)$ gauge theory (Euclidean action) has $Z(N)$ symmetry as the Euclidean action (or the partition function and hence the free energy) is invariant under $Z(N)$ transformations of the basic variables $A_\mu(x)$.

However, quark fields that transform in the fundamental representation of $SU(N)$ break this $Z(N)$ symmetry explicitly because they transform as

$${}^g\Psi = g\Psi \quad (2.44)$$

and are anti-periodic in Euclidean time as in Eq.(2.36). So, under the twisted transformation (Eq.(2.40), they transform into

$${}^g\Psi(\vec{x}, \beta) = g(\vec{x}, \beta)\Psi(\vec{x}, \beta) = -zg(\vec{x}, 0)\Psi(\vec{x}, 0) = -z {}^g\Psi(\vec{x}, 0). \quad (2.45)$$

To satisfy the boundary condition Eq.(2.36), one must restrict to $z = 1$, so that the $Z(N)$ symmetry is explicitly broken in presence of quarks.

The twisted transformations of Eq.(2.40) represent a global $Z(N)$ symmetry of the action of Eq.(2.32). Although the action is $Z(N)$ invariant, other quantities need not necessarily be invariant under the center symmetry transformations. In particular, unlike the local $SU(N)$ gauge symmetry, the global $Z(N)$ symmetry can break spontaneously and should not be considered as a subgroup of the local gauge group.

We will now discuss spontaneous breaking of this $Z(N)$ symmetry using Polyakov loop as an order parameter for $SU(N)$ pure gauge theory. Dynamical fields that transform in the fundamental representation break the $Z(N)$ symmetry explicitly. Here we limit ourselves to cases where such fields are not present. Still, even then one can use static fundamental charges to probe the physics of the adjoint dynamical fields. Static fundamental charges (infinitely heavy test quarks) will be related to the Polyakov loop (a Wilson loop closed around the periodic Euclidean time direction) [51, 52]

$$l(\vec{x}) = \text{Tr } \mathcal{P} \exp\left(ig \int_0^\beta d\tau A_0(\vec{x}, \tau)\right). \quad (2.46)$$

Here \mathcal{P} denotes path ordering of the exponential. The Polyakov loop is a complex scalar field that depends on the spatial position \vec{x} of the static color source. The

Polyakov loop transforms non-trivially under twisted $Z(N)$ transformations

$$\begin{aligned}
\mathcal{Q}(\vec{x}) &= \text{Tr } \mathcal{P} \exp\left(ig \int_0^\beta d\tau \mathcal{A}_0(\vec{x}, \tau)\right) \\
&= \text{Tr } [g(\vec{x}, \beta) \mathcal{P} \exp\left(ig \int_0^\beta d\tau A_0(\vec{x}, \tau)\right) g(\vec{x}, 0)^\dagger] \\
&= \text{Tr } [zg(\vec{x}, 0) \mathcal{P} \exp\left(\int_0^\beta d\tau A_0(\vec{x}, \tau)\right) g(\vec{x}, 0)^\dagger] = zl(\vec{x}). \tag{2.47}
\end{aligned}$$

On the other hand, it is invariant under strictly periodic gauge transformations (with $z = 1$) as it should as a gauge invariant physical quantity.

The partition function of a system of gluons in the presence of a static infinitely heavy test quark is given by [53]

$$Z_Q = \int DA l(\vec{x}) \exp(-S[A]). \tag{2.48}$$

The thermal expectation value of the Polyakov loop,

$$\langle l \rangle = \frac{1}{Z} \int DA l(\vec{x}) \exp(-S[A]) = \frac{Z_Q}{Z} \sim \exp(-\beta F), \tag{2.49}$$

is the ratio of the partition functions of the gluon systems with and without the external color source and hence measures the free energy F of the external static quark. At low temperatures color is confined and the free energy of a single quark is infinite ($F = \infty$). Consequently, in the confined phase $\langle l \rangle = 0$. At high temperatures, on the other hand, asymptotic freedom suggests that quarks and gluons become deconfined. Then F is finite and $\langle l \rangle = l_0 \neq 0$ in the deconfined phase. Since l transforms non-trivially under center symmetry transformations, a non-zero expectation value l_0 implies that the $Z(N)$ symmetry is spontaneously broken in the high temperature deconfined phase.

Due to the breaking of $Z(3)$ symmetry in deconfined phase in $SU(3)$ pure gauge theory, $Z(3)$ domain walls and strings are produced. $Z(3)$ domain walls are the solutions when one goes from one vacuum to another vacuum. So there are 3 different domain walls production in between 3 degenerate vacua. When three different domain walls meet, strings are produced. Surprisingly, these strings have confined phase within them while they are in QGP phase. We will study the formation and evolution of these in detail in next chapter.

Chapter 3

Simulation of $Z(3)$ Walls and Strings in a First Order Quark-Hadron Transition

3.1 Introduction

There has been a lot of progress in the search for the existence of the quark-gluon plasma (QGP) phase at relativistic heavy-ion collision experiments (RHICE) with the ongoing experiments at RHIC. We have discussed many signatures for the detection of the QGP phase in chapter 1 and these have been thoroughly investigated both theoretically and experimentally. Along with continued investigation of these important signatures of QGP, there is a need for investigating novel signals exploring qualitatively non-trivial features of the QGP phase.

With this view we focus on the non-trivial vacuum structure of the QGP phase which arises when one uses the expectation value of the Polyakov loop $l(x)$ as the order parameter for the confinement-deconfinement phase transition [53, 54]. As we have shown in chapter 2 of this thesis, this order parameter transforms non-trivially under the center $Z(3)$ of the color $SU(3)$ group and is non-zero above the critical temperature T_c . This breaks the global $Z(3)$ symmetry spontaneously above T_c , while the symmetry is restored below T_c in the confining phase where this order parameter vanishes. In the QGP phase, due to spontaneous breaking of the discrete

$Z(3)$ symmetry, one gets domain walls (interfaces) which interpolate between different $Z(3)$ vacua and strings at the junction of the three domain walls. The properties and physical consequences of these $Z(3)$ interfaces have been discussed in the literature [55]. It has been suggested that these interfaces should not be taken as physical objects in the Minkowski space [56]. Similarly, it has also been subject of discussion whether it makes sense to talk about this $Z(3)$ symmetry in the presence of quarks [57]. However, we will follow the approach where the presence of quarks is interpreted as leading to explicit breaking of $Z(3)$ symmetry, and this lifts the degeneracy of different $Z(3)$ vacua [58–61]. There is unique true vacuum and two metastable vacua because of explicit breaking due to quarks. Thus, with quarks, even planar $Z(3)$ interfaces do not remain static and move away from the region with the unique true vacuum. Here we will discuss mainly in the context of $SU(3)$ pure gauge theory.

Here we carry out numerical simulation of formation of these $Z(3)$ interfaces and associated strings at the initial confinement-deconfinement transition which is believed to occur during the pre-equilibrium stage in relativistic heavy-ion collision experiments [41]. For the purpose of numerical simulation we will model this stage as a quasi-equilibrium stage with an effective temperature which first rises (with rapid particle production) to a maximum temperature $T_0 > T_c$, where T_c is the critical temperature for the confinement-deconfinement phase transition, and then decreases due to continued plasma expansion.

Here we use the effective potential for the Polyakov loop expectation value $l(x)$ as proposed by Pisarski [59,60] to study the confinement-deconfinement (C-D) phase transition. Within this model, the C-D transition is weakly first order. Even though Lattice results show that quark-hadron transition is most likely a smooth cross-over at zero chemical potential, here we will use this first order transition model to discuss the dynamical details of quark-hadron transition. One reason for this is that our study is in the context of relativistic heavy-ion collision experiments (RHICE) where the baryon chemical potential is not completely zero. For not too small values of the chemical potential, the quark-hadron phase transition is expected to be of first order, so this may be the case relevant for us any way (especially when collision energy is not too high). Further, our main interest is in determining the structure of the network of $Z(3)$ domain walls and strings resulting during the phase transition. These

objects will form irrespective of the nature of the transition, resulting entirely from the finite correlation lengths in a fast evolving system, as shown by Kibble [9]. Essential ingredient of the Kibble mechanism is the existence of uncorrelated domains of the order parameter which result after every phase transition occurring in finite time due to finite correlation length. A first order transition allows easy implementation of the resulting domain structure especially when the transition proceeds via bubble nucleation. Here, we use the Polyakov loop model as in [59, 60] to model the phase transition and confine ourselves with temperature/time ranges so that the first order quark-hadron transition proceeds via bubble nucleation.

The $Z(3)$ wall network and associated strings formed during this early confinement-deconfinement phase transition evolve in an expanding plasma with decreasing temperature. Eventually when the temperature drops below the deconfinement-confinement phase transition temperature T_c , these $Z(3)$ walls and associated strings will melt away. However they may leave their signatures in the form of extended regions of energy density fluctuations (as well as P_T enhancement of heavy-flavor hadrons [62]). We make estimates of these energy density fluctuations which can be compared with the experimental data. Especially interesting will be to look for extended regions of large energy densities in space-time reconstruction of hadron density mainly using hydrodynamic models. In our model, we expect energy density fluctuations in event averages i.e representing high energy density regions of domain walls/strings, as well as event-by-event fluctuations as the number/geometry of domain walls/strings. The number of QGP bubbles, varies from one event to the other.

We also determine the distribution/shape of $Z(3)$ wall network and its evolution. In particular, our results provide an estimate of domain wall velocities to range from 0.5 to 0.8. These results provide crucial ingredients for a detailed study of the effects of collapsing $Z(3)$ walls on the P_T enhancement of heavy flavor hadrons [62, 63] in RHICE. We emphasize that the presence of $Z(3)$ walls and string may not only provide a qualitatively new signature for the QGP phase in these experiments, it may provide the first (and may be the only possible) laboratory study of such topological objects in a relativistic quantum field theory system.

3.2 The Effective Potential

We have discussed in chapter 2 about the order parameter for the confinement-deconfinement (C-D) phase transition as the expectation value of the Polyakov loop $l(x)$ which is defined as

$$l(x) = (1/N) \text{tr}(\text{Pexp}(ig \int_0^\beta A_0(x, \tau) d\tau)) \quad (3.1)$$

We also discussed that the expectation value of $l(x)$ is related to $e^{-\beta F}$ where F is the free energy of an infinitely heavy test quark. For temperatures below T_c , in the confined phase, the expectation value of Polyakov loop is zero corresponding to the infinite free energy of an isolated test quark. (Hereafter, we will use the same notation $l(x)$ to denote the expectation value of the Polyakov loop.) Hence the Z(N) symmetry is restored below T_c . Z(N) symmetry is broken spontaneously above T_c where $l(x)$ is non-zero corresponding to the finite free energy of the test quark. For QCD, $N = 3$, and we take the effective theory for the Polyakov loop as proposed by Pisarski [59, 60]. The effective Lagrangian density is given by

$$L = \frac{N}{g^2} |\partial_\mu l|^2 T^2 - V(l) \quad (3.2)$$

$V(l)$ is the effective potential for the Polyakov loop

$$V(l) = \left(\frac{-b_2}{2} |l|^2 - \frac{b_3}{6} (l^3 + (l^*)^3)\right) + \frac{1}{4} (|l|^2)^2 b_4 T^4 \quad (3.3)$$

The values of various parameters are fixed to reproduce the lattice results [64, 65] for pressure and energy density of pure SU(3) gauge theory. We make the same choice and give those values below. The coefficients b_3 and b_4 have been taken as, $b_3 = 2.0$ and $b_4 = 0.6016$. We will take the same value of b_2 for real QCD (with three massless quark flavors), while the value of b_4 will be rescaled by a factor of 47.5/16 to account for the extra degrees of freedom relative to the degrees of freedom of pure SU(3) gauge theory [64]. The coefficient b_2 is temperature dependent [64]. b_2 is taken as, $b_2(r) = (1 - 1.11/r)(1 + 0.265/r)^2(1 + 0.3/r)^3 - 0.487$, where r is taken as T/T_c . With the coefficients chosen as above, the expectation value of order parameter approaches to $x = b_3/2 + \frac{1}{2}\sqrt{b_3^2 + 4b_2(T = \infty)}$ for temperature $T \rightarrow \infty$. As in [60], we use the normalization such that the expectation value of order parameter l_0 goes to unity for

temperature $T \rightarrow \infty$. Hence the fields and the coefficients in $V(l)$ are rescaled as $l \rightarrow l/x$, $b_2(T) \rightarrow b_2(T)/x^2$, $b_3 \rightarrow b_3/x$ and $b_4 \rightarrow b_4x^4$ to get proper normalization of l_0 .

For the parameters chosen as above, the value of T_c is taken to be 182 MeV. We see that the b_3 term in Eq.(3.3) gives a $\cos(3\theta)$ term, leading to Z(3) degenerate vacua structure. We have shown 3D plot of the potential in Fig.(3.1) at a temperature of 200 MeV. The variation of effective potential with respect to temperature in the vicinity of T_c along $\theta = 0$ is shown in Fig.(3.2). Here, the shape of the potential is such that there exists a metastable vacuum upto a temperature ~ 250 MeV. Hence first order transition via bubble nucleation is possible only upto $T = 250$ MeV. This is a case of thick bubble formation because the height of central bump is very less than the energy difference between false and true vacua. We show the plot of $V(l)$ in $\theta = 0$ direction in Fig.(3.3a) for a value of temperature $T = 185$ MeV. This shows the metastable vacuum at $l = 0$. Fig.(3.3b) shows the structure of vacuum by plotting $V(l)$ as a function of θ for fixed l_0 , where l_0 is the vacuum expectation value of $V(l)$ at $T = 185$ MeV.

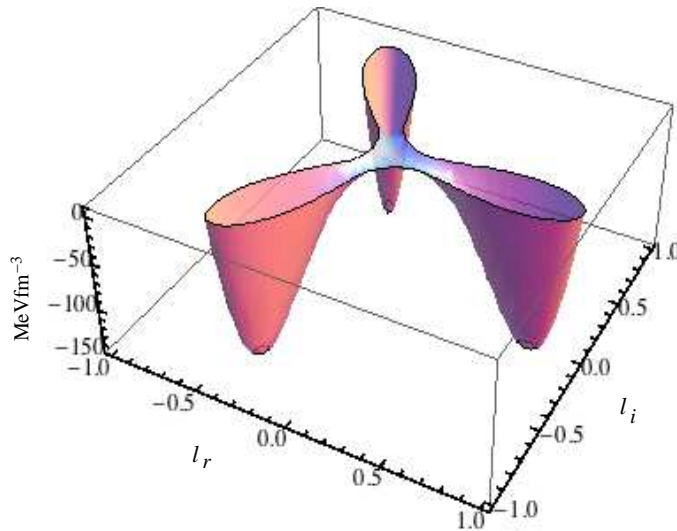


Figure 3.1:
Plot of $V(l)$ in 3-Dimension.

In Fig.(3.3b), the three degenerate vacua are separated by large barrier in between them. While going from one vacuum to another vacuum, the field configuration

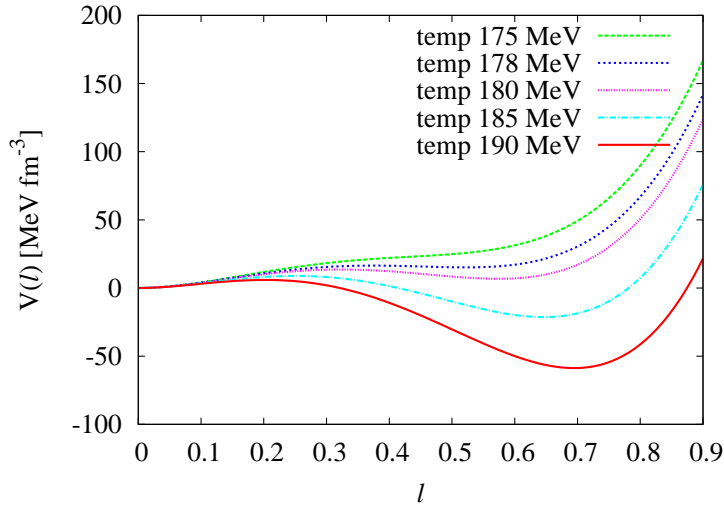


Figure 3.2:
Plot of $V(l)$ in $\theta = 0$ direction at different temperatures close to T_c

is determined from the field equations. For $SU(3)$ pure gauge theory case having degenerate vacua, there are time independent solutions which have planar symmetry. These solutions are called domain wall. For the non-degenerate case, as will be appropriate for the case when quarks are included as dynamical degrees of freedom in discussing the quark hadron transition, the solutions of the interfaces separating these vacua will be similar to the bounce solutions [44], though the standard bounce techniques need to be extended for the case of complex scalar field. The resulting planar domain wall solutions will not be static. As mentioned above, we will be neglecting such effects of quarks, and hence will discuss the case of degenerate vacua only.

3.3 Domain Wall And String Formation Via Kibble Mechanism

We have discussed the topological defect formation via Kibble mechanism in chapter 2. We now briefly describe domain wall and string formation in this scenario. Kibble

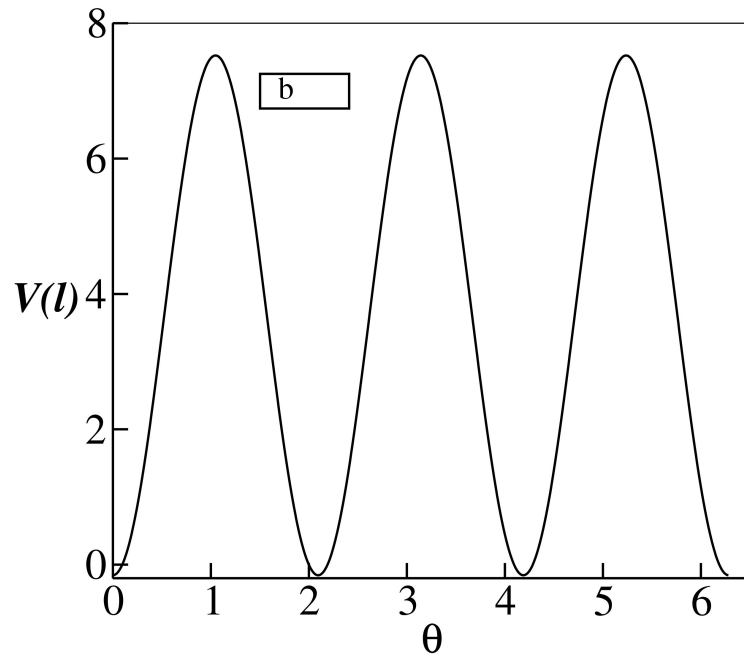
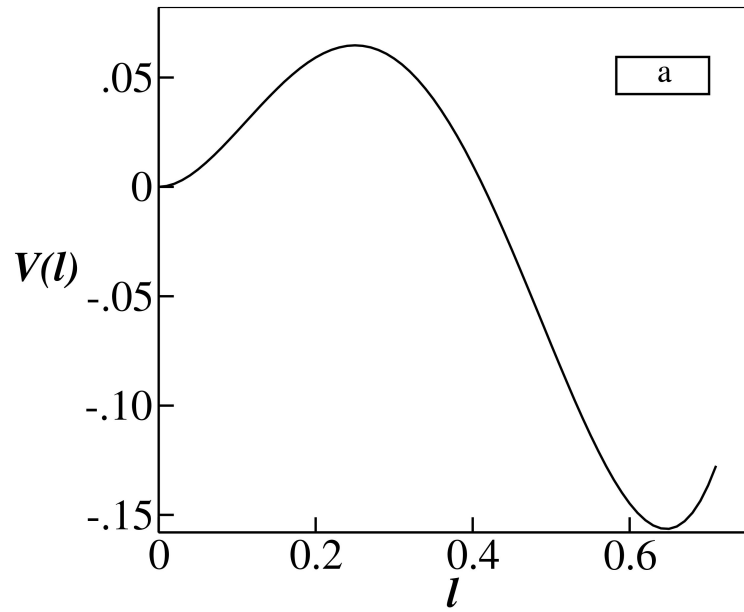


Figure 3.3:

(a) Plot of $V(l)$ in $\theta = 0$ direction for $T = 185 \text{ MeV}$ showing the metastable vacuum at $l = 0$. In (a) and (b), plots of V are given in units of T_c^4 . The value of critical temperature is taken to be $T_c \simeq 182 \text{ MeV}$. The $Z(3)$ structure of the vacuum can be seen in (b) in the plot of the potential $V(l)$ as a function of θ for fixed $|l| = l_0$. Here, l_0 corresponds to the absolute minimum of $V(l)$.

first gave a detailed theory of the formation of topological defects in symmetry breaking phase transitions in the context of the early universe [9]. Subsequently it was realized that the basic physics of Kibble mechanism is applicable to every symmetry breaking transition, from low energy physics of condensed matter systems to high energy physics relevant for the early universe [10].

We also described a simple technique of numerical implementation of Kibble mechanism by dividing the region in terms elementary domains of specific geometrical shape. We, however, will follow a more detailed simulation as in ref. [66] where the Kibble mechanism was implemented in the context of a first order transition. The first order transition proceeds through the nucleation of bubbles of true vacuum. Bubbles of true vacuum are determined from the bounce solution using Coleman's technique. The true vacuum bubbles are randomly nucleated in the background of false vacuum. Each bubble was taken to have the uniform orientation of the order parameter in the vacuum manifold, while the order parameter orientation varied randomly from one bubble to another. This provided the initial seed domains, as needed for the Kibble mechanism. Evolution of this initial configuration via the field equation led to expansion of bubbles which eventually coalesce and lead to the formation of topological defects at the junctions of bubbles when the order parameter develops appropriate variation (winding) in that region. Important thing is that in this case one does not need to assume anything like the geodesic rule. As different bubbles come into contact during their expansion, the value of the order parameter in the intermediate region is automatically determined by the field equations.

An important aspect of the Kibble mechanism is that it does not crucially depend on the dynamical details of the phase transition. Although the domain size depends on the dynamics of phase transitions, the defect number density (per domain) and type of topological defects produced via the Kibble mechanism depends only on the topology of order parameter space and spatial dimensions. If the vacuum manifold M has disconnected components, then domain walls form. If it is multiply connected (i.e., if M contains unshrinkable loops), strings will form. When M contains closed two surfaces which cannot be shrunk to a point, then monopoles will form in three dimensional physical space. In our case domain walls and string network will be produced in the QGP phase. As discussed above, domain walls arise due to interpolation

of field between different $Z(3)$ vacua. At the intersection of these interfaces, string is produced.

3.4 Critical Bubble Profile and Nucleation Probability

Since here we consider $Z(3)$ domain wall and string formation with the first order transition, such that the transition occurs via bubble nucleation. We have discussed in chapter 2, Coleman's technique of false vacuum decay which give rise to bubbles of true vacua.

Let's us first note general features of the dynamics of a standard first order phase transition at finite temperature via bubble nucleation. A region of true vacuum, in the form of a spherical bubble, appears in the background of false vacuum. The creation of bubble leads to the change in the free energy of the system as,

$$F(R) = F_s + F_v = 4\pi R^2 \sigma - \frac{4\pi}{3} R^3 \eta \quad (3.4)$$

where R is the radius of bubble, F_s is the surface energy contribution and F_v is the volume energy contribution. η is the difference of the free energy between the false vacuum and the true vacuum and σ is the surface tension which can be determined from the bounce solution.

A bubble of size R will expand or shrink depending on which process leads to lowering of the free energy given above. The bubbles of very small sizes will shrink to nothing since surface energy dominates. If the radius of bubble exceeds the critical size $R_c = \frac{2\sigma}{\eta}$, it will expand and lead to the transformation of the metastable phase into the stable phase.

Eq.(3.4) is useful for the so-called *thin wall* bubbles where there is a clear distinction between the surface contribution to the free energy and the volume contribution. For the temperature/time relevant for our case in relativistic heavy-ion collisions this will not be the case. Instead we will be dealing with the *thick wall* bubbles where surface and volume contributions do not have clear separations. We will determine the profiles of these thick wall bubbles numerically following the bounce technique [44]

as discussed in chapter 2 .

Here we note that for the effective potential in Eq.(3.3), the barrier between true vacuum and false vacuum vanishes at temperatures above about 250 MeV. So first order transition via bubble nucleation is possible only within the temperature range of $T_c \simeq 182 \text{ MeV} - 250 \text{ MeV}$. Above $T \simeq 250 \text{ MeV}$, spinodal decomposition will take place due to the roll down of field. We will discuss the spinodal decomposition scenario in the next chapter.

The initial confinement-deconfinement transition in the context of RHICE, has to be within the context of longitudinal expansion only, with negligible effects of the transverse expansion. However, Bjorken's longitudinal scaling model [31] cannot be applied during this pre-equilibrium phase, even with the assumption of quasi-equilibrium, unless one includes a heat source which could account for the increase of effective temperature during this phase to the maximum equilibrium temperature T_0 . As indicated above, this heat source can be thought of as representing the rapid particle production (with subsequent thermalization) during this early phase. We don't attempt to model such a source here. Instead, we simply use the field equations resulting from Bjorken's longitudinal scaling model for the evolution of the field configuration for the entire simulation, including the initial pre-equilibrium phase from $\tau = 0$ to $\tau = \tau_0$. The heating of the system until $\tau = \tau_0$ will be represented by the increase of the temperature upto $T = T_0$. Thus, during this period, the energy density and temperature evolution will not obey the Bjorken scaling equations [31]. After τ_0 , with complete equilibrium of the system, the temperature will decrease according to the equations in the Bjorken's longitudinal scaling model.

We will take the longitudinal expansion to only represent the fact that whatever bubbles will be nucleated, they get stretched into ellipsoidal, and eventually cylindrical, shapes during the longitudinal expansion. Here we ignore the boundary effects in the longitudinal direction. The transverse expansion of the bubble should then proceed according to relative pressure difference between the false vacuum and the true vacuum as in the usual theory of first order phase transition. We will neglect transverse expansion for the system, and focus on the mid rapidity region. With this picture in mind, we will work with effective 2+1 dimensional evolution of the field

configuration, (neglecting the transverse expansion of QGP). However, for determining the bubble profile and the nucleation probability of bubbles, one must consider full 3+1 dimensional case as bubbles are nucleated with full 3-dimensional profiles in the physical space. The bubbles will have sizes of about 1 - 1.5 fm radius.

The initial collision region during the pre-equilibrium phase also to be of the order of 1-2 fm in the longitudinal direction, it looks plausible that the nucleation of 3-dimensional bubble profile as discussed above may provide a good approximation. Of course the correct thing is to consider the bounce solutions for rapidly longitudinally expanding plasma.

We neglect transverse expansion here, which is a good approximation for the early stages when wall/string network forms. However, this will not be a valid approximation for later stages, especially when temperature drops below T_c and wall/string network melts. The way to account for the transverse expansion in the context of our simulation will be to take a lattice with much larger physical size than the initial QGP system size, and allow free boundary conditions for the field evolution at the QGP system boundary (which will still be deep inside the whole lattice). This will allow the freedom for the system to expand in the transverse direction automatically. With a suitable prescription of determining temperature from local energy density (with appropriate account of field contributions and expected contribution from a plasma of quarks and gluons) in a self consistent manner, the transverse expansion can be accounted for in this simulation. In chapter 5 of this thesis, we have studied the transverse expansion keeping entropy density times proper time fixed.

The initial system (of nucleons) before the collision was at zero temperature with the order parameter $l(x) = 0$, and will be superheated as the temperature rises above the critical temperature. It can then tunnel through the barrier to the true vacuum, representing the deconfined QGP phase. At zero temperature, the tunneling probability can be calculated by finding the bounce solution which is a solution of the 4-dimensional Euclidean equations of motion. However, at finite temperature, this 4-dimensional theory will reduce to an effectively 3 Euclidean dimensional theory if the temperature is sufficiently high, which we will take to be the case.

For this finite temperature case, the tunneling probability per unit volume per unit time in the high temperature approximation is given by [45]

$$\Gamma = A e^{-S_3(l)/T} \quad (3.5)$$

where $S_3(l)$ is the 3-dimensional Euclidean action for the Polyakov loop field configuration that satisfies the classical Euclidean equations of motion. The condition for the high temperature approximation to be valid is that $T \gg r_0^{-1}$, where r_0 is the radius of the critical bubble in 3 dimensional Euclidean space. The values of temperature for our case (relevant for bubble nucleation) will be above $T = T_c = 182$ MeV. As we will see, the bubble radius will be larger than 1.5 fm ($\sim (130 \text{ MeV})^{-1}$) which justifies our use of high temperature approximation to some extent. The determination of the pre-exponential factor is a non-trivial issue and we will discuss it below. Recall from chapter 2 that the dominant contribution to the exponential term in Γ comes from the least action $O(3)$ symmetric configuration which is a solution of the following equation (for the Lagrangian in Eq.(3.2)).

$$\frac{d^2 l}{dr^2} + \frac{2}{r} \frac{dl}{dr} = \frac{g^2}{2NT^2} V'(l) \quad (3.6)$$

where $r \equiv r_E = \sqrt{\vec{x}^2 + t_E^2}$, subscript E denoting the coordinates in the Euclidean space.

The boundary conditions imposed on l are

$$l = 0 \quad \text{as} \quad r \rightarrow \infty \quad \text{and} \quad \frac{dl}{dr} = 0 \quad \text{at} \quad r = 0 \quad (3.7)$$

Bounce solution of Eq.(3.6) can be analytically obtained in the *thin wall* limit where the difference in the false vacuum and the true vacuum energy is much smaller than the barrier height. We have discussed this in chapter 2. This situation will occur for very short time duration near $T = T_c$ for the effective potential in Eq.(3.3). However, as the temperature is rapidly evolving in the case of RHICE, there will not be enough time for nucleating such large bubbles (which also have very low nucleation rates due to having large action). Thus the case relevant for us is that of thick wall bubbles whose profile has to be obtained by numerically solving Eq.(3.6).

As we have mentioned earlier, in the high temperature approximation the theory effectively becomes 3 (Euclidean) dimensional. For a theory with one real scalar field in three Euclidean dimensions the pre-exponential factor arising in the nucleation

rate of critical bubbles has been estimated, see ref. [45]. The pre-exponential factor obtained from [45] for our case becomes

$$A = T^4 \left(\frac{S_3(l)}{2\pi T} \right)^{3/2} \quad (3.8)$$

It is important to note here that the results of [45] were for a single real scalar field and here we assume that it will still be valid for our the complex field theory case.

Another approach for the pre-exponential factor in Eq.(3.5) is obtained from the nucleation rate of bubbles per unit volume for a liquid-gas phase transition as given in ref. [67,68],

$$\Gamma = \frac{\kappa}{2\pi} \Omega_0 e^{-\Delta F/T} \quad (3.9)$$

Here κ is the dynamical prefactor which determines the exponential growth rate of critical droplets. Ω_0 is a statistical prefactor which measures the available phase space volume. The exponential term is the same as in Eq.(3.5) with ΔF being the change in the free energy of the system due to the formation of critical droplet. This is the same as S_3 in Eq.(3.5). The bubble grows beyond the critical size when the latent heat is conducted away from the surface into the surrounding medium which is governed by thermal dissipation and viscous damping. For our case, in the general framework of transition from a hadronic system to the QGP phase, we will use the expression for the dynamical prefactor from ref. [69]

$$\kappa = \frac{2\sigma}{(\Delta\omega)^2 R_c^3} (\lambda T + 2(\frac{4}{3}\eta + \zeta)) \quad (3.10)$$

Here σ is the surface tension of the bubble wall, $\Delta\omega$ is the difference in the enthalpy densities of the QGP and the hadronic phases, λ is thermal conductivity, R_c is the critical bubble radius, and η and ζ are shear and bulk viscosities. ζ will be neglected as it is much smaller than η . For λ and η , the following parameterizations are used [69,70].

$$\eta = \left(\frac{1700}{T^2} \right) \left(\frac{n}{n_0} \right)^2 + \left(\frac{22}{1 + T^2/1000} \right) \left(\frac{n}{n_0} \right)^{0.7} + \frac{5.8T^{1/2}}{1 + 160/T^2} \quad (3.11)$$

$$\lambda = \left(\frac{0.15}{T}\right) \left(\frac{n}{n_0}\right)^{1.4} + \left(\frac{0.02}{1 + T^4/(7 \times 10^6)}\right) \left(\frac{n}{n_0}\right)^{0.4} + \frac{0.0225T^{1/2}}{1 + 160/T^2} \quad (3.12)$$

Here n/n_0 is the ratio of the baryon density of the system to the normal nuclear baryon density, T is in MeV, η is in MeV/fm²c, and λ is in c/fm². With this, the rate in Eq.(3.9) is in fm⁻⁴. For the range of temperatures of our interest ($T > 160\text{MeV}$), and for the low baryon density central rapidity region under consideration, it is the last n independent term for both η and κ which dominates, and we will use these terms only for calculating η and κ for our case.

For the statistical prefactor, we use the following expression [69]

$$\Omega_0 = \frac{2}{3\sqrt{3}} \left(\frac{\sigma}{T}\right)^{3/2} \left(\frac{R_c}{\xi_{had}}\right)^4 \quad (3.13)$$

The correlation length in the hadronic phase, ξ_{had} , is expected to be of order of 1 fm and we will take it to be 0.7 fm [69]).

We will present estimates of the nucleation rates from Eq.(3.5) as well as Eq.(3.9). One needs to determine the critical bubble profile and its 3-dimensional Euclidean action S_3 (equivalently, ΔF in Eq.(3.9)). We solve Eq.(3.6) using the fourth order Runge-Kutta method with appropriate boundary conditions Eq.(3.7), to get the profile of critical bubble [66]. The critical bubble profiles (for the 3+1 dimensional case) are shown in Fig.(3.4a) for different temperatures. The bubble size decreases as temperature increases, since the energy difference between true vacuum and false vacuum increases (relative to the barrier height) as temperature increases. We choose a definite temperature $T = 200$ MeV for the nucleation of bubbles, which is suitably away from T_c to give acceptable bubble size and nucleation probabilities for the relevant time scale. Making T larger (up to $T = 250$ MeV when the barrier disappears) leads to similar bubble profile, and the nucleation probability of same order.

We are calculating bubble profiles using Eq.(3.6) relevant for the 3+1 dimensional case, however, the field evolution is done using 2+1 dimensional equations as appropriate for the mid rapidity region of rapidly longitudinally expanding plasma. In Fig.(3.4b) solid curve shows the critical bubble for the 3+1 dimensional case (which for finite temperature case becomes 3 Euclidean dimensional) for $T = 200$ MeV and

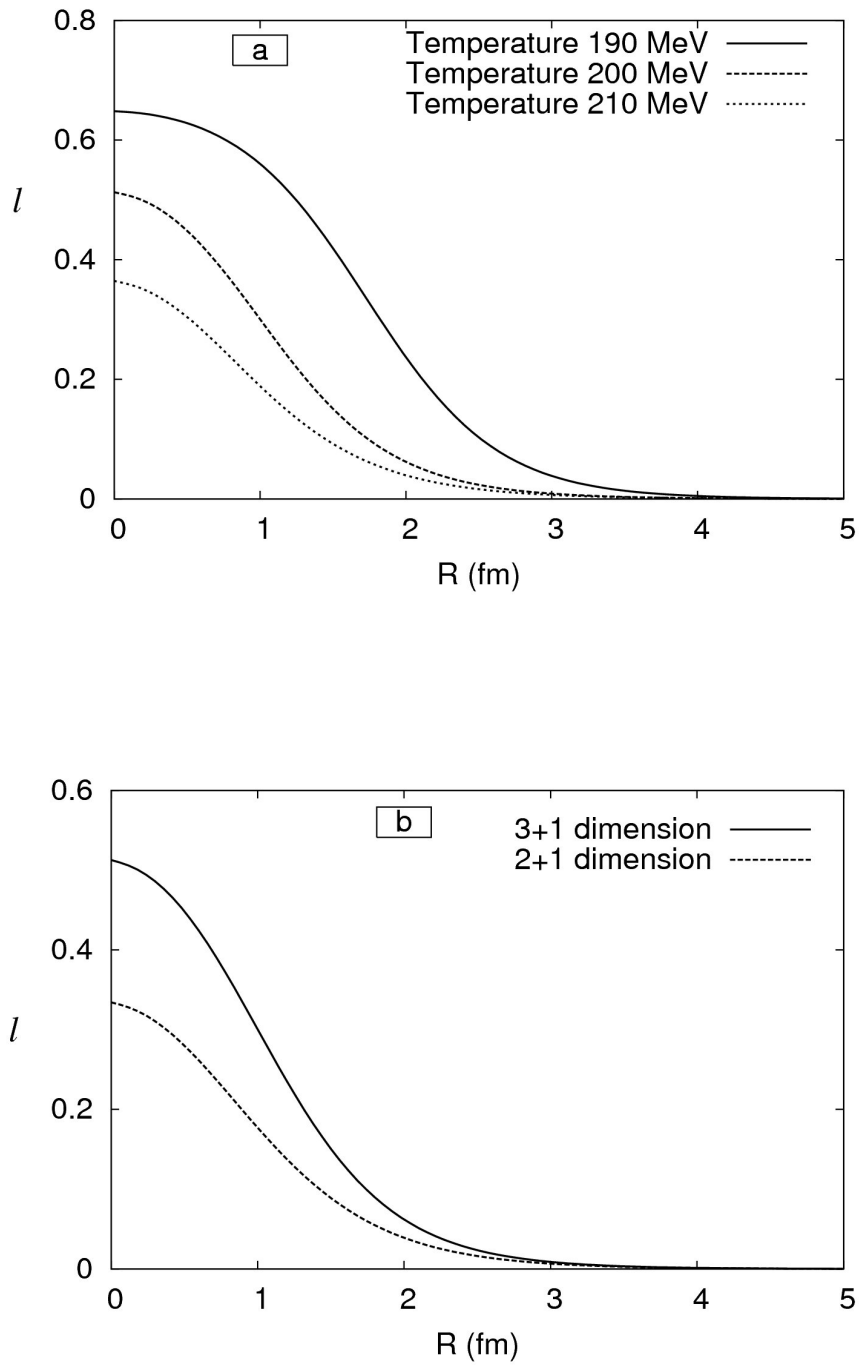


Figure 3.4:

(a) Critical bubble profiles for different values of the temperature. (b) Solid curve shows the critical bubble for the 3+1 dimensional case (which for finite temperature case becomes 3 Euclidean dimensional) for $T = 200$ MeV and the dotted curve shows the same for 2+1 dimensional case (i.e. 2 Euclidean dimensions for finite temperature case).

the dashed curve shows the same for 2+1 dimensional case (i.e. 2 Euclidean dimensions for finite temperature case). It is clear that the 3 dimensional bubble is of supercritical size and will expand when evolved with 2+1 dimensional equations. This avoids the artificial construction of suitable supercritical bubbles which can expand and coalesce as was done in ref. [66]. (Recall that for the finite temperature case, a bubble of exact critical size will remain static when evolved by the field equations. In a phase transition, bubbles with somewhat larger size than the critical size expand, while those with smaller size contract.)

For the bubble profile given by the solid curve in Fig.(3.4b), the value of the action $S_3(l)$ is about 240 MeV. Using Eq.(3.5) for the nucleation rate, we find that the nucleation rate of QGP bubbles per unit time per unit volume is of the order of $0.025 fm^{-4}$. The thermalization time for QGP phase is of the order of 1 fm at RHIC (say, for Au-Au collision at 200 GeV energy). Hence the time available for the nucleation of QGP bubbles is at most about 1 fm. We take the region of bubble nucleation to be of thick disk shape with the radius of the disk (in the transverse direction) of about 8 fm and the thickness of the disk (in the longitudinal direction) of about 1 fm. Total space-time volume available for bubble nucleation is then about $200 fm^4$ (even less than this). For the case of Eq.(3.5), net number of bubbles is then equal to 5.

For the case of the nucleation rate given by Eq.(3.9), one needs an estimate of the critical bubble size R_c as well as bubble surface energy σ , (along with other quantities like λ etc. as given by Eqs.((3.10)-(3.13)). Determination of R_c is somewhat ambiguous here as the relevant bubbles are thick wall bubbles as seen in Fig.(3.4). Here there is no clear demarcation between the core region and the surface region which could give an estimate of R_c . Essentially, there is no core at all and the whole bubble is characterized by the overlap of bubble wall region. We can take, as an estimate for the bubble radius R_c any value from 1 fm - 1.5 fm. It is important to note here that this estimate of R_c is only for the calculation of nucleation rate Γ , and not for using the bubble profile for actual simulation. When bubbles are nucleated in the background of false vacuum with $l = 0$, a reasonably larger size of the bubble is used so that cutting off the profile at that radius does not lead to computational errors and field evolution remains smooth.

Once we have an estimate of R_c , we can then estimate the surface tension σ (which also is not unambiguous here) as follows. With the realization that essentially there is no core region for the bubbles in Fig.(3.4), we say that the entire energy of the bubble (i.e. the value of S_3) comes from the surface energy. Then we write

$$4\pi R_c^2 \sigma = S_3 \quad (3.14)$$

For $S_3 = 240$ MeV, we get $\sigma = 8$ MeV/fm² if we take $R_c = 1.5$ fm. With $R_c = 1.0$ fm, we get $\sigma = 20$ MeV/fm².

Number of bubbles expected can now be calculated for the case when nucleation rate is given by Eq.(3.9). We find number of bubbles to be about 10^{-4} with R_c taken as 1.5 fm. This is in accordance with the results discussed in ref. [69]. The bubble number increases by about a factor 5 if R_c is taken to be about 1 fm. Thus, with the estimates based on Eq.(3.9), bubble nucleation is a rare event for the time available for RHICE.

As we have mentioned above, for us the bubble nucleation on one hand represents the possibility of actual dynamics of a first order transition, while on the other hand, it represents the generic properties of the domain structure arising from a C-D transition, which may very well be a cross-over, occurring in a finite time. With this view, and with various uncertainties in the determination of pre-exponential factors in the nucleation rate, we will consider a larger number of bubbles also and study domain wall and string production. First we will consider nucleation of 5 bubbles and then we will consider nucleation of 9 bubbles to get a better network of domain walls and strings.

3.5 Numerical Techniques

In our simulation critical bubbles are nucleated at a time when the temperature T crosses the value $T = 200$ MeV during the initial stage between $\tau = 0$ to $\tau = \tau_0 = 1$ fm (during which we have modeled the system temperature to increase linearly from 0 to T_0). We take $T_0 = 400$ MeV so bubble nucleation stage is taken to be at $\tau = 0.5$ fm when T reaches the value 200 MeV. Again, this is an approximation since in realistic case bubbles will nucleate over a span of time given by the (time dependent)

nucleation rate, which could lead to a spectrum of sizes of expanding bubbles at a given time. However, due to very short time available to complete the nucleation of QGP bubbles in the background of confined phase, bubbles will have very little time to expand during the nucleation period of all bubbles (especially as initial bubble expansion velocity is zero). Thus it is reasonable to assume that all the bubbles nucleate at the same time.

After nucleation, bubbles are evolved by the time dependent equations of motion in the Minkowski space [31] as appropriate for Bjorken's longitudinal scaling model.

$$\ddot{l}_i + \frac{\dot{l}_i}{\tau} - \frac{\partial^2 l_i}{\partial x^2} - \frac{\partial^2 l_i}{\partial y^2} = \frac{-\partial V(l)}{\partial l_i}, \quad i = 1, 2 \quad (3.15)$$

with $\dot{l} = 0$ at $\tau = 0$. Here $l = l_1 + il_2$, and dot indicates derivative with respect to the proper time τ .

The bubble evolution was numerically implemented by a stabilized leapfrog algorithm of second order accuracy both in space and in time with the second order derivatives of l_i approximated by a diamond shaped grid. Here we follow the approach described in [66] to simulate the first order transition. We need to nucleate several bubbles randomly choosing the corresponding $Z(3)$ vacua for each bubble. This is done by randomly choosing the location of the center of each bubble with some specified probability per unit time per unit volume. Before nucleating a bubble, it is checked if the relevant region is in the false vacuum (i.e. it does not overlap with some other bubble already nucleated). In case there is an overlap, the nucleation of the new bubble is skipped. The orientation of l inside each bubble is taken to randomly vary between the three $Z(3)$ vacua.

For representing the situation of relativistic heavy-ion collision experiments, the simulation of the phase transition is carried out by nucleating bubbles on a square lattice with physical size of 16 fm within a circular boundary (roughly the Gold nucleus size). We use fixed boundary condition, free boundary condition, as well as periodic boundary condition for the square lattice. To minimize the effects of boundary (reflections for fixed boundary, mirror reflections for periodic boundary conditions), we present results for free boundary conditions (for other cases, the qualitative aspects of our results remain unchanged). Even for free boundary conditions, spurious partial reflections occur, and to minimize these effects we use a thin strip (of 10 lattice

points) near each boundary where extra dissipation is introduced.

We use 2000×2000 lattice. For the physical size of 16 fm, we have $\Delta x = 0.008$ fm. To satisfy the Courant stability criteria, we use $\Delta t = \Delta x/\sqrt{2}$, as well as $\Delta t = 0.9\Delta x/\sqrt{2}$. For Au-Au collision at 200 GeV, the thermalization is expected to happen within 1 fm time. As mentioned above, in this pre-equilibrium stage, we model the system as being in a quasi-equilibrium stage with a temperature which increases linearly with time (for simplicity). The temperature of the system is taken to reach upto 400 MeV in 1 fm time, starting from $T = 0$. After $\tau = \tau_0 = 1$ fm, the temperature decreases due to continued longitudinal expansion, i.e.

$$T(\tau) = T(\tau_0) \left(\frac{\tau_0}{\tau} \right)^{1/3} \quad (3.16)$$

The stability of the simulation is checked by checking the variation of total energy of the system during the evolution. The energy fluctuation remains within few percent, with no net increase or decrease in the energy (for fixed and periodic boundary conditions, and without the dissipative \dot{l} term in Eq.(3.15)) showing the stability of the simulation.

The bubbles grow and eventually start coalescing, leading to a domain like structure. Domain walls are formed between regions corresponding to different $Z(3)$ vacua, and strings form at junctions of $Z(3)$ domain walls. Here, the domain wall network is formed here in the transverse plane, appearing as curves. These are the cross-sections of the walls which are formed by elongation (stretching) of these curves in the longitudinal direction into sheets. At the intersection of these walls, strings form. In the transverse plane, these strings look like vortices, which will be elongated into strings in the longitudinal direction.

3.6 With Quarks

To see the importance of these effects we need an estimate of the explicit symmetry breaking term arising from inclusion of quarks. For this we use the estimates given in [61, 71]. Even though the estimates in ref. [71] are given in the high temperature limit, we will use these for temperatures relevant for our case, i.e. $T \simeq 200 - 400$ MeV, to get some idea of the effects of the explicit symmetry breaking. The difference

in the potential energy between the true vacuum with $l = 1$ and the other two vacua ($l = e^{i2\pi/3}$, and $l = e^{i4\pi/3}$, which are degenerate with each other) is estimated in ref. [71] to be,

$$\Delta V \sim \frac{2}{3}\pi^2 T^4 \frac{N_l}{N^3} (N^2 - 2) \quad (3.17)$$

where N_l is the number of massless quarks. If we take $N_l = 2$ then $\Delta V \simeq 3T^4$. At the bubble nucleation temperature (which we have taken to be about $T = 200$ MeV, the difference between the false vacuum and the true vacuum is about 150 MeV/fm³ while ΔV at $T = 200$ MeV is about four times larger, equal to 600 MeV/fm³. As T approaches T_c , this difference will become larger as the metastable vacuum and the stable vacuum become degenerate at T_c , while ΔV remains non-zero. For T near 250 MeV (where the barrier between the metastable vacuum and the stable vacuum disappears), ΔV becomes almost comparable to the difference between the potential energy of the false vacuum (the confining vacuum) and the true vacuum (deconfined vacuum).

It does not seem reasonable that at temperatures of order 200 MeV a QGP phase (with quarks) has higher free energy than the hadronic phase. This situation can be avoided if the estimates of Eq.(3.17) are lowered by about a factor of 5 so that these phases have lower free energy than the confining phase. A more desirable situation will be when ΔV approaches zero as the confining vacuum and the deconfining (true) vacuum become degenerate at T_c . It is in the spirit of the expectation that explicit breaking of $Z(3)$ is small near T_c for finite pion mass [61]. We also have shown that the nucleation probabilities of metastable vacua are similar to the true vacuum in presence of quarks. This may not be very unreasonable as for thick wall bubbles thermal fluctuations may be dominant in determining the small number of bubbles nucleated during the short span of time available. For very few bubbles nucleated, there may be a good fraction of events where different $Z(3)$ vacua may occur in good fraction. Also note that the pre-exponential factor for the bubble nucleation rate of Eq.(3.5), as given in Eq.(3.8) increases with the value of $S_3(l)$. Thus, for the range of values of $S_3(l)$ for which the exponential factor in Eq.(3.5) is of order 1, which is likely in our case, the nucleation rate may not decrease with larger values of $S_3(l)$, i.e. for the $Z(3)$ vacua with higher potential energies than the true vacuum. (Of course

for very large values of $S_3(l)$ the exponential term will suppress the nucleation rate.) Thus our assumption of neglecting quark effects for the bubble nucleation rate may not be unreasonable.

We now consider the effect of non-zero ΔV , as in Eq.(3.17), on the evolution of closed domain walls. The temperature range relevant for our case is $T = 200 - 400$ MeV. The surface tension of Z(3) walls to be about 0.34 and 7.0 GeV/fm² for $T = 200$ and 400 MeV respectively. The effects of quarks will be significant if a closed spherical wall (with true vacuum inside) starts expanding instead of collapsing. Again, using the bubble free energy Eq.(3.4), with $\eta = \Delta V$ and σ as the surface energy of the interface, we see that the critical radius R^* of the spherical wall is

$$R^* = \frac{2\sigma}{\eta} \simeq 2\sigma/3T^4 \quad (3.18)$$

For $T = 200$ MeV and 400 MeV we get $R^* \simeq 1$ and 1.5 fm respectively. Though these values are not large, these are not too small either when because of the fact that relevant sizes and times for RHICE are of order few fm anyway. The values of R^* we estimated here are very crude as for these sizes wall thickness is comparable to R^* hence application of Eq.(3.4), separating volume and surface energy contributions, is not appropriate. further, as we discussed above, the estimate in Eq.(3.17) which is applicable for high temperature limit, seems an over estimate by about an order of magnitude at these temperatures. Thus uncertainties of factors of order 1 may not be unreasonable to expect. In that case the dynamics of closed domain walls of even several fm diameter will not be affected by the effects of quarks via Eq.(3.17).

3.7 Results of the Simulation

We have mentioned above that the number of bubbles expected to form in RHICE is small. We first present and discuss the case of 5 bubbles which is more realistic from the point of view of nucleation estimates given by Eq.(3.5). Note that a domain wall will form even if only two bubbles nucleate with different Z(3) vacua. However, we can see QGP string formation, when at least three bubbles of different phase nucleate. Next we will discuss the case of 9 bubbles which is a much more optimistic estimate of the nucleation rate (even for Eq.(3.5)). Alternatively, this case can be taken as

better representation of the case when the transition is a cross over and bubbles only represent a means for developing a domain structure expected after the cross-over is completed. In this case only relevant energy density fluctuations, as discussed below, will be those arising from $Z(3)$ walls and strings, and not the ones resulting from bubble wall coalescence.

3.7.1 formation and motion of extended walls

Fig.(3.5-3.9) show the results of simulation when five bubbles are nucleated with random choices of different $Z(3)$ vacua inside each bubble. Fig.(3.5) shows a time sequence of surface plots of the order parameter $l(x)$ in the two dimensional lattice. Fig.(3.5a) shows the confining vacuum with $l = 0$ at $\tau = 0.5$ fm with the temperature $T = 200$ MeV. Here for initial 1 fm time the temperature is taken to linearly increase from zero to $T_0 = 400$ MeV. The radial profile of each bubble is truncated with appropriate care of smoothness on the lattice for proper time evolution. Fig.(3.5b) shows the profile of each bubble at $\tau = 1.5$ fm showing the expansion of the bubbles. Near the outer region of a bubble the field grows more quickly towards the true vacuum. If bubbles expand for long time then bubble walls become ultra-relativistic and undergo large Lorentz contraction. This causes problem in simulation (see, e.g. [66]). In our case this situation arises at outer boundaries (for the inner regions bubbles collide quickly). For outer regions also it does not cause serious problem because of the use of dissipative boundary strip.

Figs. (3.5c-3.5i) show plots of $l_0 - l$ clearly showing formation of domain walls and strings (junctions of three walls). Here l_0 is a reference vacuum expectation value of l calculated at the maximum temperature $T = T_0 = 400$ MeV. Formation of domain walls, extending through the entire QGP region, is directly visible from Fig.(3.5e) (at $\tau = 4$ fm) onwards. The temperature drops to below $T_c \simeq 182$ MeV at $\tau \simeq 10.5$ fm. The last plot in Fig.(3.5i) is at $\tau = 13.7$ fm when the temperature $T = 167$ MeV, clearly showing that the domain walls have decayed away in the confined phase and the field is fluctuating about $l = 0$.

In Fig.(3.5f-3.5h) we see two junctions of three domain walls where the QGP strings form. This is seen more clearly in Fig.(3.6) where the phase θ of l is plotted. Here the convention is that θ is the angle of the arrow from the positive X axis. The

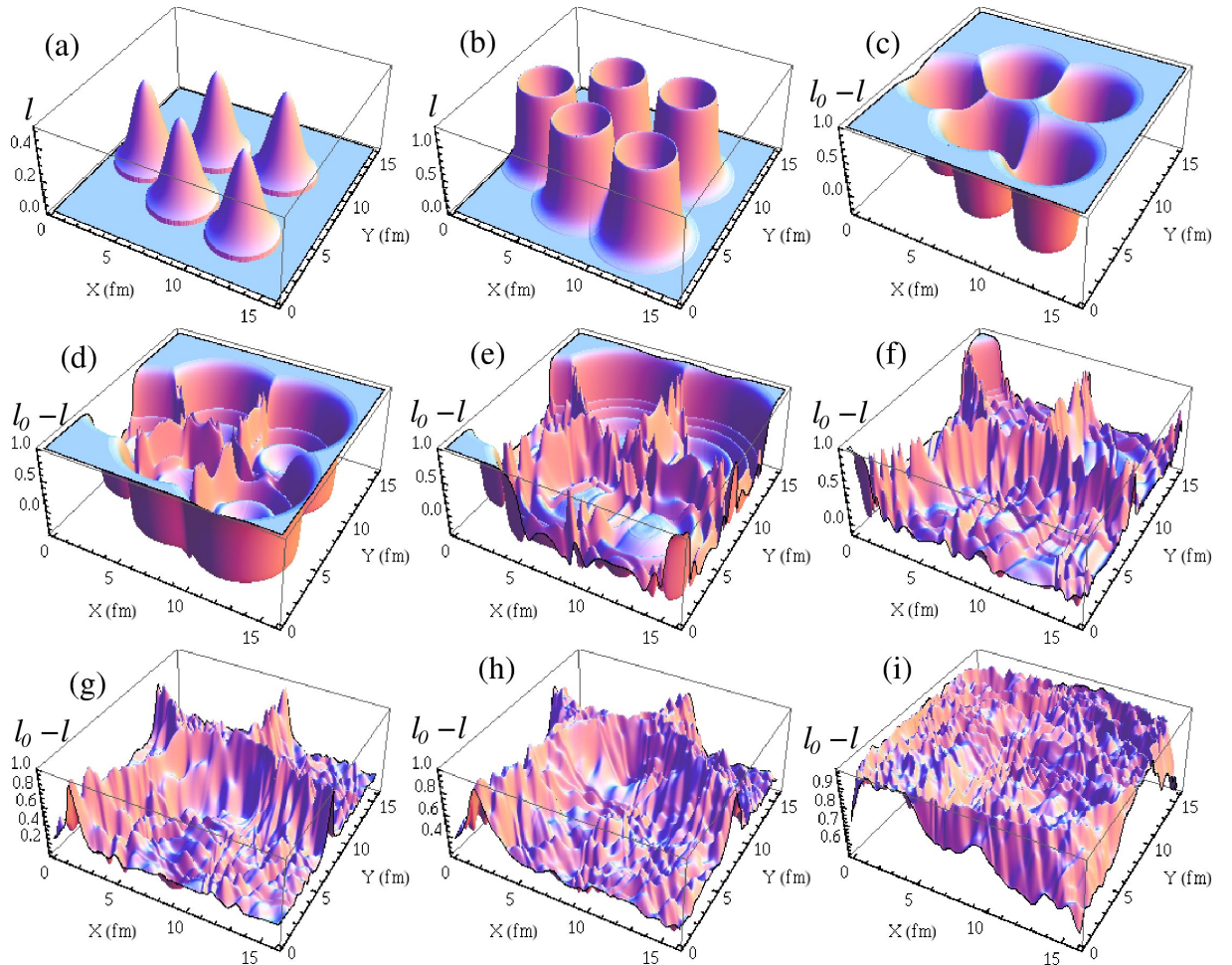


Figure 3.5:

(a) and (b) show plots of profiles of l at $\tau = 0.5$ fm and 1.5 fm respectively. (c)-(i) show plots of $l_0 - l$ at $\tau = 1.5, 2.5, 4.0, 6.0, 9.0, 11.0,$ and 13.7 fm. T drops to below T_c around at $\tau = 10.5$ fm and $T = 167$ MeV at $\tau = 13.7$ fm. Formation of domain walls and string and antistring (at junctions of three walls) can be seen in the plots in (e) - (h).

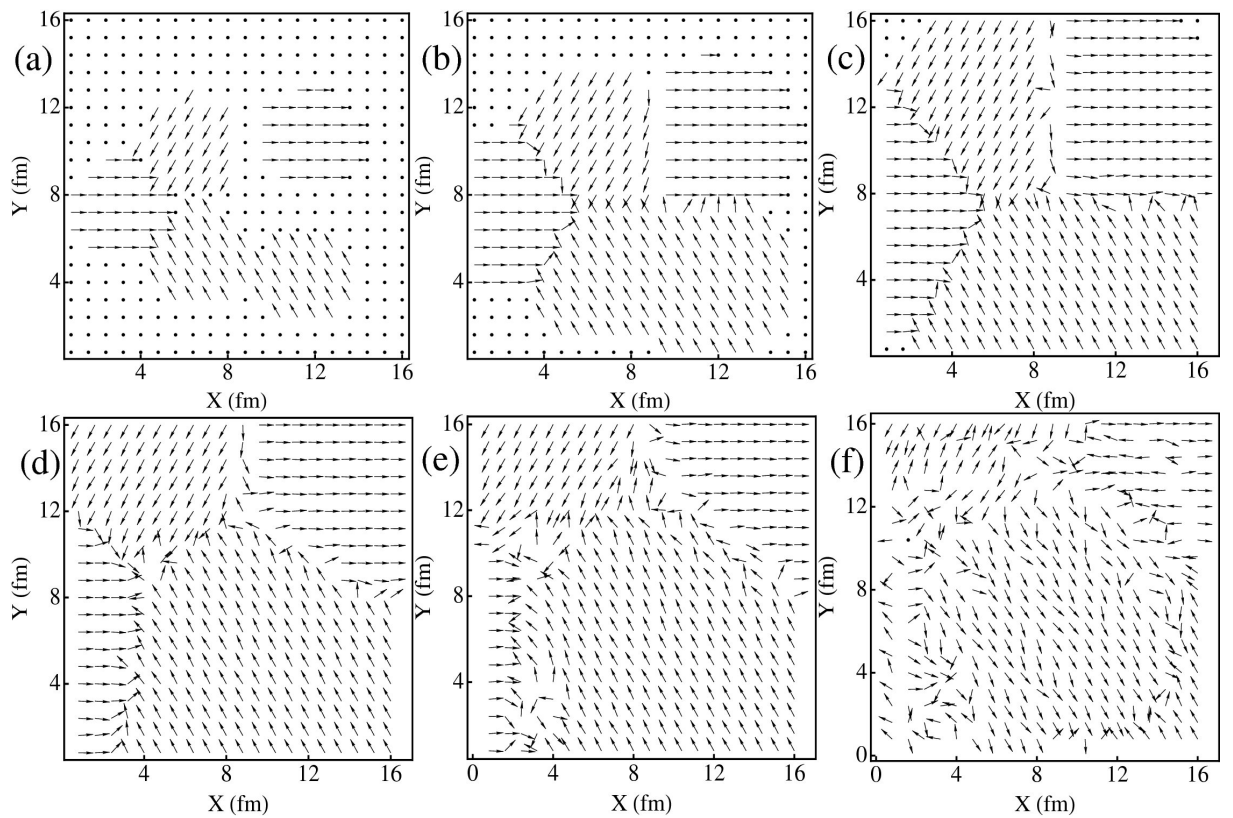


Figure 3.6:

Plots of the phase θ of the order parameter l . (a) shows the initial distribution of θ in the bubbles at $\tau = 0.5$ fm. (b) - (f) show plots of θ at $\tau = 2.0, 4.6, 11.0, 12.2,$ and 13.7 fm respectively. Location of domain walls and the string (with positive winding) and antistring (with negative winding) are clearly seen in the plots in (b)-(e). The motion of the antistring and associated walls can be directly seen from these plots and an estimate of the velocity can be obtained.

domain walls are identified as the boundaries where two different values of θ meet, and strings correspond to the non-trivial winding of θ at the junctions of three walls. From Fig.(3.6b,c) we clearly see that at one of the junctions we have a string (at $X \simeq 5$ fm, $Y \simeq 8$ fm) with positive winding and we have an anti-string at $X \simeq 9$ fm, $Y \simeq 8$ fm with negative winding. Note the rapid motion of the walls forming the antistring towards positive Y axis from Fig(3.6c) (at $\tau = 4.6$ fm) to Fig.(3.6e) (at $\tau = 12.2$ fm). The average speed of the antistring (and wall associated with that) can be directly estimated from these figures to be about 0.5 (in natural units with $c = 1$). This result is important in view of the discussion in the preceding section showing that effects of pressure differences between different $Z(3)$ vacua, arising from quarks, may be dominated by such random velocities present for the walls and strings at the time of formation. The motion of the walls here is a direct result of the straightening of the L shaped wall structure due to its surface tension. For the same reason the wall in the left part of Fig.(3.6b) also straightens from the initial wedge shape. Fig.(3.6f) shows almost random variations of θ at $\tau = 13.7$ fm when the temperature is 167 MeV, well below the critical temperature. Though it is interesting to note that a large region of roughly uniform values of θ still survives at this stage.

Fig.(3.7) shows surface plots of the local energy density ε . ε is plotted in units of GeV/fm^3 . Although the simulation is 2+1 dimensional representing the transverse plane of the QGP system, we calculate energy in 3+1 dimensions by taking a thickness of 1 fm in the central rapidity region. Fig.(3.7a) shows plot at $\tau = 3$ fm when bubbles have coalesced. In Fig.(3.7b) at $\tau = 3.6$ fm we see that bubble walls have almost decayed (in ripples of l waves) between the bubbles with same θ (i.e. same $Z(3)$ vacua) as can be checked from θ plots in Fig.(3.6). Energy density remains well localized in the regions where domain walls exist. Also, one can see the small peaks in the energy density where strings and antistrings exist. Large peaks arise from oscillations of l when bubble walls coalesce, as discussed in [66]. Large values of ε near the boundary of the lattice are due to relativistically expanding bubble walls. Motion of walls and generation of increased fluctuations in energy density are seen in Fig.(3.7c-3.7e). Fig.(3.7f) at $\tau = 13.2$ fm (with $T = 169$ MeV) shows that walls have decayed. However, some extended regions of high energy density can be seen at this stage also.

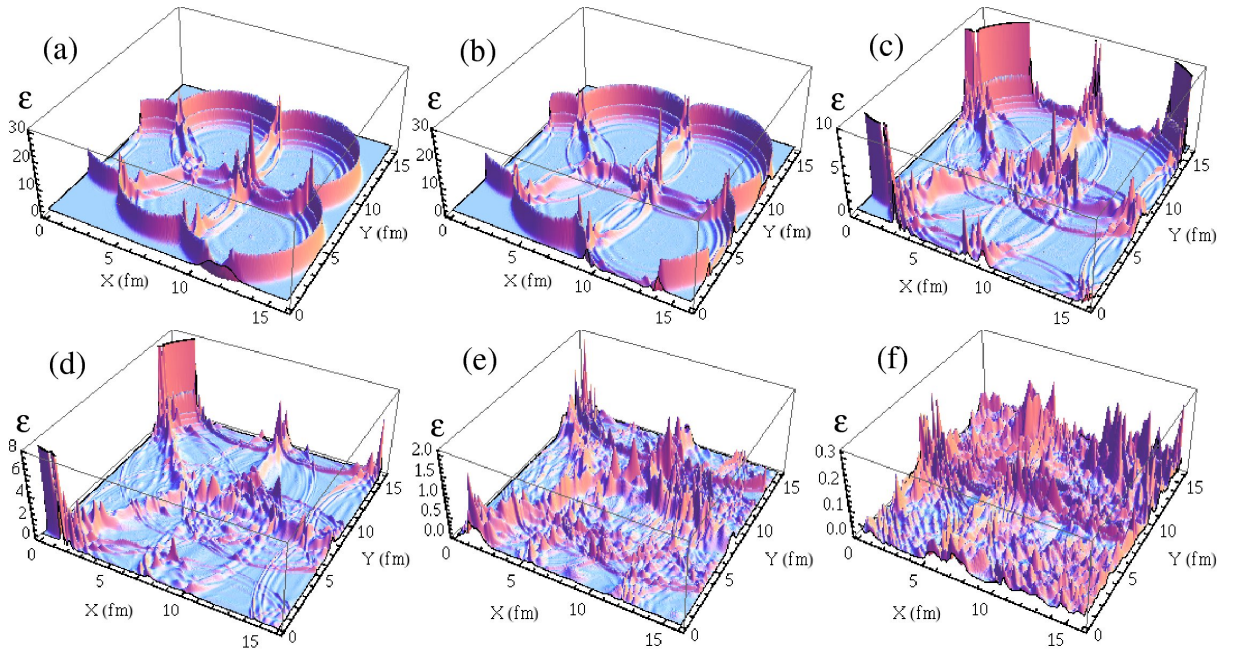


Figure 3.7:

Surface plots of the local energy density ε corresponding to the Lagrangian density in Eq.(3.2) in GeV/fm^3 . (a) - (f) show plots at $\tau = 3.0, 3.6, 5.0, 6.0, 8.0,$ and 13.2 fm respectively. Extended domain walls can be seen from these plots of ε in (b) - (e). Small peaks in ε exist at the locations of string and antistring (larger peaks arise from oscillations of field where bubbles coalesce). Plot in (f) is at the stage when $T = 169$ MeV and domain walls have decayed away.

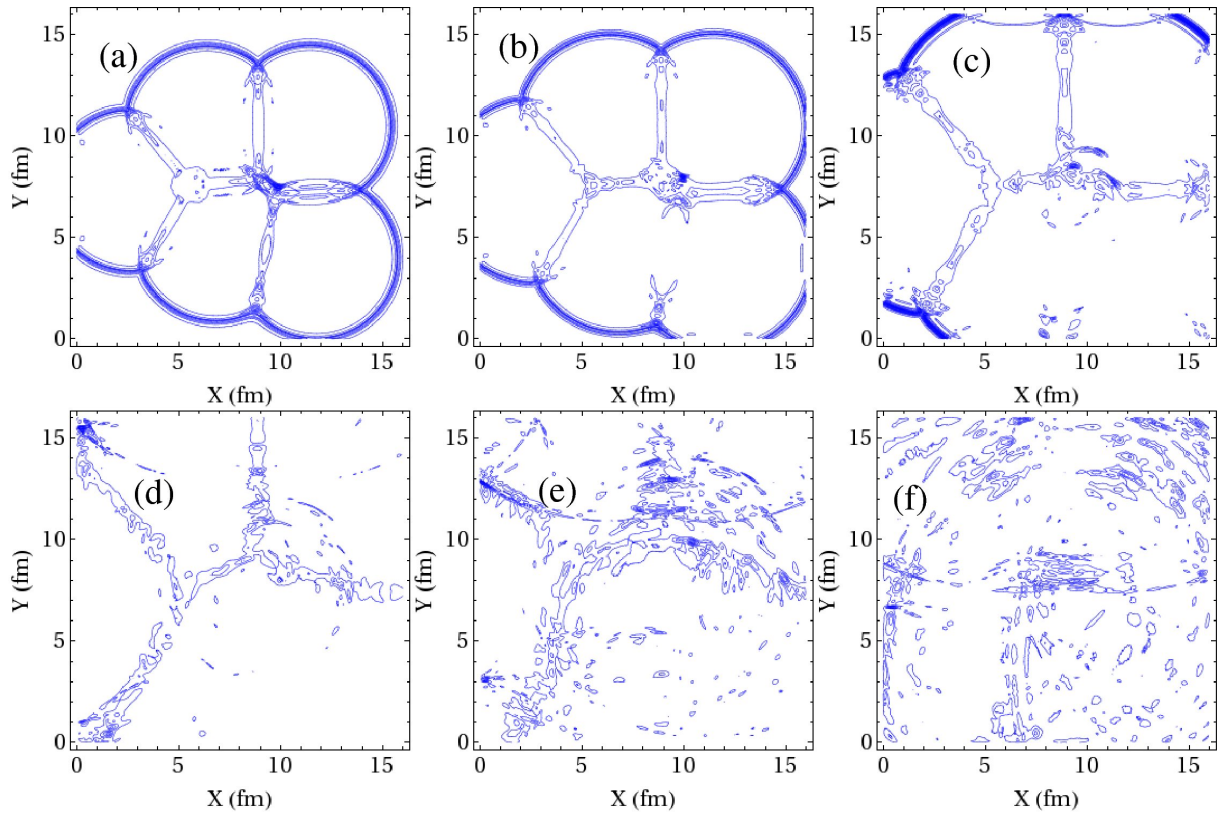


Figure 3.8:

Contour plots of the local energy density ε at different stages. Plots in (a) - (f) correspond to $\tau = 3.0, 3.6, 5.0, 7.6, 10.2,$ and 13.2 fm respectively. Structure of domains walls formed near the coalescence region of bubbles with different θ is clear in (b), whereas the bubble walls at lower half of Y region, and near $X = 10$ fm, are seen to simply decay away due to same vacuum in the colliding bubbles. Motion of the antistring and associated domain walls is clear from plots in (b) - (e). The last plot in (f) is at $\tau = 13.2$ fm when $T = 169$ MeV.

Fig.(3.8) shows contour plots of energy density ε . Fig.(3.8a) shows coalescence of bubbles at $\tau = 3$ fm. Fig.(3.8b) at $\tau = 3.6$ fm clearly shows the difference in the wall coalescence depending on the vacua in the colliding bubbles. Where domain walls exist, we see extended regions of high energy density contours whereas where the two vacua in colliding bubbles are same, there are essentially no high energy density contours. Motion of domain walls and strings at wall junctions is clearly seen in these contour plots in Fig.(3.8b-3.8d). Fig.(3.8e) is at $\tau = 10.2$ fm when T drops to T_c . Wall structures are still present. Fig.(3.8f) is at $\tau = 13.2$ fm ($T = 169$ MeV) when walls have decayed away, though some extended structures in contours still survive.

We have also calculated the standard deviation of energy density σ at each time stage to study how energy fluctuations change during the evolution. In Fig.(3.9) we show the plot of σ/ε as a function of proper time. Here ε is the average value of energy density at that time stage. The energy density ε decreases due to longitudinal expansion, hence we plot this ratio to get an idea of relative importance of energy density fluctuations. Fig.(3.9) shows initial rapid drop in σ/ε due to large increase in ε during the heating stage upto $\tau = 1$ fm, followed by a rise due to increased energy density fluctuations during the stage when bubbles coalesce and bubble walls decay, as expected. Interesting thing to note is a slight peak in the plot near $\tau = 10.5$ fm when T drops below T_c . This should correspond to the decay of domain walls and may provide a signal for the formation and subsequent decay of such objects in RHICE.

3.7.2 Formation and collapse of a closed wall

Fig.(3.10-3.14) show the results of simulation where nine bubbles are nucleated. Fig.(3.10) shows a time sequence of surface plots of $l(x)$ (similar to Fig.(3.5)). Fig.(3.10a) shows the initial profiles of the QGP bubbles at $\tau = 0.5$ fm with the nucleation temperature of $T = 200$ MeV. Fig.(3.10b) shows the profile of l for the bubbles at $\tau = 1.5$ fm showing the expansion of the bubbles. Fig.(3.10c-3.10i) show plots of $l_0 - l$ at different stages. There is formation of a closed domain wall near the central region which is clearly first seen in Fig.(3.10e) at $\tau = 5$ fm. The collapse of this closed domain wall is seen in the subsequent plots with the closed wall completely collapsing away in Fig.(3.10h) at $\tau = 9.6$ fm. Only surviving structure is an extended domain

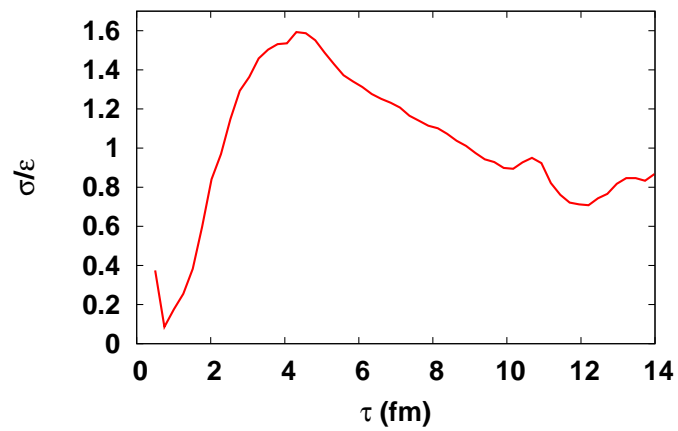


Figure 3.9:

Plot of the ratio of standard deviation of energy density σ and the average energy density ε as a function of proper time. Energy fluctuations increase during the initial stages when bubbles coalesce and bubble walls decay. After that there is a slow decrease in energy fluctuation until the stage when the temperature drops below T_c and $\tau \simeq 10.5$ fm. Energy fluctuations increase after this stage. Note small peak near the transition stage.

wall along the X axis. Fig.(3.10i) is at $\tau = 13.2$ fm when $T = 169$ MeV. The domain walls have decayed away and l fluctuates about the value zero as appropriate for the confined phase.

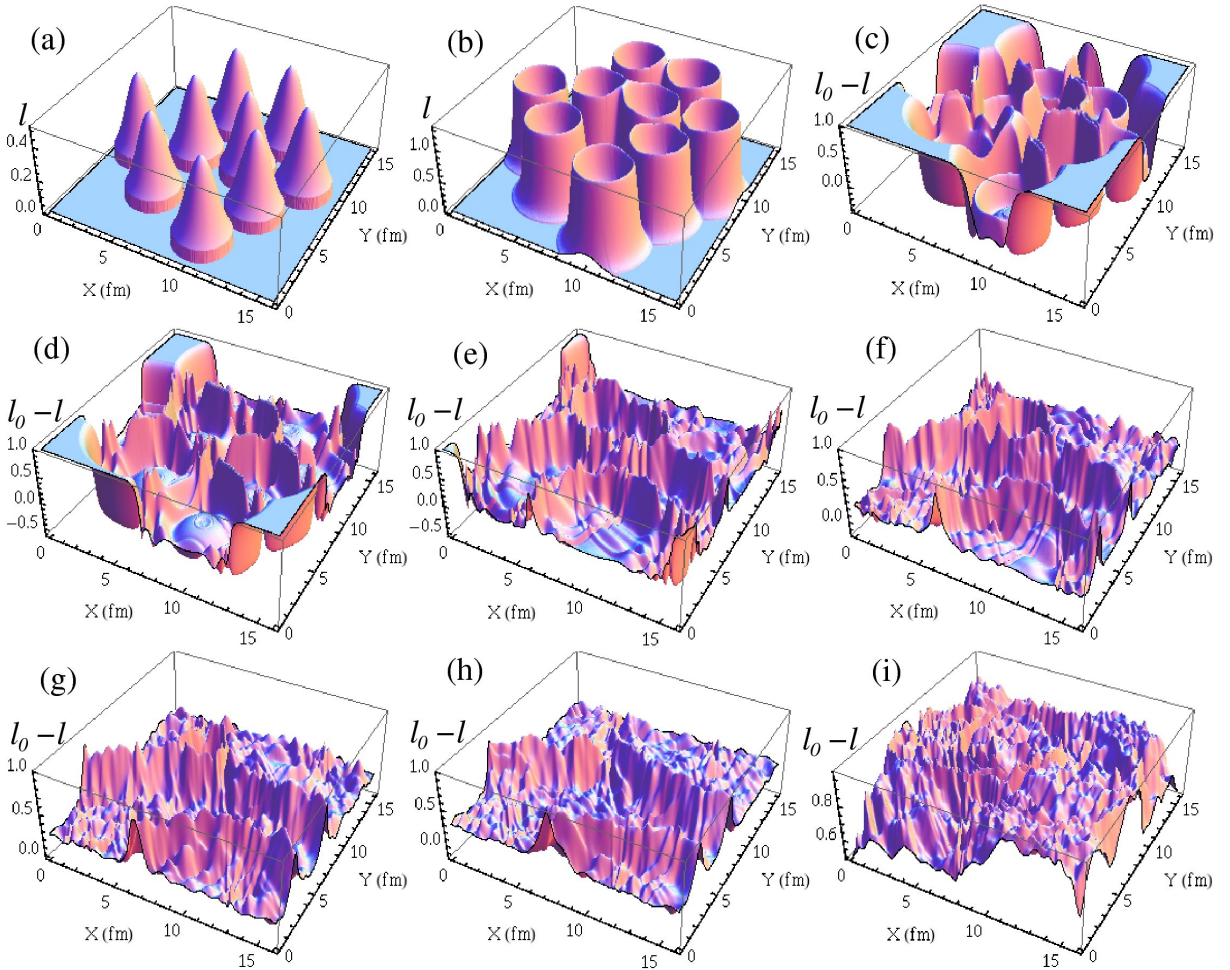


Figure 3.10:

(a) and (b) show plots of profiles of l at $\tau = 0.5$ fm and 1.5 fm respectively for the case when 9 bubbles are nucleated. (c)-(i) show plots of $l_0 - l$ at $\tau = 2.0, 3.0, 5.0, 7.0, 8.6, 9.6,$ and 13.2 fm respectively. Formation of a closed domain wall is first clearly seen in the plot in (e). This closed domain wall collapses as seen in plots in (e) through (h). Only surviving domain wall is an extended wall along X axis in (h). Plot in (i) is when the temperature $T = 169$ MeV.

Fig.(3.11) shows plots of the phase θ of l at different stages. Initial phase distribution in different bubbles is shown in Fig.(3.11a) at $\tau = 0.5$ fm. Fig.(3.11b) shows the formation of closed, elliptical shaped domain wall at $\tau = 2.6$ fm.

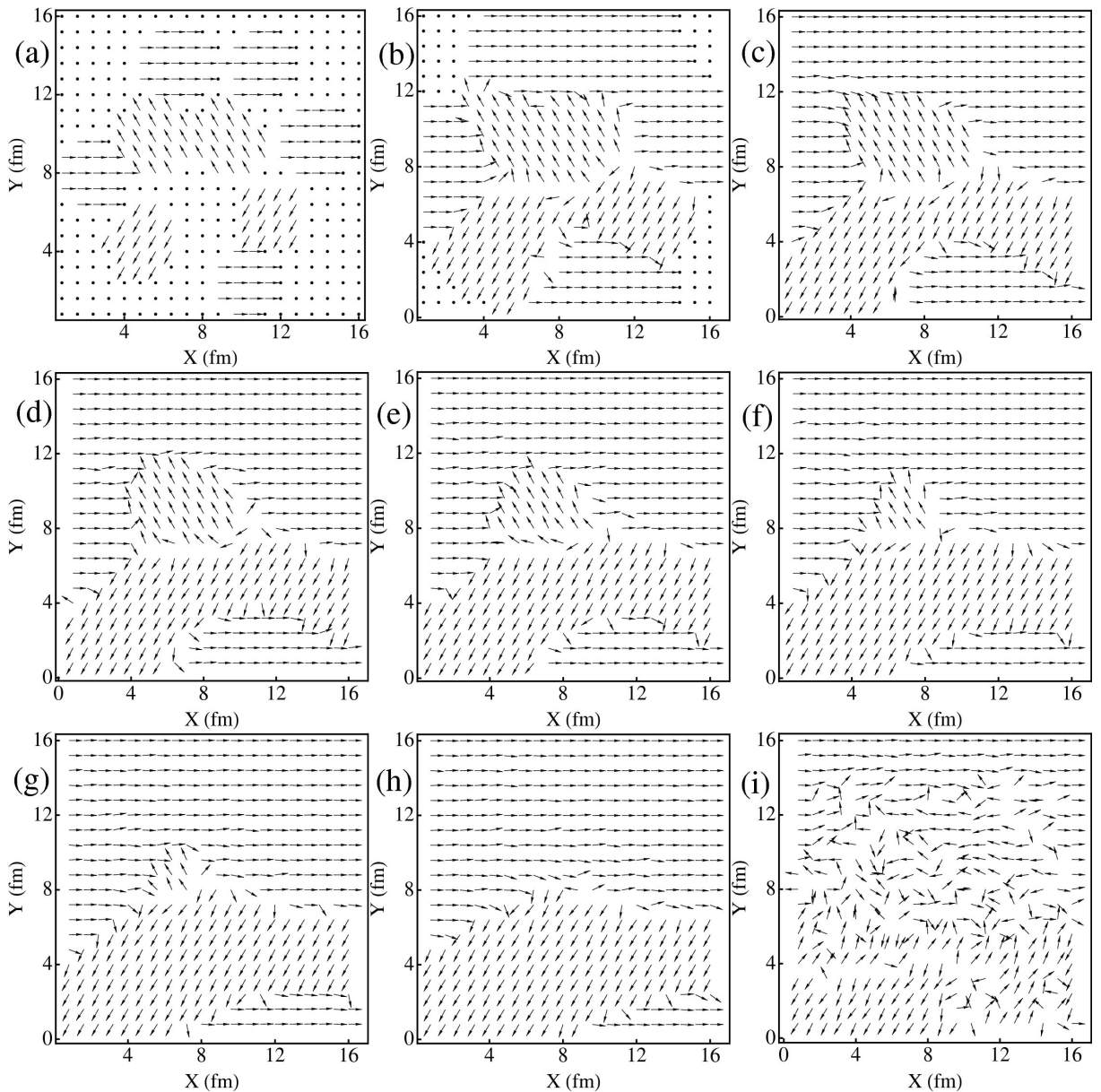


Figure 3.11:

Plots of the phase θ of l . (a) shows initial distribution of θ in the bubbles at $\tau = 0.5$ fm. (b) - (i) show plots of θ at $\tau = 2.6, 5.0, 6.0, 7.0, 8.0, 8.6, 9.6,$ and 13.8 fm respectively. (b) shows formation of elliptical shaped closed domain wall which subsequently becomes more circular as it collapses away by $\tau = 9.6$ fm as shown by the plot in (h). The plot in (i) is at $T = 167$ MeV showing random fluctuations of θ .

Strings and antistrings can also be identified by checking the windings of θ . The closed domain wall collapses, and in the process becomes more circular, as shown in the plots in Fig.(3.11b-3.11h). Fig.(3.11h) shows the plot at $\tau = 9.6$ fm when the closed domain wall completely collapses away, leaving only an extended domain wall running along X axis between $Y \simeq 4 - 8$ fm. The final Fig.(3.11i) at $\tau = 13.8$ fm is when the temperature $T = 167$ MeV showing random fluctuations of θ when domain walls have decayed away in the confining phase.

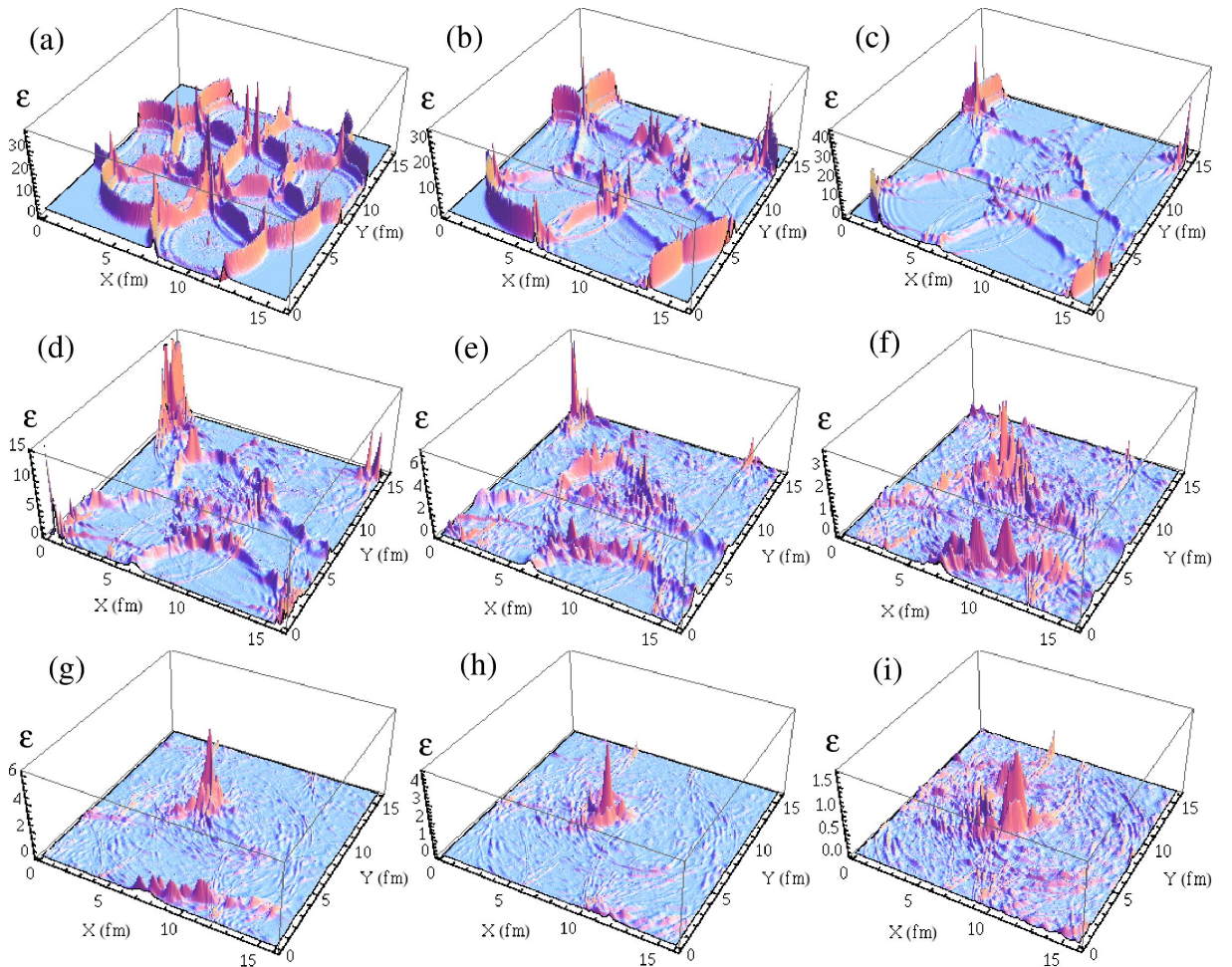


Figure 3.12:

Surface plots of the local energy density ε in GeV/fm^3 . (a) - (i) show plots at $\tau = 2.6, 3.5, 4.6, 5.6, 7.0, 8.6, 9.6, 11.2,$ and 13.2 fm respectively. Formation and subsequent collapse of closed domain wall is clearly seen in plots in (c) through (g). Note that the strong peak in ε resulting from domain wall collapse (the *hot spot*) survives in (i) when $T = 169$ MeV.

Fig.(3.12) shows the surface plot of energy density ε at different stages. Extended thin regions of large values of ε are clearly seen in the plots corresponding to domain walls. Collapse of the closed domain wall is also clearly seen in Fig.(3.12c-3.12g). Important thing to note here is the surviving peak in the energy density plot at the location of domain wall collapse. This peak survives even at the stage shown in Fig.(3.12i) at $\tau = 13.2$ fm when $T = 169$ MeV, well below the transition temperature. Such *hot spots* may be the clearest signals of formation and collapse of Z(3) walls.

Contour plots of ε are shown in Fig.(3.13). Though closed domain wall can be seen already in Fig.(3.13b) (at $\tau = 3.5$ fm), the domain wall is still attached to outward expanding bubble walls near $X = 3$ fm, $Y = 12$ fm which affects the evolution/motion of that portion of the domain wall. Formation of distinct closed wall structure is first visible in Fig.(3.13c) at $\tau = 4.6$ fm. Subsequent plots clearly show how the domain wall becomes circular and finally collapses away by Fig.(3.13k) at $\tau = 9.6$ fm. Note the survival of the *hot spot* even at the stage shown in Fig.(3.13l) at $\tau = 13.2$ fm when $T = 169$ MeV.

One can make a rough estimate of the velocity of the closed wall during its collapse from these plots. In Fig.(3.13c), at $\tau = 4.6$ fm, the X extent of the closed wall is about 8 fm and the Y extent is about 5 fm. The wall collapses away by the stage in Fig.(3.13k) at $\tau = 9.6$ fm. This gives rough velocity of collapse in X direction to be about 0.8 while the velocity in Y direction is about 0.5. Note that here, as well as in Fig.(3.6) for the five bubble case, the estimate of the wall velocity is not affected by the extra dissipation which is introduced only in a very thin strip (consisting of ten lattice points) near the lattice boundary. Formation and collapse of such closed domain walls is important as the resulting hot spot can lead to important experimental signatures. Further, such closed domain wall structures are crucial in the studies of P_T enhancement, especially for heavy flavor hadrons as discussed in [62, 63]

Fig.(3.14) shows the evolution of the ratio of the standard deviation of energy density and the average energy density. As for the five bubble case, initial drop and rise are due to heating stage upto $\tau = 1$ fm and subsequent bubble coalescence and decay of bubble walls. In this case the ratio remain roughly constant upto $\tau \simeq 10.5$ fm which is the transition stage to the confining phase. This is the stage when the surviving extended domain wall starts decaying. This is also the stage soon after the

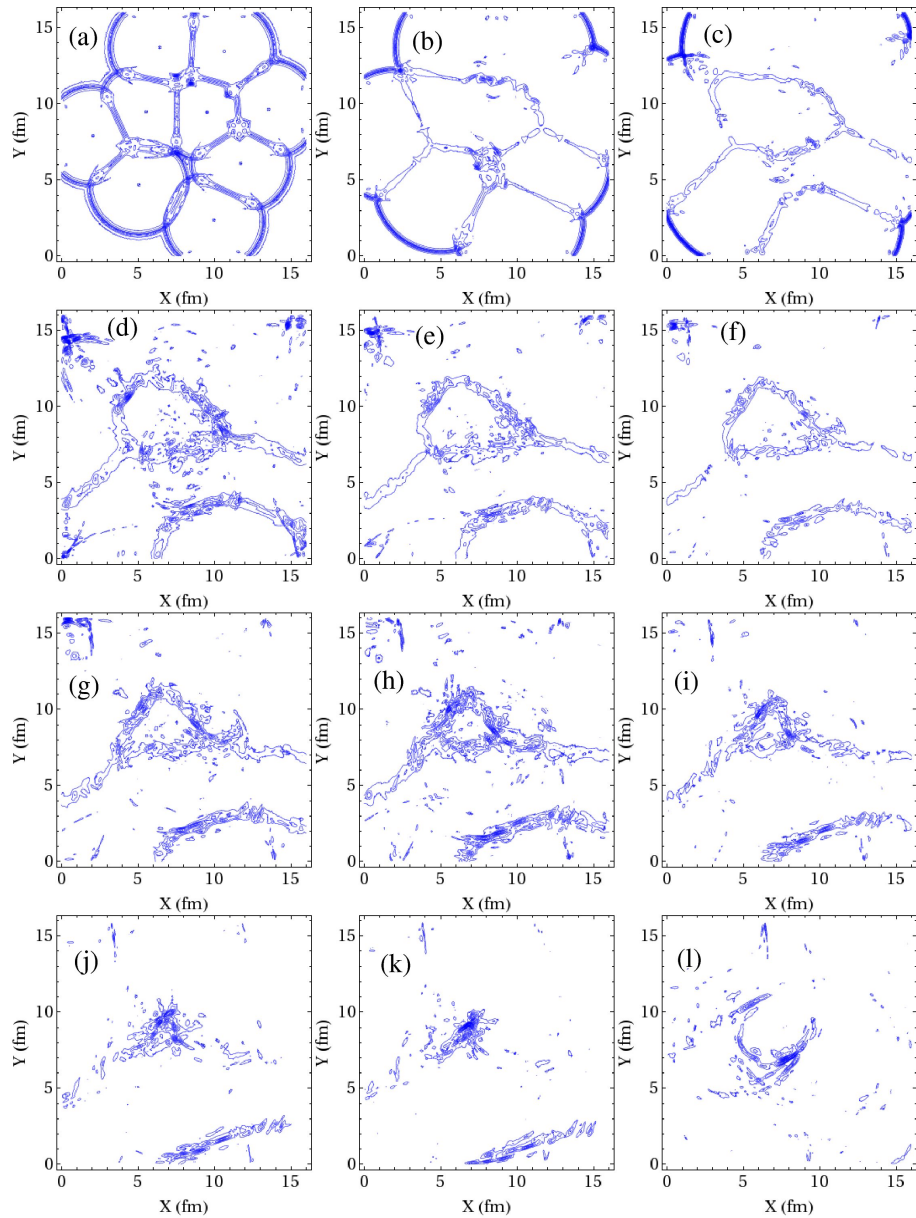


Figure 3.13:

Contour plots of the local energy density ε at different stages. Plots in (a) - (l) correspond to $\tau = 2.6, 3.5, 4.6, 6.0, 6.6, 7.0, 7.6, 8.0, 8.6, 9.0, 9.6,$ and 13.2 fm respectively. Formation of distinct closed wall structure is first visible in (c) at $\tau = 4.6$ fm. Subsequent plots show the collapse of this domain wall as it becomes more circular. The wall finally collapses away in (k) at $\tau = 9.6$ fm. Note that concentration of energy density at the location of domain wall collapse (the *hot spot*) survives even at the stage shown in (l) at $\tau = 13.2$ fm when $T = 169$ MeV.

closed domain wall collapses away. The prominent peak at this stage should be a combined result of both of these effects. The large increase in the variance of energy density at this stage should be detectable from the analysis of particle distributions and should be a clear signal of hot spots resulting from collapse of closed walls and the decay of any surviving domain walls.

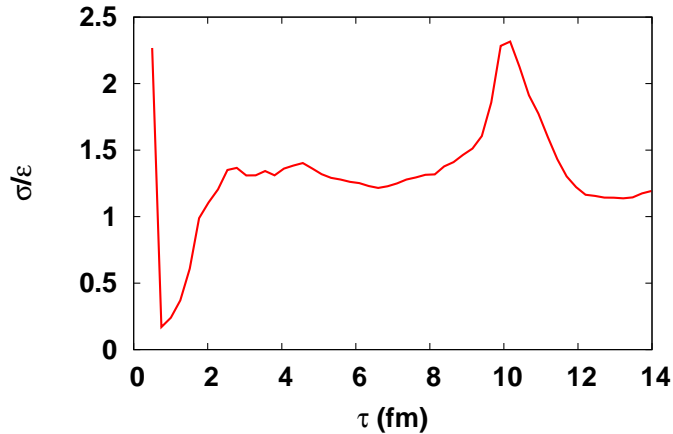


Figure 3.14:

Plot of the ratio of standard deviation of energy density σ and the average energy density ε as a function of proper time. Energy fluctuations increase during the initial stages when bubbles coalesce and bubble walls decay. After that σ/ε remains roughly constant until the stage when the temperature drops below T_c at $\tau \simeq 10.5$ fm. This is also the stage just after the collapse of the closed domain wall. Energy fluctuations sharply increase around this stage. Note the prominent peak at this stage.

3.8 Possible experimental signatures of $Z(3)$ walls and strings

The $Z(3)$ wall network and associated strings form during the early confinement-deconfinement phase transition. They undergo evolution in an expanding plasma with decreasing temperature, and eventually melt away when the temperature drops below the deconfinement-confinement phase transition temperature. They may leave their signatures in the distribution of final particles due to large concentration of

energy density in extended regions as well as due to non-trivial scatterings of quarks and antiquarks with these objects.

Let's focus on the extended regions of high energy density resulting from the domain walls and strings. This is obvious from our simulations that some extended structures/hot spots also survive after the temperature drops below the transition temperature T_c . Note that even the hot spot resulting from the collapse of closed domain wall in Fig.(3.11),(3.12) will be stretched in the longitudinal direction into an extended linear structure resulting from the collapse of a cylindrical wall. Since the final freezeout temperature is not too far below the transition temperature, the energy density concentrated in any extended sheet like for domain walls and line like for strings /hot spots regions may not be able to defuse away effectively. Assuming local energy density to directly result in multiplicity of particles coming from that region, an analysis of particle distribution in P_T and in rapidity should be able to reflect any such extended regions. In this context, it will be interesting to investigate if the ridge phenomenon seen at RHIC [72] could be a manifestation of an underlying Z(3) domain wall/string structure. Correlation of particle production over large range of rapidity will naturally result from longitudinally extended regions of high energy density (*hot spots* in the transverse plane). Combined with flow effects it may lead to ridge like structures [72, 73]. If extended domain wall structure survives in the transverse plane also, this will then extend to sheet like regions in the longitudinal direction. Decay of such a region of high energy density may directly lead to a ridge like structure, without requiring flow effects.

We expect non-trivial signatures resulting from the consideration of interactions of quarks and antiquarks with domain walls. It was shown in an earlier work [63] using generic arguments that quarks and antiquarks should have non-zero reflection coefficients when traversing across these domain walls. A collapsing domain wall will then concentrate any excess baryon number enclosed, leading to formation of baryon rich regions. This is just like Witten's scenario for the early universe [74] (which was applied for the case of RHICE in ref. [75]). However, for these works it was crucial that the quark-hadron transition be of (strong) first order. Even though we have implemented it in the context of a first order transition via bubble nucleation, these objects will form even if the transition is a cross-over. Thus, concentration of baryons

in small regions should be expected to occur in RHICE which should manifest in baryon concentration in small regions of rapidity and P_T .

Another important aspect of quark/antiquark reflection is that inside a collapsing wall, each reflection increases the momentum of the enclosed particle. When closed domain walls collapse then enclosed quarks/antiquarks may undergo multiple reflections before finally getting out. This leads to a specific pattern of P_T enhancement of quarks with heavy flavors showing more prominent effects [62]. The modification of P_T spectrum of resulting hadrons can be calculated, and the enhancement of heavy flavor hadrons at high P_T can be analyzed for the signal for the formation of Z(3) domain walls in these experiments [62]. In our simulations extended domain walls also form which show bulk motion with velocities of order 0.5. Quarks/antiquarks reflected from such moving extended walls will lead to anisotropic momentum distribution of emitted particles which may also provide signature of such walls. For collapsing closed domain walls, spherical domain walls were used for estimates in ref. [63] and in ref. [62]. Our simulation in the present work provides a more realistic distribution of shapes and sizes for the resulting domain wall network. We have estimated the velocity of moving domain walls to range from 0.5 to 0.8 for the situations studied. These velocities are large enough to have important effect on the momentum of quarks/antiquarks undergoing reflection from these walls. One needs to combine the analysis of [62, 63] with the present simulation to get a concrete signature for baryon concentration and heavy flavor hadron P_T spectrum modification.

The results show interesting pattern of the evolution of the fluctuations in the energy density. As seen in Fig.(3.9) and Fig.(3.14), energy density fluctuations show rapid changes during stages of bubble wall coalescence and during collapse/decay of domain walls. Even string-antistring annihilations should be contributing to these fluctuations. Fluctuations near the transition stage may leave direct imprints on particle distributions. It is intriguing to think whether dileptons or direct photons may be sensitive to these fluctuations, which could then give a time history of evolution of such energy density fluctuations during the early stages as well. Even the presence of domain walls and strings during early stages may affect quark-antiquark distributions in those regions which may leave imprints on dileptons/direct photons. An important

point to note is that in our model, we expect energy density fluctuations in event averages (representing high energy density regions of domain walls/strings as discussed above), as well as event-by-event fluctuations. These will result due to fluctuation in the number/geometry of domain walls/strings from one event to the other resulting from different distribution of (randomly occurring) $Z(3)$ vacua in the QGP bubbles. Even the number of QGP bubbles, governed by the nucleation probability, will vary from one event to the other contributing to these event-by-event fluctuations.

Here we discussed confinement-deconfinement transition as an equilibrium first order phase transition. However, elliptic flow results hint towards very early thermalisation. In this short time period, it may not be correct to consider this transition as an equilibrium first order phase transition. Rather, the more appropriate situation is the quenched transition. We will discuss the quenched dynamics and formation and evolution of $Z(3)$ domains in next chapter. We will also discuss the effect of quarks in terms of explicit symmetry breaking.

Chapter 4

Domain Growth and Fluctuations during Quenched Transition to QGP in Relativistic Heavy-ion Collisions

4.1 Introduction

In relativistic heavy-ion collision experiments (RHICE) the collision of two nuclei leads to a hot dense region which is expected to rapidly achieve state of thermal equilibrium. For the relevant range of energies and colliding nuclei at RHIC and at LHC there is compelling evidence that a region of quark-gluon plasma is created in these collisions. Simulation results as well as experimental data, such as elliptic flow measurements, all point towards a very rapid thermalization to the QGP phase, within a proper time less than 1 fm. We thus have a system which starts out in the confining phase, and within proper time of (probably much less than) 1 fm makes a transition to the QGP phase (with maximum temperature estimates ranging from 200 MeV to more than 700 MeV for the relevant energies in these experiments). Lattice results show that for real world QCD with small baryon density (as appropriate for the central rapidity regions in RHICE) the transition is likely to be a crossover. With that, the dynamics of the transition depends crucially on the rate of temperature change compared to the time

scale of the evolution of the order parameter field. For an equilibrium transition, we had studied the formation of $Z(3)$ domains and associated *QGP strings* using a first order transition dynamics via bubble nucleation in the 3rd chapter of this thesis [41]. These studies are appropriate for large chemical potential case, as in lower energy collisions, where the transition is expected to be of first order. Though, the results for $Z(3)$ wall network etc. having certain universal characters, may be applicable in more general context, even for a cross-over, as explained in [41, 76].

However, given the very short time scale of initial thermalization to QGP state, an equilibrium dynamics of the transition appears unlikely. A more appropriate description of the transition should employ quenched dynamics in which the growth of $Z(3)$ domains will be via spinodal decomposition. In this work, we carry out such a study [42] using the Polyakov loop, $l(x)$, as an order parameter for the confinement-deconfinement transition, with an effective potential of the kind used in refs. [59, 60, 77]. For our simulation results we choose a definite parameterization of the effective potential [59] as was used in previous chapter [41]. We model the phase transition in this Polyakov loop model, with the initial field configuration (in the confining phase) covering a small neighborhood of the confining vacuum $l \simeq 0$ as appropriate for the initial $T = 0$ system. In a quench, the temperature rapidly (rather suddenly) increases to its maximum value T_0 with the effective potential changed accordingly. The initial field l , unable to relax to the new equilibrium vacuum state in this short time, becomes unstable and rolls down in different directions from the top of the central hill in the effective potential of l . We study the formation of $Z(3)$ domain structure during this evolution. When explicit $Z(3)$ symmetry breaking effects (arising from dynamical quark effects) are small, then we find well defined $Z(3)$ domains which coarsen in time. With a symmetric initial patch of l , all the three $Z(3)$ domains form with random shapes and rapidly increase in size by coarsening. Remarkably, the magnitude plot of l shows vacuum bubble like configurations, such as those which arise in a first order transition, arising during the quench in this case (when the initial field rolls down in different directions). This first order transition like behavior occurs even though there is no metastable vacuum separated by a barrier from the true vacuum for the parameter values used. These bubble like configurations expand as well, somewhat in similar manner as during a first order transition. We

will explore more about this transition dynamics in the next chapter of this thesis.

When the initial patch of l is only partially symmetric around $l = 0$ (as appropriate for small explicit symmetry breaking from quark effects), the dynamics retains these qualitative aspects with expected changes. Thus, true vacuum domains (with $\theta = 0$) are more abundant and they also grow fast at the cost of the other two $Z(3)$ domains (which are now metastable due to explicit symmetry breaking). Still, for small explicit symmetry breaking, all the three types of domains occur during the initial stages of the transition. There are few, small $Z(3)$ walls as there are fewer metastable $Z(3)$ domains embedded in the dominant true vacuum with $\theta = 0$. These walls shrink rapidly and eventually only the true vacuum survives.

The dynamics is found to be very different when the explicit symmetry breaking due to quark effects is taken to be strong. In this case the initial patch of l (around equilibrium point for $T = 0$ effective potential) could be significantly shifted towards the true vacuum for the quenched $T = T_0$ effective potential. In such a situation, l will roll down roughly along the same direction with angular variations becoming smaller during the roll down. In this case only $\theta = 0$ vacuum survives and no other $Z(3)$ domains are formed. Also, in this case we do not find bubble-like configurations. However, in this case we find huge oscillations of l with large length scales. This behavior is known from previous studies of the dynamics of scalar field in a quench [78] and is expected here when angular variations are small. The dynamics of field in such a case is dominated by large length scale coherent oscillations. It leads to novel scenarios of reheating via parametric resonance in the case of inflation in the early Universe [78]. In our case of RHICE also it raises important questions about the possibility of parametric resonance and of novel modes of particle production from these large oscillations of l during the early stages of the transition. In this chapter, we explore another important effect of these large oscillations, on the evolution of flow anisotropies in RHICE. As most of the flow anisotropies are expected to develop during first few fm of the QGP formation, it becomes an important question if the presence of large oscillations of l can affect the development of these flow anisotropies. As we will see, this indeed happens and these large oscillations lead to large fluctuations in flow anisotropy.

We mention here that we do not discuss which of the cases discussed here (small,

or large explicit symmetry breaking) may actually be realized in RHICE. This is primarily because of lack of understanding of the magnitude of explicit symmetry breaking term near $T = T_c$. Also, the spread of initial field configuration about confining vacuum plays a crucial role here and that in turn depends on details of pre-equilibration stage. A proper modeling of this stage and resulting estimate of the initial spread is essential before one can make more definitive statements about the dynamics of the transition. However, our main purpose here is to illustrate the possibility of very different types of dynamics of transition depending on the initial configuration. Our results show that in quenched dynamics, $Z(3)$ domains, and resulting $Z(3)$ domain walls, can last for any reasonably length of time only when explicit symmetry breaking terms are very small. Otherwise either different domains do not form at all, hence no $Z(3)$ walls are formed, or fewer metastable $Z(3)$ domains form embedded in most abundant true vacuum region. In the latter case resulting $Z(3)$ walls are smaller to begin with, and disappear quickly.

The consequences of the presence of $Z(3)$ walls and strings for cosmology as well as for RHICE [41, 62, 63, 76], including the possibility of CP violating scattering of quarks from $Z(3)$ walls leading to interesting observational implications [79], have been discussed. Recently an interesting possibility has been discussed by Asakawa et al. in ref. [80] where it is argued that scattering of partons from $Z(3)$ walls may account for small viscosity as well as large opacity of QGP. Our results for the formation of $Z(3)$ domains during quench (which are abundant only for small explicit symmetry breaking case) can be relevant for the studies in ref. [80]. In this context we mention that smallest reasonable size $Z(3)$ domains (hence $Z(3)$ walls) we find are of order 1-2 fm at very early times, and at that stage the magnitude of the Polyakov loop order parameter l is very small, of order few percent of its vacuum expectation value. The quark scattering from $Z(3)$ walls is likely to be small for such a small magnitude of l [62, 63, 79]. By the time the magnitude of l becomes significant, domains coarsen to have large sizes, of order several fm. Thus, in the context of our model it appears difficult to form very small $Z(3)$ domains which still can scatter partons effectively (as needed in the study of ref. [80]).

It is important to note that our results for domain growth and fluctuations for the quench case are dominated by the spinodal instabilities during the roll down of

the field from the top of the hill of the effective potential. These instabilities arise primarily from the nature of the quench when the initial field configuration becomes unstable to exponential growth of long wavelength modes due to sudden change in the shape of the effective potential (the quench), and will be in general present even if the transition is a cross-over. In this sense we believe that the qualitative aspects of our results have a wider applicability and are not crucially dependent on the specific form of the effective potential used here.

Here, we also note that recent work of Deka et al. [81] has provided a support for the existence of these metastable vacua from Lattice at temperatures greater than 750 MeV. Even though this value of temperature is much higher than the temperature reachable at RHIC and LHC, the mere existence of these structures in Lattice calculations is important in view of arguments in the literature claiming that these objects are unphysical [56]. We also note that a simulation of spinodal decomposition in Polyakov loop model has been carried out in ref. [82], where fluctuations in the Polyakov loop and growth of long wavelength modes (representing domain formation) are investigated. In comparison, the main focus of our work is on detailed growth of domains due to coarsening with and without explicit symmetry breaking, new bubble like structures, and existence of large fluctuations affecting flow anisotropies in important ways.

4.2 Effective Potential Based on Polyakov Loop

We have discussed the salient features of the model in section 2 of chapter 3 of this thesis. So we will not repeat it here. The effective Lagrangian density and effective potential are given by Eq.(3.2) and Eq.(3.3) respectively.

The effects of dynamical quarks is included in terms of explicit breaking of the $Z(3)$ symmetry which is represented in the effective potential by inclusion of a linear term in l [59–61]. The potential of Eq.(4.2) with the linear term becomes,

$$V(l) = \left(-\frac{b_1}{2}(l + l^*) - \frac{b_2}{2}|l|^2 - \frac{b_3}{6}(l^3 + l^{*3}) + \frac{1}{4}(|l|^2)^2 \right) b_4 T^4 \quad (4.1)$$

Here coefficient b_1 measures the strength of explicit symmetry breaking. The coefficients b_1 , b_2 , b_3 and b_4 are dimensionless quantities. With $b_1 = 0$, other parameters

b_2 , b_3 and b_4 are fitted in ref. [59, 60] such that that the effective potential reproduces the thermodynamics of pure $SU(3)$ gauge theory on lattice [61, 64, 65]. Due to nonzero b_1 , $l = 0$ vacuum shifts to nonzero l value along $\theta = 0$ direction as shown in the Fig.(4.1)

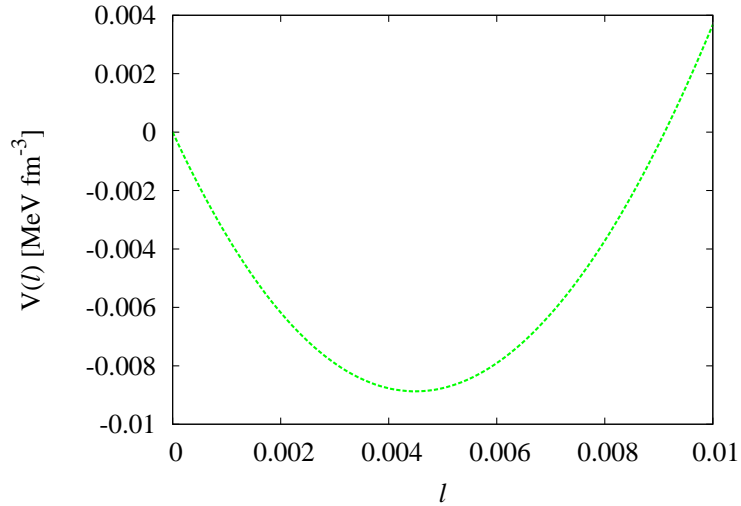


Figure 4.1:
Plot of $V(l)$ in $\theta = 0$ direction shows the shift of vacuum

4.3 Numerical Simulation

In this chapter, we carry out a $2 + 1$ dimensional field theoretic simulation of the dynamics of confinement-deconfinement transition in a quench. First we work within the framework of Bjorken's boost invariant longitudinal expansion model [31] (without any transverse expansion) for the central rapidity region in RHICE. To model the quench, we take the initial field configuration to constitute a small patch around $l = 0$ which corresponds to the vacuum configuration for the confining phase. This is for the case of zero explicit symmetry breaking. We will discuss the case of explicit symmetry breaking later. We have taken the initial phase of l to vary randomly between 0 and 2π from one lattice site to the other, while the magnitude of l is taken to vary uniformly between 0 and ϵ . (We have also taken the initial magnitude to have a fixed value equal to ϵ and the results are similar.) Value of ϵ is taken to be much

smaller than the vacuum expectation value (vev) of l at $T = T_0$ and results remain qualitatively the same for similar small values of ϵ . We report results for $\epsilon = 0.01$ times the vev of l . We take the quench temperature $T_0 = 400$ MeV.

This initial field configuration, which represents the equilibrium field configuration of a system with $T < T_c$, is evolved using the effective potential with $T = T_0 > T_c$. This represents the transition dynamics of a quench. The field configuration is evolved by time dependent equation of motion in the Minkowski space [31]

$$\frac{\partial^2 l_j}{\partial \tau^2} + \frac{1}{\tau} \frac{\partial l_j}{\partial \tau} - \frac{\partial^2 l_j}{\partial x^2} - \frac{\partial^2 l_j}{\partial y^2} = -\frac{g^2}{2NT^2} \frac{\partial V(l)}{\partial l_j}; \quad j = 1, 2 \quad (4.2)$$

with $\frac{\partial l_j}{\partial \tau} = 0$ at $\tau = 0$ and $l = l_1 + il_2$. The temperature is taken to decrease starting with the value T_0 (at an initial time τ_0 which we take to be 1 fm in all the simulations) as $\tau^{-1/3}$ as appropriate for the longitudinal expansion model. We mention that later in Sect.V we will consider an isotropic geometry for the transverse dynamics of QGP as relevant for RHICE. There we will also model non-zero transverse expansion and then the central temperature will decrease faster than $\tau^{-1/3}$. Here, we take a 2000×2000 square lattice with physical size 20 fm x 20 fm. We take this lattice as representing the transverse plane of the QGP formed in a central collision and consider mid rapidity region. The evolution of field was numerically implemented by a stabilized leapfrog algorithm of second order accuracy both in space and in time with the second order derivatives of l_i approximated by a diamond shaped grid [41,76]. We evolve the field using the periodic, fixed, and free boundary conditions for the square lattice. Here we present the results with periodic boundary conditions. We use $\Delta x = 0.01$ fm for the present case, later on we use different values of Δx , as shown by the lattice size in the corresponding figures. we take $\Delta t = \Delta x/\sqrt{2}$ as well as $\Delta t = 0.9\Delta x/\sqrt{2}$ to satisfy the Courant stability criteria. The stability and accuracy of the simulation is checked using the conservation of energy during simulation. The total energy fluctuations remains few percent without any net increase or decrease of total energy in the absence of dissipative \dot{l} term in Eq.(4.4).

First, we present results for the formation and evolution of $Z(3)$ domains. The initial field configuration in the neighborhood of $l = 0$ becomes unstable when evolved with the effective potential (Eq.(4.3)) with $T = T_0 = 400$ MeV (at $\tau = \tau_0 = 1$ fm). As l rolls down in different direction, settling in one of the three $Z(3)$ vacua, different

$Z(3)$ domains form. Initially, as the phase of l is taken to vary randomly from one lattice site to the next, there are no well defined domains. Also, the magnitude of l is very small initially making any association of $Z(3)$ structure meaningless at such early stages. Situation remains similar for very early times as seen in Fig.(4.2a) at an early stage $\tau = 1.2$ fm (i.e. 0.2 fm after the quench). In Fig.(4.2) we have shown the values of the phase of l around the three $Z(3)$ vacua in terms of different shades (colors) to focus on the evolution of $Z(3)$ domain structure. Thus all the values of the phase θ of l are separated in three ranges, between $-2\pi/6$ to $2\pi/6$ ($\theta = 0$ vacuum), between $2\pi/6$ to π ($\theta = 2\pi/3$ vacuum), and between π to $2\pi - 2\pi/6$ ($\theta = 4\pi/3$ vacuum). As the field magnitude grows, the angular variation of l also becomes less random over small length scales, leading to a sort of $Z(3)$ domain structure. $Z(3)$ domains become more well defined, and grow in size by coarsening as shown in sequence of figures Fig.(4.2b-d). Different shades (colors) in Fig.(4.2) represent the three $Z(3)$ domains. Here red, green and blue color represent $\theta = 0, 2\pi/3$ and $4\pi/3$ vacuum respectively. Fig.(4.2b-d) shows the growth of these domains at $\tau = 2.0, 2.4,$ and 2.8 fm, as l relaxes to the three $Z(3)$ vacua and domains grow in size by coarsening. The magnitude of l is about 0.04, 0.08, 0.2, and 0.4 for Figs.(4.2a,b,c, and d) respectively. Note that domains grow rapidly to size of order 2 fm within a time duration of about 1 fm as shown in Fig.(4.2b). Within another 1 fm time, domain size is about 4 fm as seen in Fig.(4.2d).

The boundaries of different $Z(3)$ domains represent $Z(3)$ walls, and junction of three different $Z(3)$ domains gives rise to the QGP strings. These objects have been discussed in detail [41, 76, 83].

We mention here that smallest reasonable size $Z(3)$ domains (hence $Z(3)$ walls), which we find in our simulation, are of order 1-2 fm at very early times, such as seen in Fig.(4.2b). At this stage, the magnitude of the Polyakov loop order parameter l is still very small, of order few percent of its vacuum expectation value. This is important when one considers the possibility of nontrivial scattering of partons from $Z(3)$ walls [62, 63, 79, 80]. The quark scattering from $Z(3)$ walls is likely to be small for such a small magnitude of l [62, 63, 79]. By the time the magnitude of l becomes significant, domains coarsen to have large sizes, of order several fm, as in Fig.(4.2c,d) where the magnitude of l is about 20% and 40%, respectively, of

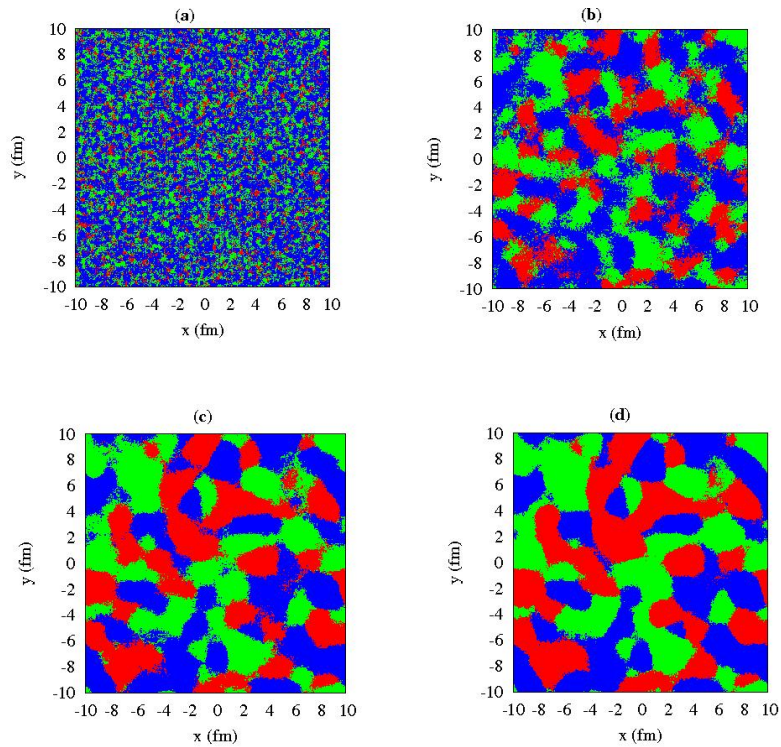


Figure 4.2:

(a) Evolution of $Z(3)$ domain structure during a quench. Note we take the initial temperature to be T_0 ($= 400$ MeV) at proper time $\tau = \tau_0 = 1$ fm to set the initial conditions for the simulation. Here red, green and blue color represent $\theta = 0, 2\pi/3$ and $4\pi/3$ domains respectively. (a) - (d) show the growth of these domains at $\tau = 1.2, 2.0, 2.4,$ and 2.8 fm, (with corresponding values of temperature $T = 376, 317, 298, 283$ MeV) as l relaxes to the three $Z(3)$ vacua and domains grow in size by coarsening. The magnitude of l is about 0.04, 0.08, 0.2, and 0.4 for (a), (b), (c), and (d) respectively. Note that domains grow rapidly to size of order 2 fm within a time duration of about 1 fm as shown in (b). Within another 1 fm time, domain size is about 4 fm (as seen in (d)).

its vacuum expectation value. Thus, in the context of our model, with quenched dynamics of transition, it appears difficult to form very small $Z(3)$ domains which still can scatter partons effectively (as needed in the study of ref. [80]).

4.4 Bubble like Structures during Quench

Here we show a very unexpected result. Fig.(4.3) shows sequence of plots of the magnitude of l during the quench described in the previous section. We note the appearance of bubble like structures. These structures are also seen to grow in a manner similar to the bubbles for a conventional first order phase transition, as in ref. [41,76]. However, the distribution of the phase of l does not show any specific local variation related to these bubble-like configurations. In a roughly uniform region of the phase these localized bubble-like configurations arise and expand. We show here the plots of l in Fig.(4.3) corresponding to the initial central temperature $T = T_0 = 500$ MeV (at $\tau = \tau_0 = 1$ fm). The plots in Fig.(4.3a,b,c,d) are for $\tau = 2.0, 2.8, 3.0,$ and 3.3 fm respectively, with the corresponding values of the central temperature being $T = 395, 355, 345, 336$ MeV. It is important to note that at such high temperatures there is no metastable confining vacuum at $l = 0$ in the effective potential [76]. (Metastable confining vacuum exists from $T = T_c = 182$ MeV upto $T \simeq 250$ MeV.) There is no tunneling modeled, (or thermal hopping over the barrier) here, nor is expected. One expects a simple roll down of the field representing the dynamics of spinodal decomposition during the quench. We mention that similar bubble-like configurations also arise with $T_0 = 400$ MeV. However, in that case the temperature range goes below $T = 250$ MeV. To make a clear case that these bubble like configuration have nothing to do with a first order transition like situation (even remotely), we have shown plots with $T_0 = 500$ MeV.

This result is very unexpected and points to new interesting possibilities for the phase transition dynamics. This may have important implications for RHICE. More importantly this new possibility of transition dynamics needs to be understood and analyzed in detail. We will present such a study [43] in the next chapter.

The studies of this section and the previous section apply to the case without any explicit symmetry breaking, i.e. with $b_1 = 0$ in Eq.(4.3). We have repeated these

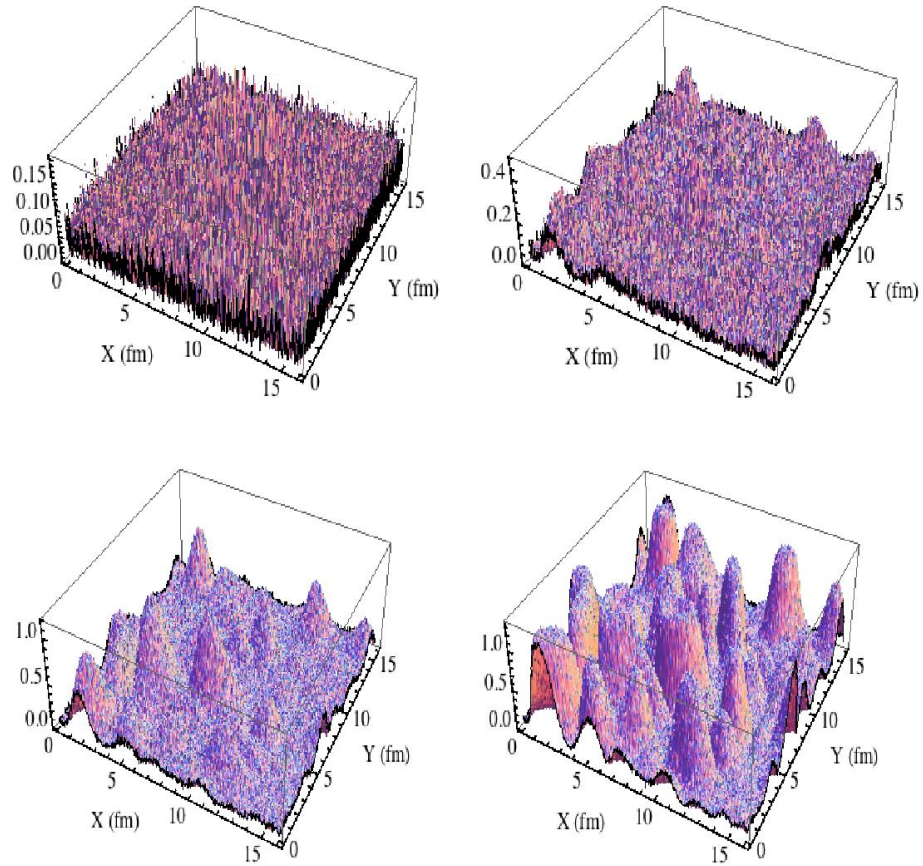


Figure 4.3:

These plots correspond to initial central temperature $T_0 = 500$ MeV. (a)-(d) show the surface plots of $|l|$ during early stages with subsequent formation and growth of bubble like structures just like a first order phase transition. Plots in (a) -(d) are at $\tau = 2, 2.78, 3$ and 3.3 fm respectively, with corresponding temperature being $T = 395, 355, 345, 336$ MeV. These bubble-like configurations are surprising as there is no barrier here, and no metastable vacuum in the effective potential for this temperature range.

simulations with small explicit symmetry breaking effects on the initial conditions. We take $b_1 = 0.005$ as in ref. [76] here as well as in the next section. By small explicit symmetry breaking effects on the initial conditions we mean that the initial patch of l is taken to shift towards $\theta = 0$ vacuum for $T = T_0$ effective potential, while still overlapping with the initial equilibrium value of l . This forces l to roll down to different θ directions at least at some fraction of lattice points, though major fraction now rolls down towards $\theta = 0$. Fig.(4.4) shows sequence of plots showing growth of $Z(3)$ domains in one such case. Here red, green and blue color represent $\theta = 0, 2\pi/3$ and $4\pi/3$ vacuum respectively. We see that one of the vacua ($\theta = 0$) expands dominantly while other domains remain relatively smaller. The $Z(3)$ domain walls in this case are smaller and disappear faster compared to the case without explicit symmetry breaking. The dynamics of bubble like structure retains its qualitative aspects in this case as long as the field rolls down in different directions.

4.5 Strong Explicit Symmetry Breaking and Large Field Oscillations

Now we consider the case when explicit symmetry breaking effects make the initial field configuration completely biased towards $\theta = 0$ direction. Here the initial patch of l rolls down entirely towards $\theta = 0$ direction with angular variations decreasing during the roll down. The dynamics of transition is entirely different in this case. Clearly there is no possibility of different $Z(3)$ domains here, hence no $Z(3)$ interfaces, or QGP strings will form. We also do not see any bubble like structures here as were seen in Fig.(4.3). Instead we find the l settles down to the true vacuum after undergoing huge oscillations, with large length and time scales.

These large oscillations are very similar to coherent oscillations of the inflaton field in the context of inflation in the early Universe [78]. For the inflation, decay of such coherently oscillating field to particles can be via parametric resonance leading to novel features in the reheating of the Universe after inflation. Existence of similar oscillations here raises possibilities of parametric resonance for RHICE and similar novel dynamics of particle production during such early stages of QGP evolution. As

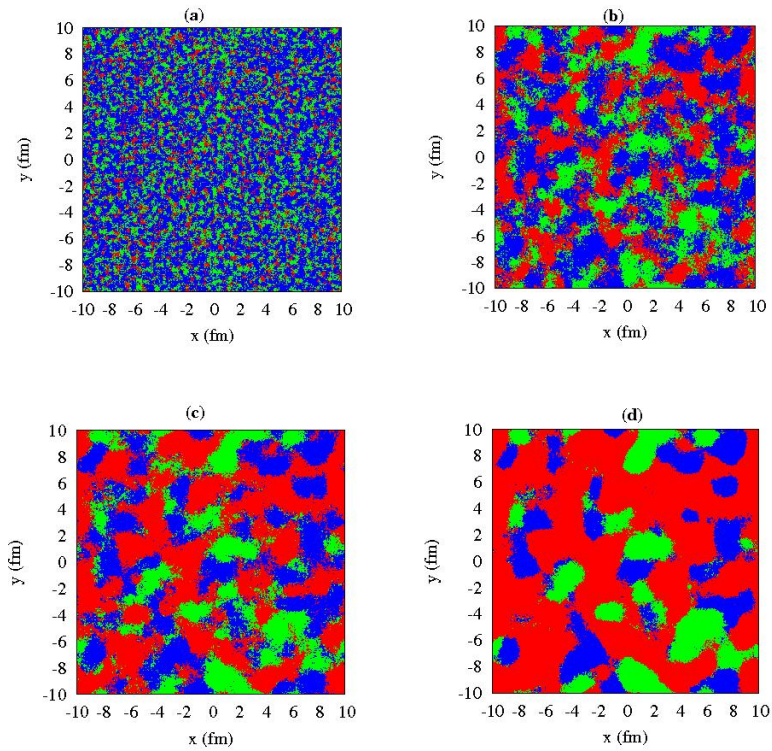


Figure 4.4:

(a) Field configurations at different times with small explicit symmetry breaking effects. The shading (red color) representing dominant region in (d) corresponds to the true vacuum with $\theta = 0$. (a) - (d) show the growth of domains for $\tau = 1.2, 1.6, 2.0,$ and 2.4 fm (with corresponding values of temperature $T = 376, 342, 317, 298$ MeV).

for the universe, new possibilities of thermalization and symmetry changes may arise here.

A direct implication of the existence of such huge oscillations of l in the context of RHICE is its possible effects on the growth of flow anisotropies. In the hydrodynamical studies of elliptic flow in non-central collisions it is known that much of the flow anisotropy develops during early stages of the plasma evolution [84, 85]. In such studies one starts with equilibrium QGP phase where flow develops due to pressure gradients. In view of the possibility of large oscillations during early stages of transition to the QGP phase, the equilibrium starting point of these hydrodynamics simulations becomes suspicious. Our present study does not allow us to address this issue in the context of hydrodynamical evolution. However, even with the field theoretical simulation in this work, we can do a comparative study of momentum anisotropy development with and without the presence of large oscillations of the order parameter field l . For this we proceed as follows.

First we need to model the initial QGP system with appropriate spatial anisotropies. One cannot then use the square lattice with uniform temperature. We use the temperature profile of Woods-Saxon shape with the size in the X and Y directions being different representing elliptical shape for a non-central collision. This allows us to have a well defined size for the central QGP region, with temperature smoothly decreasing at the boundary of this region. The transverse size R of this system (i.e. profile of temperature) is taken to increase with uniform acceleration of 0.015 c per fm, starting from an initial value of R equal to the nuclear radius [85]. The initial transverse expansion velocity is taken to be zero. This expanding background of temperature profile is supposed to represent the hydrodynamically expanding quark-gluon plasma in which the evolution of the order parameter field l will be studied. It may appear confusing as l is expected to represent the QGP phase. Indeed, the normalization of the effective potential in Eq.(4.3) from refs. [59, 60] is carried out precisely so that it represents energy density and pressure of gluons plus quark degrees of freedom. Still, the dynamics of l from Eq.(4.3) does not carry the information of hydrodynamical degrees of freedom. Various particle modes in l need to be excited, which should reach equilibrium, and only then we can expect some sort of hydrodynamical evolution. Clearly the initial field configurations assumed here are far from representing

such a hydrodynamical state. A consistent interpretation of our simulation can be that we are studying long wavelength modes of l which are couple to a background of short wavelength modes which are in thermal equilibrium. This equilibrated background is expanding with velocity as mentioned above, and drives the evolution of large wavelength modes of l via Eq(4.4).

With this interpretation, our task is straight forward. The central temperature of the Woods-Saxon profile is taken to decrease by assuming that the total entropy (integrated in the transverse plane) decreases linearly as appropriate for Bjorken dynamics of longitudinal expansion. Note that, with the transverse expansion being non-zero now, the central temperature will decrease faster than $\tau^{-1/3}$. We show, in Fig.(4.5), a sequence of surface plots of the magnitude of l showing huge oscillations with large length scale during quench. Lattice here is again 2000×2000 but we take a large value of $\Delta x = 0.25$ fm so that the physical lattice size is $50 \text{ fm} \times 50 \text{ fm}$. The Woods-Saxon temperature profile (representing QGP region) is taken to have a diameter of about 16 fm as appropriate for Au-Au collision for RHICE. Large physical size of the lattice allows for the evolution of the QGP region to be free from boundary effects.

At any stage we can calculate the energy momentum tensor $T^{\mu\nu}$ of l . We then calculate the spatial eccentricity ϵ_x of the l field configuration in the standard way,

$$\epsilon_x = \frac{\int dx dy (y^2 - x^2) \rho}{\int dx dy (y^2 + x^2) \rho} \quad (4.3)$$

Where ρ is the energy density. We can also calculate the momentum density at any time using T^{0x} and T^{0y} . Using these components we know the momentum density vector at every stage. By integrating it in angular bins we calculate its various Fourier coefficients, in particular the elliptic flow coefficient v_2 .

4.6 Effects of Large l Oscillations on Flow Anisotropy

To study the effects of large l oscillations on flow anisotropy, we consider two separate cases. Note that now we are considering the cases with explicit symmetry breaking, with its effect being strong on the initial field configuration. First we consider the quench case as described above. Here, we start with the initial field configuration

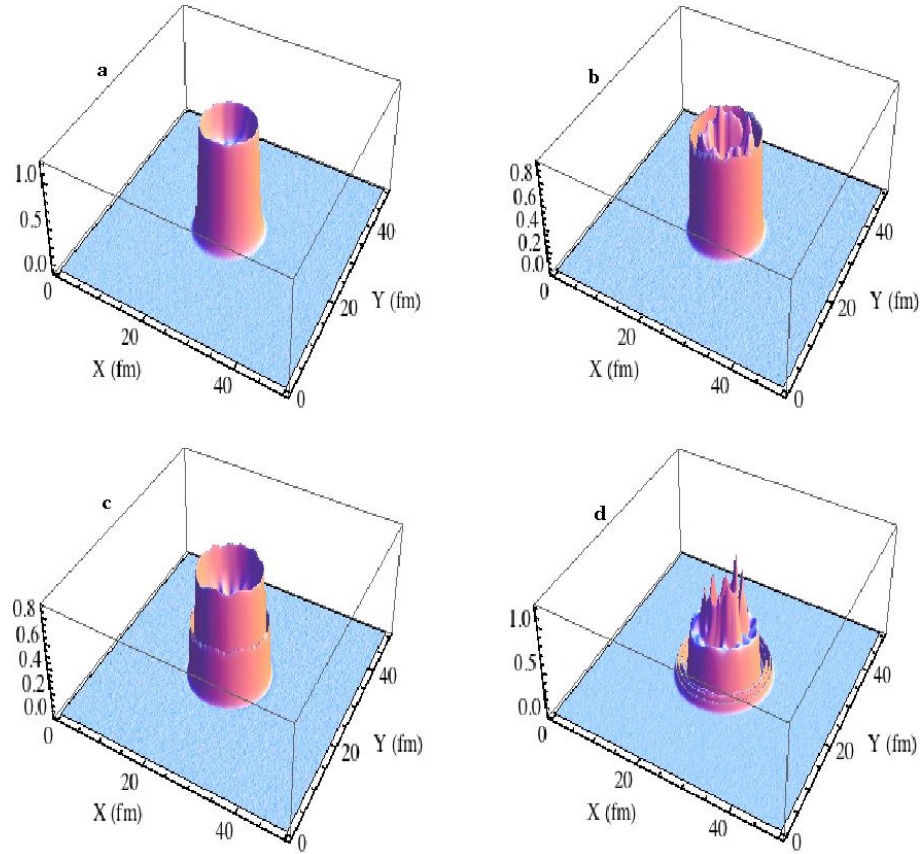


Figure 4.5:

Surface plots of the magnitude of l with circular geometry for the QGP region. (a) - (d) show large oscillations of l during the quench when l rolls down everywhere towards the same vacuum with $\theta = 0$. Plots in (a)-(d) correspond to $\tau = 2.6, 3.6, 4.4, 6.2$ fm/c, with corresponding values of temperature being $T = 281, 251, 228, 191$ MeV, respectively

corresponding to a small patch near the equilibrium point of $T = 0$ effective potential. The patch is taken, as above, with field magnitude randomly varying in angle between 0 and 2π with random amplitude uniformly varying from 0 to 0.01 times the vev of l but now shifted by a constant value of 0.011 times the vev along $\theta = 0$ direction. This simulates the effect of strong explicit symmetry breaking as the entire patch rolls down towards $\theta = 0$ direction. This patch is then evolved with the temperature profile of Woods-Saxon shape as described above with the central temperature having initial value equal to $T_0 = 400$ MeV. As a sample case we give results for the case when the initial (elliptical shaped) temperature profile has an eccentricity of 0.5 (with the major and minor axes being along the x and y axes respectively), which for uniform energy density will correspond to $\epsilon_x = -0.143$ from Eq.(4.5). The initial field configuration rolls down in the entire central region towards roughly $\theta = 0$ direction leading to strong l oscillations. ϵ_x , and flow coefficients, e.g. v_2 are calculated at each stage during the evolution. This is shown in Fig.(4.6). In this section we take the lattice to be 1000×1000 with the physical size of $25 \text{ fm} \times 25 \text{ fm}$. This still allows for sufficient separation of the QGP region (of size 16 fm diameter) from the boundary. Here we show plots (both for ϵ_x and for v_2) for two different realizations of the random initial field configuration (shown as solid and dashed plots). Here, and in all the figures below, we will show plots for a time upto $\tau = 10 \text{ fm}/c$, starting with $\tau = \tau_0 = 1 \text{ fm}/c$ at the initial stage. The central temperature decreases (now faster than $\tau^{-1/3}$ due to nonzero transverse expansion) from an initial value $T = T_0 = 400$ MeV at $\tau = \tau_0 = 1 \text{ fm}/c$ to the final value $T = 147$ MeV at $\tau = 10 \text{ fm}/c$. Note from the difference in solid and dashed plots in Fig.(4.6) that differences in the initial field configuration, which have very small magnitudes, lead to huge differences in the values of ϵ_x and v_2 .

This situation should be compared to the case of equilibrium initial conditions, as appropriate for conventional hydrodynamical simulations. This equilibrium initial condition is implemented in the following manner here. For the initial temperature profile of Woods-Saxon shape (again, with a given eccentricity), with initial temperature $T = T_0 = 400$ MeV, we first need to determine the appropriate l configuration which assumes vacuum expectation value everywhere depending on the local value of the temperature. To achieve this, we first evolve field configuration for 1000 time

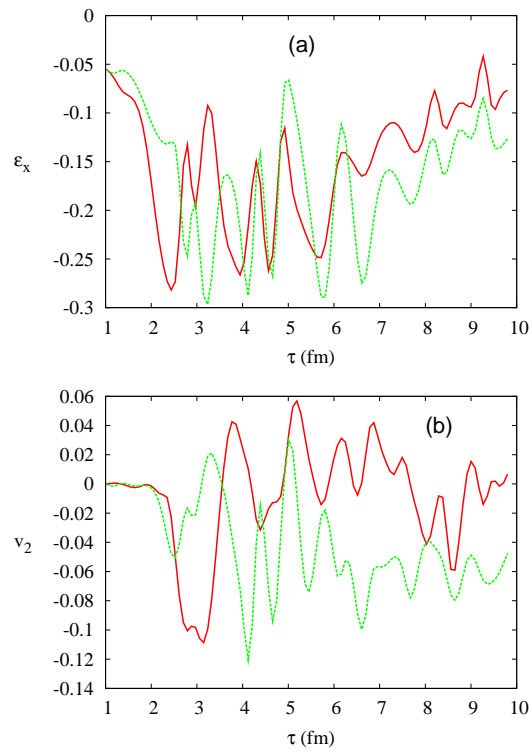


Figure 4.6:

These plots correspond to quench case when initial elliptical shaped temperature profile has eccentricity of 0.5. Solid and dashed plots correspond to two different realizations of the initial random field configuration. (a) and (b) show plots for ϵ_x and elliptic flow v_2 respectively.

steps with highly dissipative dynamics while keeping the temperature profile to remain fixed at the initial profile. A reasonably smooth initial test profile of l is used as the initial field configuration. With highly dissipative evolution, the field everywhere settles to the local minimum of the potential quickly. The final configuration is found to be reasonably independent of the initial configuration assumed for l as long as it is smooth. This final configuration has correct profile as appropriate for the Woods-Saxon profile of temperature representing lowest energy configuration everywhere. In order to make a suitable comparison with the quench case we must incorporate small fluctuations around this *equilibrium* configuration everywhere. For this purpose we add to the value of the field everywhere, a small fluctuating field component with randomly varying angle between 0 and 2π and with random amplitude uniformly varying from 0 to 0.01 times the vev of l (as for the quench case). This new field configuration represents the equilibrium field configuration everywhere, with small fluctuations. This is taken as the initial field configuration for subsequent evolution where now any extra dissipation is switched off. This stage is taken as representing the initial time $\tau = \tau_0 = 1$ fm. The field now evolves with the field equations, Eq.(4.4). Temperature profile also is now allowed to change in time as mentioned above. ϵ_x , and v_2 etc. are calculated at each stage. Fig.(4.7) shows these plots for this equilibrium case, starting from the time slightly after when extra dissipation (to achieve equilibrium configuration) has been switched off. When random fluctuating component is introduced at every lattice site after the end of dissipative evolution, it introduces large gradients. Thus, for a very short time, there are large fluctuations as the field smoothens to certain level. Thus we show plots slightly after (by about 0.2 fm/c) the introduction of random field component.

Comparison of Fig.(4.6) and Fig.(4.7) shows the dramatic effects of quench induced oscillations on flow anisotropies. First note that for the equilibrium case the initial value of ϵ_x is close to the value -0.143 (as shown by the inset in Fig.(4.7)) which exactly corresponds to the initial eccentricity of 0.5 for the temperature profile. This gives us confidence that our procedure of achieving equilibrated configuration works well. In contrast, initial value of ϵ_x for the case of quench in Fig.(4.6) is very different showing the importance of fluctuations for this case. We further see huge fluctuations in the values of ϵ_x and v_2 in Fig.(4.6) compared to the equilibrium case shown in

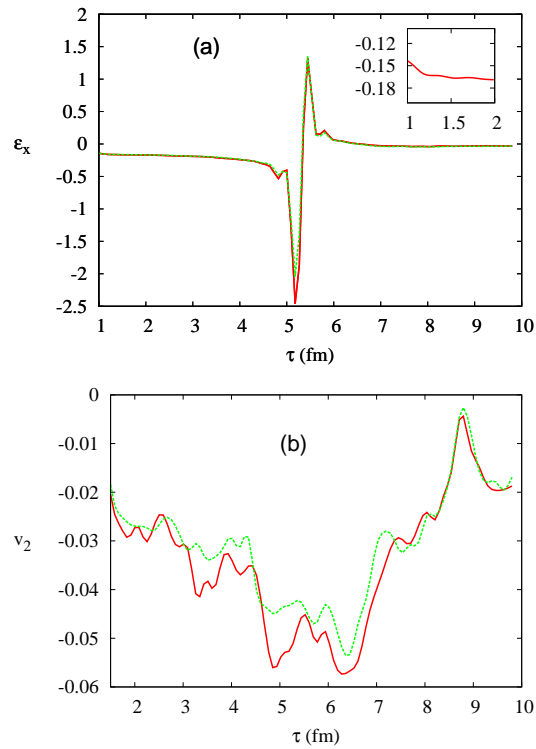


Figure 4.7:

Plots as in Fig.(4.6), now for the equilibrium case. Solid and dashed plots show different realizations of the small random fluctuating part of the equilibrium field configuration. The temperature profile has same initial eccentricity of 0.5 (with corresponding value of $\epsilon_x = -0.143$) as in Fig.(4.6). (a) and (b) show plots of ϵ_x and elliptic flow v_2 respectively. Note, the initial value of ϵ_x for the equilibrated configuration in (a) is very close to -0.143 as shown by the plot in the inset.

Fig.(4.7). Note that though there are oscillations in v_2 for the equilibrium case also, they do not change much from one event to another. In contrast, for the quench case in Fig.(4.6), there are huge variations between the two different realizations, i.e. different events. These large fluctuations in Fig.(4.6) arise due to large oscillations in l which itself depends on the nature of randomness in the initial field configuration. Note that plots for ϵ_x in Fig.(4.7) show a sharp change near $\tau = 5.5$ fm after which ϵ_x settles down to a value close to zero. The central temperature at that stage is about 208 MeV. Presumably a large part of the region (away from the central part where temperature is lower due to a Woods-Saxon profile) may be undergoing transition at that stage leading to large changes in field dynamics. We have checked with the contour plots that the ellipticity of the profile of l , as well as that of energy density, does not undergo rapid changes during this stage. (In fact this is a reflection of a shortcoming in our model where the temperature profile is taken to have definite initial eccentricity, and its further expansion is with definite acceleration as discussed above, starting with zero transverse velocity. A more appropriate model may be to take the time evolution of the spatial eccentricity of the temperature profile from hydrodynamical models and study the evolution of l using that.) We note strong fluctuations in both these quantities around this stage, which may be responsible for these large changes in ϵ_x at this stage. We hope to develop a better understanding of the dynamics during this stage. However, it is important to note that apart from this peak region, everywhere else ϵ_x shows rather stable values settling down to a value close to zero after $\tau \simeq 5.5$ fm, and does not fluctuate much, as compared to the quench case in Fig.(4.6a).

To further illustrate the importance of fluctuations for the quench case, we show plots for the case with zero eccentricity of the QGP region (i.e. for the temperature profile) which also will mean zero value of ϵ_x for uniform density case. Thus, any non-zero ϵ_x and v_2 arise only from the randomness in the initial field configuration. Fig.(4.8a) and Fig.(4.8b) show the plots for the equilibrium case. We note that ϵ_x and v_2 remain very small, apart from a large change near $\tau = 5.5$ fm for ϵ_x , just as in Fig.(4.7). Again, at present what is important to note is that, apart from this peak region, everywhere else ϵ_x and v_2 remain very small for equilibrium case, as expected for the zero eccentricity case. Different plots in Fig.(4.8a) and Fig.(4.8b) correspond

to different realizations of the initial random field configuration. This situation should be contrasted with the quenched case as shown in Fig.(4.8c) and Fig.(4.8d). Note that ϵ_x and v_2 now fluctuate with large amplitudes, even though eccentricity of temperature profile is zero. Further, different realizations of the initial random field configurations lead to widely different plots of these quantities. This shows the fluctuating nature of development of flow anisotropies if large l fluctuations are present. These results suggest the dynamics of the order parameter field, especially such large length scale oscillations may play an important role in determining flow anisotropies and it needs to be incorporated in the hydrodynamical models.

In the next chapter we will discuss the unexpected result of bubble formation in spinodal decomposition in detail. We also discuss different kinds of general potential and check whether bubbles are forming or not in all of them.

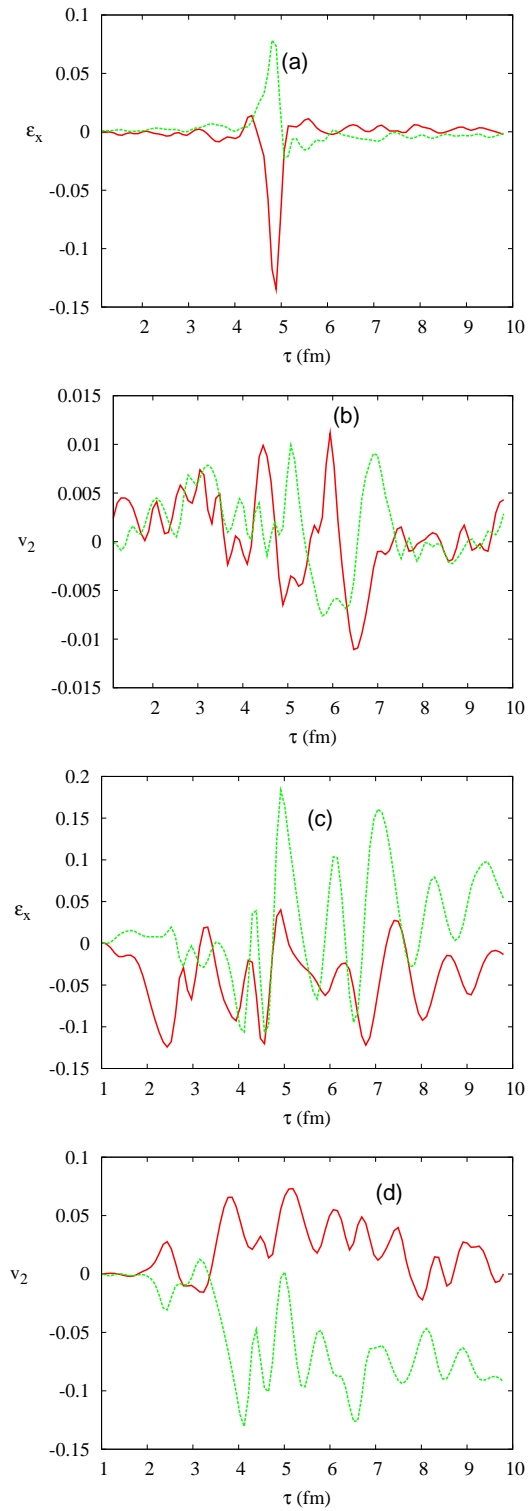


Figure 4.8:

These plots are for the zero eccentricity for the temperature profile. In all the figures here, solid and dashed plots correspond to different realizations of initial random field configuration. (a) and (b) show plots of ϵ_x and v_2 for the equilibrium transition case, while (c) and (d) correspond to the quench case.

Chapter 5

Bubble Formation During Spinodal Decomposition in Heavy-Ion Collisions

5.1 Introduction

Relativistic heavy-ion collision experiments at RHIC and LHC provide evidence for the deconfinement phase transition of QCD [18]. The order of the phase transition between the confined and deconfined phase has been the subject of intense investigation by various lattice QCD groups. These studies find a first order phase transition for SU(3) pure gauge theory [65], then the transition becomes a crossover for full QCD with physical quark masses [86]. These results are mainly applicable for systems in complete equilibrium.

As we discussed in the previous chapter, hydro studies show very small thermalisation time for the fireball, less than 1 fm time. In such a small time, one expects that the fireball is not in a fully equilibrated state. The soft modes will be out of equilibrium during the initial stages of the fireball evolution. So a direct application of lattice QCD results for the deconfinement transition to a fast evolving system such as thermalisation of the fireball in heavy-ion collisions is far from clear. Evolution/thermalisation of the soft modes need to be addressed appropriately. The issue

of soft modes in out of equilibrium has been studied in detail for the deconfinement-confinement phase transition when the fireball cools [87]. For heavy-ion collisions, cooling of the fireball seems to be at a slower pace than the early thermalisation and the deconfinement transition. So the issue of soft modes in out of equilibrium is more important to the deconfinement transition in heavy-ion collisions.

We here present our approach to study the phase transition and the soft modes out of equilibrium by considering the evolution of the soft modes by a quenched effective potential [43]. The hard modes are considered effectively through the parameters of the potential. In the quench an initial thermal state is evolved by a rapidly changing thermodynamic potential. This is achieved through fast increase of the temperature to a value larger than the critical temperature $T > T_c$. The evolution of the soft modes will then depend on the shape of the thermodynamic potential, final temperature and the rate of cooling of the system.

The deconfinement phase transition has been studied in detail for a fully equilibrated system. In general there is a competition between the mechanism of nucleation and spinodal decomposition. Infact, the nucleation probability of the bubble for transition from confined phase to deconfined phase is very small [45,67,68]. So, it is very much unlikely that the phase transition proceeds via bubble nucleation. So, spinodal mechanism is the favored mechanism compared to bubble nucleation for the deconfinement phase transition. It has also been argued that explosive hadron production at BNL RHIC favors the spinodal decomposition scenario from high temperature phase of QGP to low temperature phase of hadrons [59,60,88–93].

The initial temperature of the fireball after thermalisation is expected to be much higher than the critical temperature T_c . It is very unlikely that there is any barrier between the confining and deconfining states at such a high temperature. So a first order deconfinement phase transition via bubble nucleation is unlikely. The confinement phase will simply become unstable and decay. The evolution of this unstable state is carried out via numerical simulation in this chapter. For simplicity we ignore the effect of dynamical quarks. We use the same effective potential proposed by Pisarski as used in previous chapters to study the spinodal decomposition [59,60]. As we have mentioned earlier, this effective potential represents a weak first order phase transition in the vicinity of T_c . So, there is a barrier between stable deconfined state

and meta-stable confined state near and above T_c . The barrier between true vacuum and false vacuum vanishes when the temperature of QGP is higher than 250 MeV. So, after this temperature, there is spinodal decomposition of the field. In our approach the system is rapidly quenched from low temperature confined phase to high temperature deconfined phase. This is achieved through rapid change of the temperature variable, in the effective potential, to $T_0 = 400$ MeV in $1fm$ time. Then the system is allowed to cool with the temperature profile in proper time given by the Bjorken longitudinal expansion [31].

As we discussed in the previous chapter (Sect. 4.4), there are bubble like structures in a spinodal decomposition even without any metastable vacuum. Thus, the deconfinement transition turns out to be very similar to a first order transition, with spontaneous nucleation of bubbles and their coalescence. This is surprising as the potential exhibits no local minima. As we will see below, the fourier analysis clearly shows that medium wavelength modes dominate during the time when bubbles nucleate. To exclude that the first order transition is not due to local minima appearing due to cooling to low temperature we fixed the temperature at $T = T_0$ and evolved the system. This, however, did not change the nature of the transition. We repeated our simulations for the case with $U(1)$ symmetry in place of the present $Z(3)$ symmetry. The results remained qualitatively similar. We also considered the simulations without any Φ^3 term in the effective potential. In this case however we found results consistent with conventional spinodal decomposition with enhancement of long wavelength modes and without any bubble like structure. This suggests to us that the presence of Φ^3 term changes the dynamics of spinodal decomposition, and gives rise to a transition similar to a first order transition.

5.2 Effective Potential

This effective potential is described in detail in chapter 3 of this thesis. The effective Lagrangian density and effective potential are given by Eq.(3.2) and Eq.(3.3) respectively.

The effective potential at a temperature 400 MeV along $\theta = 0$ is shown in the Fig.(5.1). There is no metastable barrier at this temperature as shown in this figure.

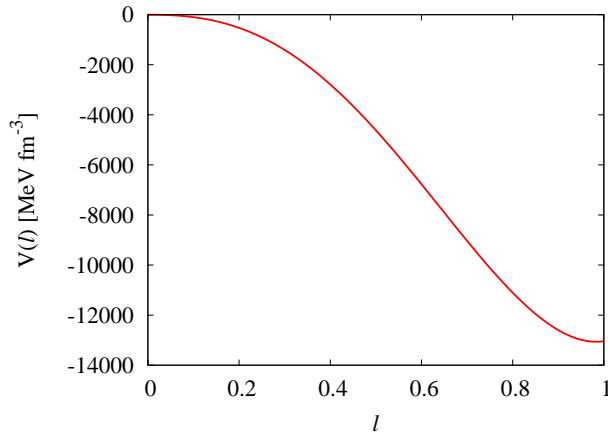


Figure 5.1: Plot of $V(l)$ in $\theta = 0$ direction for $T = 400\text{MeV}$.

5.3 Numerical Techniques

The numerical techniques used for this simulation is already discussed in chapter 4 and sec.(4.3) of this thesis. So we don't repeat it here. The fourier modes are studied by using the 2D fast fourier transform algorithm of field configuration on the lattice at each time. We calculate how the power in different k modes varies with respect to time. The power of some medium wavelength modes increases compared to higher wavelength modes when the bubbles start forming.

5.4 Bubble Formation during Spinodal Decomposition

In a general spinodal decomposition mechanism, field just rolls down to the true vacuum of the potential. As for example, consider U(1) theory, where field rolls down in every direction and forms string defects. In this case, long wavelength modes get enhanced the most. Now, consider spinodal mechanism in case of confinement deconfinement phase transition in Relativistic heavy-ion collision experiments. In Relativistic heavy-ion collision experiments, the system temperature increases suddenly from zero temperature to a very high temperature (400 MeV for RHIC and

higher for LHC). Here, the system is quenched from low temperature to high temperature in a very short period of time. We study this quenching effect in the context of Polyakov loop as order parameter and effective potential described by Eq.(3.3).

After the quench of the system to a very high temperature, the field still sits near the confined vacuum initially. So, the field magnitude is almost constant near $l = 0$ and phase varies randomly from $\theta = 0$ to $\theta = 2\pi$. Then, field evolves according to the Euler Lagrange equation of motion with the effective potential. The plasma temperature decreases as $\tau^{-1/3}$ according to Bjorken expansion [31]. The quench effect on the transition from a high temperature symmetry restored phase to a low temperature symmetry broken phase has been studied in [94] in the context of Linear Sigma model. They show that higher wavelength modes grow exponentially, while short wavelength modes remain almost in equilibrium. In our spatial fourier transform study of different modes, we observe some medium wavelength modes increasing compared to higher wavelength modes at time around 5 fm as shown in Fig.(5.5), this is the time when bubbles appear. But, this is a quench effect, and there is no barrier between true and false vacua, so we do not expect any bubble nucleation like in a first order transition .

The bubble like structure in this quench effect is surprising. We will now discuss details of the potential structure and initial configuration to understand the formation of these structures. The bubbles are formed during spinodal decomposition because of the initial fluctuations and the presence of l^3 term in the potential. Initially, the field magnitude is very small near $l = 0$, but the phase of field varies randomly from $\theta = 0$ to $\theta = 2\pi$. Here, the initial configuration is such that there is large gradient energy due to random phase of field. Using mean field analysis, one can see that the radius of instability in the momentum space is larger in the presence of l^3 term. This leads to enhancement of medium wavelength modes due to higher phase space volume. We also suggest a plausible explanation for the appearance of these bubble like structures in this case. It may happen that the parameters of the potential (for which there is no barrier) get modified due to the fluctuations in the initial configuration coupled with l^3 term in the potential effectively creating a barrier. (Modification of the Polyakov loop potential due to the presence of fluctuations has also been discussed in ref. [87].) In such a situation, the field will hop over the barrier due to large gradient energy.

This may explain bubbles appearing in this situation. For the potential without l^3 term, with same initial configuration, bubbles don't appear. So l^3 term appears to be important for the barrier to reappear for bubble nucleation. Even with the presence of l^3 term in the potential, but with initial smooth configuration of the field (with uniform random phase), bubbles don't appear. The initial smooth configuration of field does not have enough fluctuations to modify the shape of the potential. So, in summary, we suggest that the important thing for bubbles to appear in spinodal decomposition mechanism may be the presence of l^3 term in the potential and initial thermal fluctuations of the field.

The spinodal decomposition of field during fast expansion of the system and bubble formation during slow expansion of the system, for a weakly first order transition case, has been studied in [87]. In our simulation, we consider the case when there is no metastable vacuum. we concentrate on central rapidity region and take the system temperature to increase linearly upto 400 MeV in 1 fm time. We have used Bjorken longitudinal expansion for QGP where temperature varies as $\tau^{-1/3}$. The $|l|$ histogram plot at different times shows how the field evolves. At $t=0$ the $|l|$ histogram shows a peak near $l = 0$ which corresponds to confined phase. As the field evolves for some time upto 1 fm, it is still more populated near $l = 0$. We only show $|l|$ histogram at later time steps in Fig.(5.2a), where the two peak structure (one is near $l = 0$ and other is near $l=0.7$) is more clear. This is a clear sign of phase mixing and a first order phase transition. At later times, the height of the peak at $l = 0$ decreases corresponding to the transition from confined phase to deconfined phase. The peak at larger l becomes more broader and higher when more bubbles form and bubbles expand.

Since these bubbles are produced in this quenched system due to random phase configuration, these bubbles are very narrow shaped during formation. The phase of these bubbles are nearly uniform inside the bubble and varying randomly outside the bubble .

Next we consider some general constant potentials with Φ^3 and without Φ^3 term to study spinodal decomposition scenario and to compare the results.

Let's consider a potential without Φ^3 term

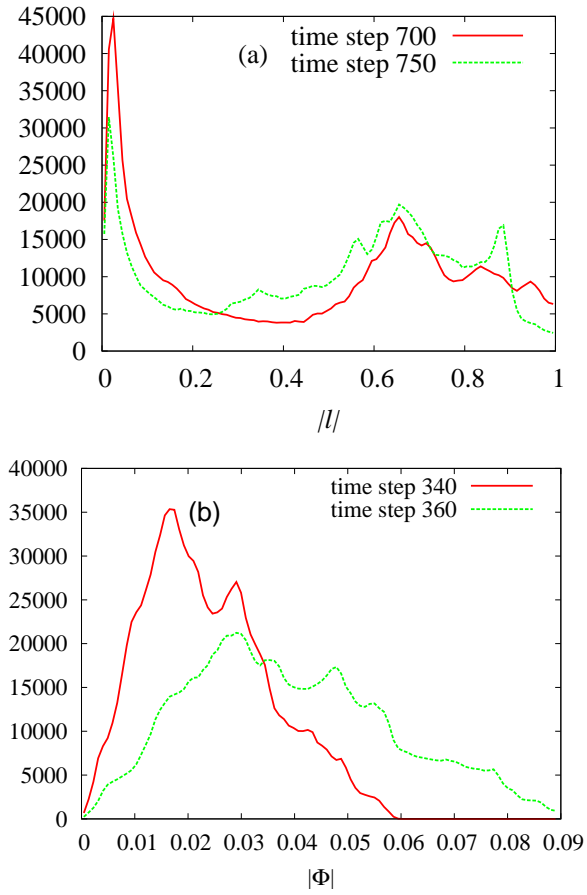


Figure 5.2:

(a) Histogram of $|l|$ at different times for the potential with l^3 term as in Eq.(3.3) and (b) Histogram of $|\Phi|$ at different times for the potential with no Φ^3 term as in Eq.(5.1)

$$V(\Phi) = -a|\Phi|^2 + c|\Phi|^4 \quad (5.1)$$

where $a = 0.004$ and $c = 0.25$. This represents a general potential with U(1) symmetry. This potential has similar form as shown in Fig.(5.1). It does not have any central barrier between false vacuum $\Phi = 0$ and true vacuum $\Phi =$ vacuum expectation value $= 0.09$.

We consider spinodal decomposition of the field with this potential. The initial configuration is such that its magnitude is near $\Phi = 0$ and the phase of field varies randomly. The field evolves according to Euler Lagrange equation of motion. The field magnitude and phase plot are shown in Fig.(5.6) and (5.7) respectively. As explained earlier, we don't get any bubble in this case due to the absence of Φ^3 term in the potential. The $|l|$ histogram plot for this case is shown in Fig.(5.2b). There is a peak initially at $\Phi = 0$ and then the field spreads over a large range of Φ at later times. There is a qualitative difference between the plots of Fig.(5.2a) and Fig.(5.2b). Also, the two peak structure is not there in Fig.(5.2b) as in Fig.(5.2a). This is the situation with spinodal decomposition without any bubble formation. We will discuss more about this in section 5.5.

We also consider spinodal decomposition of the fields with general U(1) potential with Φ^3 term

$$V(\Phi) = -a|\Phi|^2 - b|\Phi|^3 + c|\Phi|^4 \quad (5.2)$$

where a and c has the same value as in Eq.(5.1) and $b = 0.5$. This potential also does not have central barrier between true and false vacuum as in Eq.(5.1). The initial configuration is same as described above. But, due to the presence of Φ^3 term in the potential, it has bubble formation during spinodal decomposition. $|l|$ histogram for this case is similar to Fig.(5.2a), so we don't show it here.

5.5 Results

This sections consists of two subsections where the first part describes the heavy-ion collision and the second part describes general kind of potential with Φ^3 and without Φ^3 term.

5.5.1 Bubble formation in heavy-ion collision

The confinement deconfinement transition in the context of RHICE has to be studied with temperature evolution in accordance with longitudinal expansion and with negligible effect of transverse expansion. As explained in chapter 3 of this thesis, we simply use field equations resulting from Bjorken's longitudinal scaling model for the evolution of the field configuration for the entire simulation, excluding the initial pre-equilibrium phase from $\tau = 0$ to $\tau = \tau_0$. The heating of the system until $\tau = \tau_0$ will be represented by the increase of the temperature from 0 upto $T = T_0$. After τ_0 , with complete equilibrium of the system, the temperature will decrease according to the equations in the Bjorken's longitudinal scaling model.

The appearance of bubbles during confinement deconfinement phase transition is due to the initial random phase configuration. Also, the initial field magnitude has to be one order magnitude smaller than the vacuum expectation value of the potential. When the magnitude of field is still smaller, bubbles don't appear in the time range (~ 10 fm) suitable for the relativistic heavy-ion collisions. This is due to the small magnitude of field, it does not have large gradient energy to modify the potential. Hence there is no effective barrier and in this case the field decays via usual spinodal decomposition mechanism. Also, there is dissipation of energy density due to Bjorken expansion. But, if we take a larger lattice say 50 fm (which is not suitable for heavy-ion collision case) with the same potential. Even if the initial field magnitude is very small, due to larger size of lattice, the gradient energy of the field over a patch is large such that it hops over the barrier created. So bubbles appear in this large lattice.

For some initial time the field fluctuates a lot, around 5 fm time bubble start forming and the temperature of the system is about 240 MeV. It should not be misleading that these bubbles form at this temperature because there is a metastable barrier between true and false vacua at this temperature. To check this, we also run a simulation with maximum temperature of the order of 500 MeV at 1 fm time and in this case bubbles appear at a temperature greater than 250 MeV where there is no metastable barrier. This will also be clear in the next subsection where we will discuss constant temperature during the evolution of field, these bubbles appear where there is no barrier between true and false vacua. We see bubbles in this because the

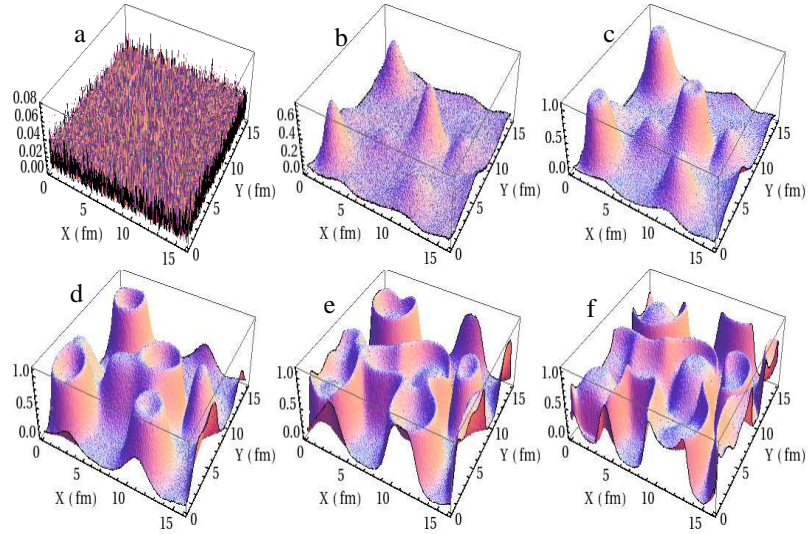


Figure 5.3:

(a)-(f) show plots of profiles of l for the potential in Eq.(3.3) at $\tau = 2, 5.5, 6, 6.5, 7$ and 7.5 fm respectively

parameters of the potential has been changed creating a barrier between them. But the most realistic situation for a first order phase transition is that bubbles should nucleate before 1 fm time such that bubbles get sufficient time to expand and convert the whole region to QGP. If we have a larger lattice say 50 fm (not suitable for heavy-ion collision), then we get the bubbles at earlier times ~ 1 fm time. It is of great importance to study the details of the difference between bubbles in case of first order phase transition and bubbles forming in this mechanism. In this case, all bubbles don't nucleate at the same time. Whenever the gradient energy of the field over a patch is large to hop over the barrier, bubbles form. These bubbles expand very fast at a speed of 0.9 . Fig.(5.3) and Fig.(5.4) represents the magnitude and corresponding phase of field on the lattice at different times. The phase plot shows uniform theta inside the bubble. For this case there are 3 possible phases corresponding to 3 degenerate vacua. The different phases are separated by domain walls and when 3 different phases meet, string is produced.

Fig.(5.5) represents the evolution of different fourier modes for this case. As explained earlier, during bubble formation, some medium wavelength modes grow

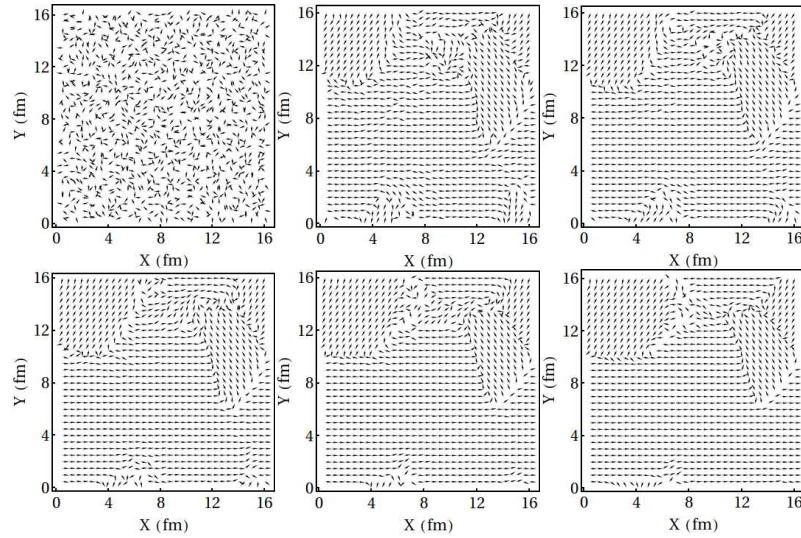


Figure 5.4:

(a)-(f) show plots of phases of l for the potential in Eq.(3.3) at $\tau = 2, 5.5, 6, 6.5, 7$ and 7.5 fm respectively

faster. The medium wavelength modes grow much larger compared to highest wavelength ($k=0$) modes. This can be compared with the case when there are no bubbles (potential without Φ^3 term). The medium wavelength modes don't grow larger compared to higher wavelength modes.

We also study this mechanism by taking uniform random number generator as well as Gaussian random number generator. The results are independent of the random number generator chosen. We also did the simulation taking different seed of random number generator. The qualitative aspects of the results remain unchanged. We also did the simulation with constant potential (i.e potential with temperature fixed), the physical picture remains unchanged in this case.

5.5.2 (ii) Bubble formation in general potentials

Let's first consider the potential described by Eq.(5.1). Due to the absence of Φ^3 term in the potential, there are no bubble formation in this case. Fig.(5.6) and Fig.(5.7) represent the magnitude and corresponding phase of field on the lattice at different timesteps respectively. The strings which corresponds to $\Phi = 0$ can be seen in Fig.(5.6f). Since the potential has infinite degeneracy, the phase plot at later times

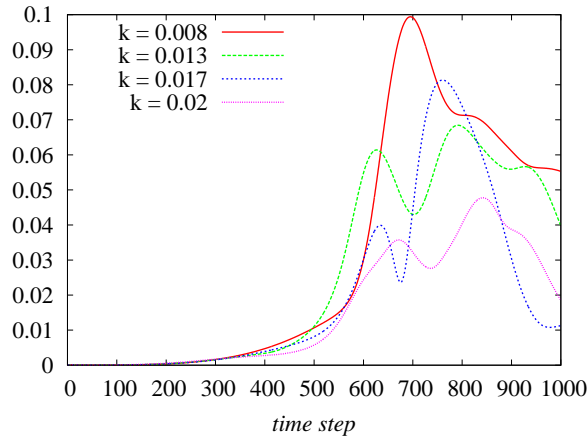


Figure 5.5:

This plot shows evolution of the square root of power of different fourier modes (in terms of lattice spacing) for the potential in Eq.(3.3).

show the variation of phase. Fig.(5.8) represents the evolution of different fourier modes. Here the higher wavelength modes increase compared to lower wavelength modes.

Now consider the potential described by Eq.(5.2) with Φ^3 term. Fig.(5.9) represents the magnitude of the field at different time steps. At time step 140, the bubbles start forming, after that bubbles coalesce to complete the transition. The phase plot of field is similar to Fig.(5.7). So, we don't show it here. The time evolution of fourier modes are shown in Fig.(5.10), here the lower wavelength modes increase compared to higher wavelength modes during bubble formation as shown in Fig.(5.5).

5.6 Discussion

We study the spinodal decomposition of Polyakov loop order parameter in the context of heavy-ion collision. Even in the absence of any metastable confining vacuum, true vacuum bubble like structures are formed during the transition. Our study suggests that the initial random fluctuations coupled with the l^3 term give rise to this type of dynamics for the transition. We also checked some general potential with and without l^3 term, the results are consistent with this conclusion. A plausible explanation for this may be as follows. Although these potentials do not have a barrier to nucleate

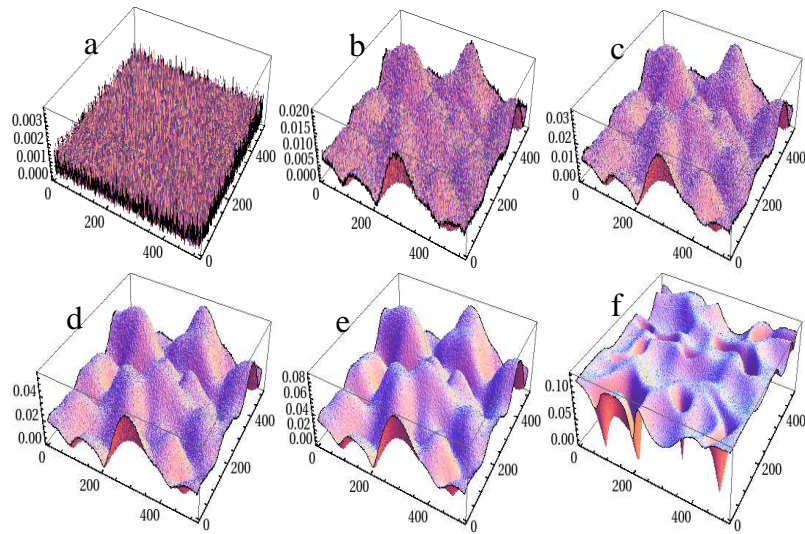


Figure 5.6:

(a)-(f) show plots of profiles of Φ for the potential in Eq.(5.1) at timesteps 20, 300, 320, 340, 360 and 440 respectively

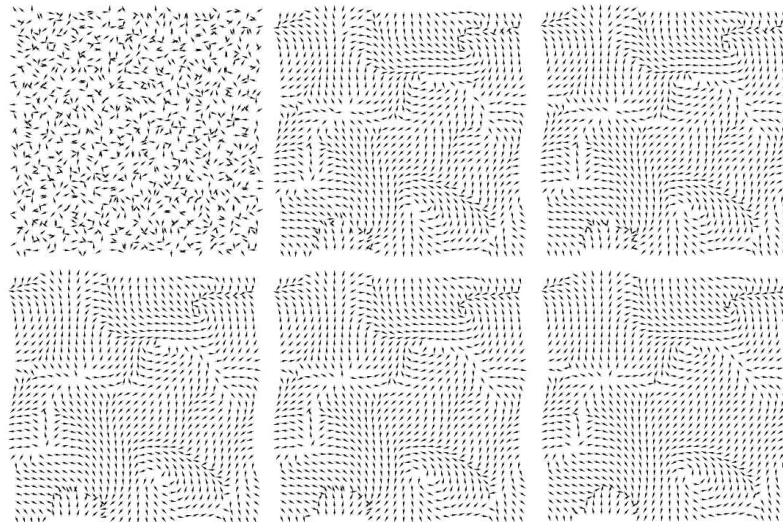


Figure 5.7:

(a)-(f) show plots of phases of l for the potential in Eq.(5.1) at timesteps 20, 300, 320, 340, 360 and 440 respectively

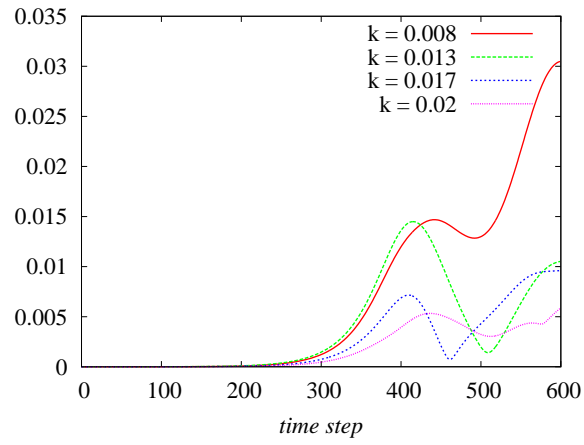


Figure 5.8:

This plot shows the evolution of square root of power of different fourier modes (in terms of lattice spacing) for the potential in Eq.(5.1)

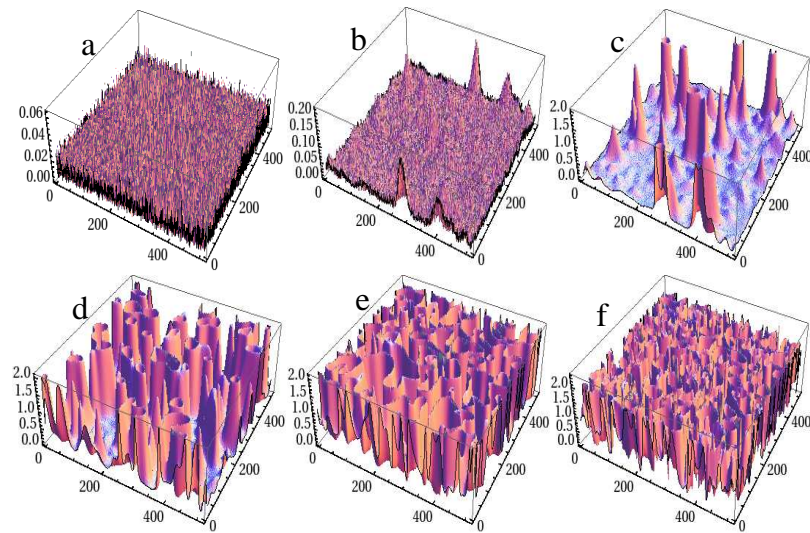


Figure 5.9:

(a)-(f) show plots of profiles of l for the potential in Eq.(5.2) at timesteps 20, 120, 140, 150, 160 and 180 respectively.

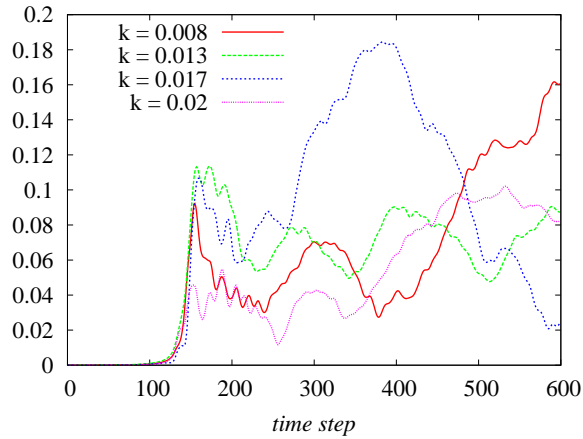


Figure 5.10:

This plot shows the evolution of square root of power of different fourier modes (in terms of lattice spacing) for the potential in Eq.(5.2)

bubbles, due to the presence of l^3 term and huge gradient energy over a patch on the lattice, the coefficients get modified and create an effective barrier. So, bubbles are nucleated due to the hopping of field over this barrier. We also see the enhancement of medium wavelength modes compared to higher wavelength modes during the bubble formation.

With these studies about the nature of the phase transition, it is equally important to study signature of the transient state of QGP. As we have discussed in the introduction, elliptic flow is one of the most important signature of QGP. There are several methods to measure the elliptic flow such as event plane method, particle correlation method etc. In the next chapter, we will discuss another analysis technique to quantify the elliptic flow. This analysis technique also identify the event plane.

Chapter 6

Analyzing Elliptic Flow Anisotropy with Excursion Sets in Relativistic Heavy-Ion Collisions

6.1 Introduction

Elliptic flow is one of the most important probes of the formation of new thermalised quark gluon plasma phase in RHICE. We have discussed elliptic flow anisotropy as a signature of QGP in the introduction. There are various methods to measure elliptic flow coefficient and higher order flow anisotropies like event plane method, particle correlation method, Lee-Yang zero method etc.

In this chapter, we present a different analysis technique to measure elliptic flow anisotropy in relativistic heavy-ion collisions [34]. This technique has also been used to probe anisotropic expansion history of the universe starting from inflationary stage to the surface of last scattering by studying CMBR fluctuation patches [95]. There the basic idea is the following : if the density perturbations generated initially by inflation are statistically isotropic, then the average shape of spherical fluctuation patches will become ellipsoidal due to anisotropic expansion of the universe for some time along one direction. Even if the universe expands isotropically after that, the deformation remains printed in superhorizon fluctuation patches. Hence by studying the shapes of superhorizon fluctuation patches, one can know the anisotropic expansion factor

of the Universe.

Temperature fluctuations of CMBR are represented on the surface of a two sphere. If there is larger expansion in one direction, say along the Z-axis, then the fluctuation patches at the equator will be most sensitive to it. What one wants to know here is the distribution of widths in the ϕ direction (called as X direction) and compare it with the distribution of widths in the θ direction (called as Y direction), where θ and ϕ are the latitude and longitude respectively. For this we proceed as follows. We divide the entire 20° wide equatorial belt (with θ within $\pm 10^\circ$ about the equator, and ϕ ranging from 0 to 360°) into thin slices (varying from 0.02° - 0.1°) in X and Y directions (to increase statistics). Using these slices, we determine the X and Y extents of various filled patches. A comparison of the distribution of these X and Y width of fluctuation patches gives information about anisotropic expansion of the Universe.

The anisotropic expansion of the universe has very strong similarities with the anisotropic flow expected in RHICE. The situation of anisotropic expansion of the universe is directly realized in the form of elliptic flow for non-central events. In case of non central collision, there is spatial anisotropy in the transverse plane and there is larger flow along x direction compared to y direction. Here x-axis represents impact parameter direction. So, the fluctuation patches near x-axis will not know about the expansion, but the patches which are near y-axis will be stretched more in x direction. When we will study the histogram of size distribution of fluctuation patches near x-axis and y-axis, there will be more large size patches near y axis compared to x axis and more small size patches near x axis compared to y axis. The technique analyzes shapes (sizes) of patches above (below) certain threshold value for transverse energy/particle number (the excursion sets) as a function of the azimuthal angle and rapidity. In case of a central collision, where there is no anisotropic expansion, one would expect that the two histograms of size distribution of fluctuation patches near $\phi = 0$ and $\phi = 90$ or any two histograms at some azimuthal angle difference (90° or any other) almost overlap. In case of non central collision, the two histograms of size distribution of fluctuation patches near $\phi = 0$ and $\phi = 90$ give the maximum difference due to anisotropic expansion. The histograms at any other azimuthal angle (at a 90° separation) gives less difference compared to above case.

Hence, this technique can also be used to identify event plane in each event. One can compare the two histograms at different azimuthal angles (at 90° separation), the histograms which give maximum difference determines the event plane.

6.2 Different methods to measure elliptic flow anisotropy

6.2.1 Event Plane Method

To measure flow coefficients, one first needs to know the reaction plane angle. This is the plane containing beam axis and impact parameter vector direction. However, it is very difficult to know the reaction plane angle exactly event by event in experiments. The estimated reaction plane is called event plane [96].

The method uses the anisotropic flow itself to determine the event plane. It also means that the event plane can be determined independently for each harmonic of the anisotropic flow. The event flow vector Q_n and the event plane angle Ψ_n from the n th harmonic of the distribution are defined by the equations

$$Q_n \cos(n\Psi_n) = X_n = \sum_i w_i \cos(n\phi_i), Q_n \sin(n\Psi_n) = Y_n = \sum_i w_i \sin(n\phi_i), \quad (6.1)$$

The event flow vector Q_n is a 2d vector in the transverse plane. The sums go over the i particles used in the event plane determination and the w_i are weights. In general the weights are also optimized to make the reaction plane resolution the best. Sometimes it can be done by selecting the particles of one particular type, or weighting with transverse momentum of the particles, etc. Usually the weights for the odd and even harmonic planes are different.

The event plane angle is the azimuthal angle of Q_n calculated as

$$\Psi_n = \left(\tan^{-1} \frac{\sum_i w_i \sin(n\phi_i)}{\sum_i w_i \cos(n\phi_i)} \right) / n. \quad (6.2)$$

The observed v_n is the n^{th} harmonic of the azimuthal distribution of particles with respect to this event plane

$$v_n^{\text{obs}}(p_t, y) = \langle \cos[n(\phi_i - \Psi_n)] \rangle \quad (6.3)$$

Since finite multiplicity limits the estimation of the angle of the reaction plane, the v_n have to be corrected for the event plane resolution for each harmonic given by

$$r_n = \langle \cos[n(\Psi_n - \Psi_{RP})] \rangle \quad (6.4)$$

So, the final flow coefficients value depend upon how accurately this resolution of event plane is determined. We will not discuss the details of the event plane resolution calculation here.

6.2.2 Particle Correlation Method

The *pair-wise correlation method* [97], is based on the fit of the two-particle azimuthal distribution to that expected from anisotropic flow:

$$\frac{dN^{pairs}}{d\Delta\phi} \propto (1 + \sum_{n=1}^{\infty} 2v_n^2 \cos(n\Delta\phi)) \quad (6.5)$$

This method does not require determination of event plane event by event. Here all pairs of particles in a given momentum region are correlated with the event plane.

The *two-particle cumulant method* differs from the previous one only in that instead of the fit to the two-particle distribution, it calculates the coefficients directly as

$$v_n[2]^2 = \langle \cos[n(\phi_1 - \phi_2)] \rangle = \langle u_{n,1} u_{n,2}^* \rangle \quad (6.6)$$

for all pairs of particles, where $u_n \equiv e^{in\phi}$ is a particle's unit flow vector.

This method can be generalized to many particle correlation method [98] which is almost independent of nonflow correlations.

6.3 Our method: Construction of Excursion Sets

Here we consider fluctuations of transverse energy or particle number as a function of the azimuthal angle and rapidity. These fluctuations are like temperature fluctuations in CMBR at the surface of last scattering. So, considering fluctuations above/below a certain threshold value, we generate the excursion sets of fluctuations like in CMBR, we call them simply as fluctuation patches. Here we use HIJING event generator

and get the information of final particles produced in a heavy-ion collision event by event. To detect anisotropic flow, we model flow by imparting extra anisotropic momentum to the momentum distribution of particles obtained from HIJING [99]. We then analyze the shape/size distribution of the fluctuation patches at two different azimuthal angles. We will see that azimuthal angles with maximum difference in the two distributions identify the event plane, and the magnitude of difference relates to the magnitude of momentum anisotropy, i.e. elliptic flow.

For analyzing anisotropic expansion history of the universe in [95], we had examined the size distribution of patches on the surface of last scattering (which is a two sphere S^2) along θ and ϕ directions. This will be different for RHICE. Since our interest is in probing flow anisotropy in the transverse plane, say the elliptic flow in a non-central event, we would like to compare the shape/size distribution of fluctuations along the X axis with that along the Y axis, where the X and the Y axis correspond to the event plane. We model anisotropic flow in HIJING by multiplying a factor f_{p_x} to the momentum P_x of every final state particle. For central events f_{p_x} is taken to be 1 while for non-central events f_{p_x} is taken to vary from 1.1 to 1.4 representing the momentum anisotropy resulting from elliptic flow. Precise value of momentum anisotropy represented by f_{p_x} is not an issue here (though the values used here are of right order of magnitude, say, $f_{p_x} = 1.2$ implying about 20 % anisotropy). Our intention is only to show the systematic pattern in which the difference between the size distributions of excursion sets at different azimuthal angle probe the event plane and strength of elliptic flow. The only way to get a quantitative correspondence of these results is by doing only hydrodynamical simulations.

With the (anisotropic) momentum distribution of particles from HIJING, we collect particle numbers as well as transverse energy in different ϕ and y bins where ϕ is the azimuthal angle in the event plane and y is the rapidity. We use 100 bins for full 2π range of ϕ and 100 bins for the full range of y . By considering smaller range of rapidity y , the results are similar. Full range of y gives better statistics. To exclude very large values of y we use a lower cutoff for $P_T \simeq 150$ MeV. For each event thus we get the particle number/transverse energy as a function of ϕ and y . By subtracting the average values of these quantities we get particle number fluctuations/transverse energy fluctuations as a function of ϕ and η . We then consider a threshold value for

these fluctuations and consider only those ϕ, y bins where particle number or transverse energy fluctuations is above (or below) this threshold value. This provides us with the excursion sets for the relevant fluctuations. Fig.(6.1) shows the excursion sets for transverse energy fluctuations obtained from HIJING for a single Au-Au collision event at $\sqrt{s_{NN}} = 2$ TeV. Here, we will be presenting results for transverse energy fluctuations. results for number fluctuations are very similar to these, hence we do not discuss them separately.

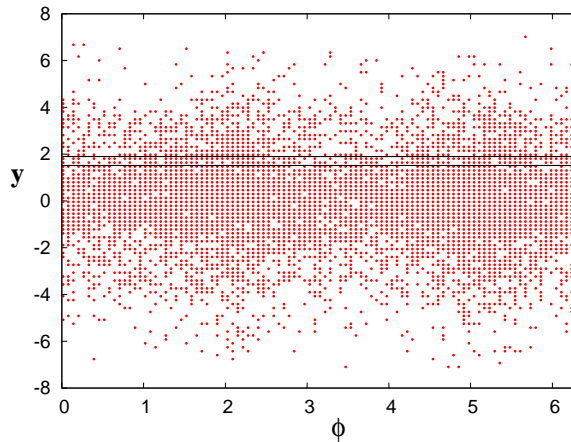


Figure 6.1:

Plot of excursion sets (fluctuation patches) in the azimuthal angle ϕ (in radians) and the rapidity y space. Horizontal solid lines show the slicing used for widths of filled patches.

6.4 Results

We consider here non-central events with the impact parameter lying between $b = 3-4$ fm. Here we have used $f_{p_x} = 1.2$ (for modification of the momenta of particles from HIJING) and fluctuations above $0.2 \times$ maximum fluctuation have been included to generate the excursion sets. We use here large collision energy as relevant for LHC. The size distributions for small number of particles have large statistical errors. For the case of RHIC energies one will need to combine much larger number of events to control statistical errors.

We have to calculate the average width of the fluctuations along ϕ direction near

$\phi = 0$ and compare it with the similar average width near $\phi = \pi/2$. This will probe the elliptic flow. The same result will be obtained by comparing distributions at $\phi = \pi$ and $\phi = 3\pi/2$. We determine the distribution of widths along the ϕ direction in a 45° wide arc centered at $\phi = 0$ and compare it with the distribution of widths (again, in a 45° wide arc) centered at $\phi = \pi/2$. To calculate these distributions we proceed as follows. We divide the entire region shown in Fig.(6.1) (with y varying within full range, and ϕ ranging from 0 to 360°) into thin slices (with a rapidity width of 0.18) along the ϕ direction, as shown by horizontal lines in Fig.(6.1). Using these slices, we determine the ϕ widths of various filled patches. We then plot the frequency distributions (histograms) of the widths of the intersections of all the patches with these slices at $\phi = 0$ and at $\phi = \pi/2$ (within 45° arcs). For the isotropic expansion case, without any flow anisotropy, we expect these two histograms to almost overlap. For anisotropic expansion case we expect that fluctuation patches will be stretched more at $\phi = \pi/2$ than at $\phi = 0$, as system expands faster along $\phi = 0$ (and $\phi = \pi$) directions for a non-central collision. Any relative difference, between the two histograms will, therefore, imply the presence of an anisotropy of expansion (apart from the possibility of any initial anisotropy, we will discuss it below).

Fig.(6.2a) shows the frequency distributions (histograms) of the widths of the intersections of the slices with the filled patches (excursion sets) at $\phi = 0$ (solid curve) and $\phi = \pi/2$ (dashed curve) for the case with $f_{p_x} = 1$ (i.e. no momentum anisotropy). The horizontal axis corresponds to the widths of the slices (in radians) along ϕ , with histogram bin having width of 0.05 radians. The vertical axis gives the frequency N of the occurrence of the respective widths in all the slicings of excursion sets (such as in Fig.(6.1), but now for $f_{p_x} = 1$). The error bars denote the statistical uncertainty of \sqrt{N} for the frequency N in each bin. As we are comparing distributions for two different data sets (one at $\phi = 0$, the other at $\phi = \pi/2$), we normalize the distributions, as well as the errors, with the total number of particles included for each data set. We combine histograms of 500 events in HIJING with the X axis of each event (with same event parameters such as the impact parameter, collision energy etc.) representing the minor axis of the ellipse representing the overlap of the two colliding nuclei. We can see from Fig.(6.2a) that the two histograms, are almost overlapping. This is interesting as we are considering here non-central collisions (with $b = 3 - 4$

fm). This shows that the momentum distributions and all fluctuations obtained from HIJING (without any momentum modification, i.e. $f_{p_x} = 1$) are isotropic. Any anisotropy will result from effects of particle interactions, primarily from collective flow effects, and we will represent it by using values of f_{p_x} different from 1. We mention here that the peak near 0.1 radians in Fig.(6.2) will represent fluctuations of size order 1 fm at the distance of about 10 fm representing the size of initial nuclei. As discussed in ref. [33], initial fluctuations are expected because of the nucleon size of order 1 fm (as well as quantum fluctuations in nucleon coordinates.) Such a peak thus may have useful information about the scale of fluctuations in the early stages of system evolution.

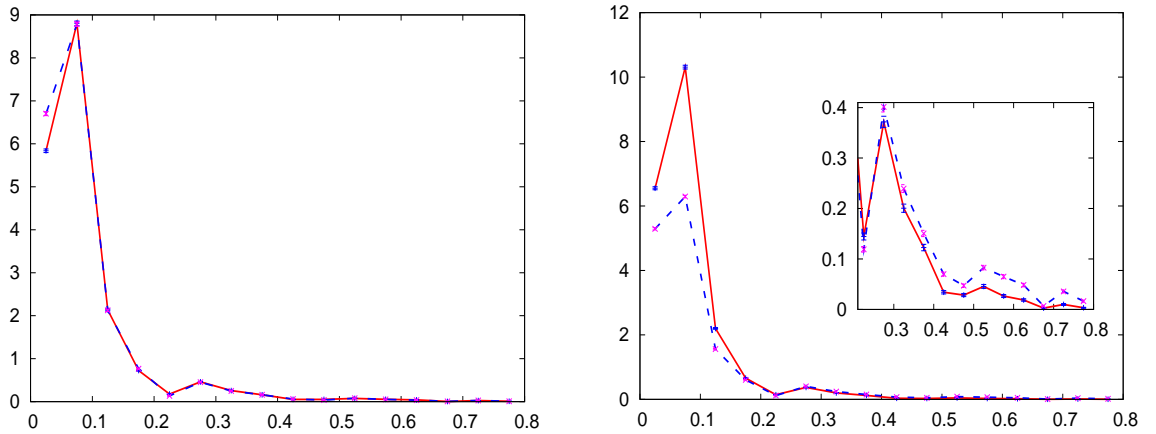


Figure 6.2:

(a) Plots of the histograms of the widths (in radians) of filled patches for $f_{p_x} = 1$. Smooth curves join the points which are marked with corresponding (\sqrt{N}) error bars. Distribution for widths at $\phi = 0$ ($\phi = \pi/2$) are shown by solid (dashed) plots. (b) Plots for the case with momentum modification, with $f_{p_x} = 1.2$. The inset in (b) shows the plots for larger widths.

We now consider an anisotropic momentum distribution by taking $f_{p_x} = 1.2$ to modify particle momentum distribution from HIJING. (Note that this is just to model the effects of flow.) Fig.(6.2b) shows the plots of distributions of widths for this case. We see that the distribution at $\phi = \pi/2$ is smaller than the distribution at $\phi = 0$ (beyond the error bars) for small widths while the situation is reversed for larger widths (as shown by the inset in Fig.(6.2b)). This is expected as the stretching of

fluctuation patches will be more significant at $\phi = \pi/2$ due to elliptic flow. Stretching makes fluctuation patches larger, hence the distribution for large widths is higher for $\phi = \pi/2$ than for $\phi = 0$. This is suitably compensated at smaller angles where $\phi = \pi/2$ distribution falls below the $\phi = 0$ distribution. We find that the ratio of the heights of the two peaks is directly related to the value of f_{p_x} representing the effects of elliptic flow. For $f_{p_x} = 1.1, 1.2, 1.3$, we find this ratio to be 1.3, 1.6, 2.0. Thus, the magnitude of elliptic flow can be probed directly with the comparison of the distributions of widths of fluctuation patches at $\phi = 0$ and at $\phi = \pi/2$. Hence this ratio of two peaks is an increasing function with centrality. However, for most peripheral collisions, there are discrepancies due to smaller number of statistics. Note that our modeling of flow in terms of a factor like f_{p_x} is ad hoc. Thus we do not try to derive any functional relationship between this factor and the ratios of the heights of the two peaks above (or try to give error bars for these etc.). Our purpose here is to show specific patterns of these distributions depending on momentum anisotropy. We also mention here that in actual hydrodynamic flow, the effect of flow on the momentum of particles will depend on the Y coordinate of the particle inside the plasma (in the event plane), being less important for larger Y values, as well as on the distance from the center. To more accurately represent the Y dependence of flow anisotropy, we have compared the $\phi = 0$ distribution using $f_{p_x} = 1.3$ with the $\phi = \pi/2$ distribution with $f_{p_x} = 1.1$. The difference between the two distributions is found to be closer to the difference obtained for the constant value of $f_{p_x} = 1.2$ for both the distributions. Since we are only interested in comparative changes in the two distributions, for simplicity, we will continue to use a constant value of f_{p_x} for determining the difference between the $\phi = 0$ and $\phi = \pi/2$ distributions.

6.4.1 Determination of Event Plane

As we have mentioned earlier, this analysis technique can be used to identify event plane event by event. To avoid statistical problem, a large number of events can be added up for controlled statistical errors. In Fig.(6.3) , we show a series of plots of widths distributions at $\phi = \phi_0$ (solid plot) and at $\phi = \phi_0 + \pi/2$ (dashed curve) for the angle $\phi_0 = 0, \pi/16, \pi/8, \pi/4$. We note that the ratio of the two peaks (solid curve and dashed curve) is largest for $\phi_0 = 0$ which represents the event plane. Thus, one needs

to simply plot the two width distributions at angles $\pi/2$ apart and keep changing the initial angle until the two distributions have maximum difference. This will identify the event plane. (Though we note that maximum overlap of the two distributions seems to happen at $\phi_0 = \pi/8$ and not at $\pi/4$ as one would have expected. This could be due to the large arc size of 45° used for calculating the individual distributions.) We have also compared the two distributions by varying the separation of ϕ at which they are evaluated. When the separation is larger than about $50\text{-}60^\circ$ the difference becomes almost similar up to 90° separation. With the physics of elliptic flow in view, we choose 90° separated distributions for comparison. Fig.(6.3) is shown with collection of data from 500 events each. One will need to do this on event-by-event basis to be able to identify the event plane in each case. Fig.(6.4) shows the same plots as in Fig.(6.3), but for single events. We see that statistical errors are larger for single events. For larger collision energies, statistical errors will be under better control. Also, one may arrive at the event plane by an iterative process. First one can roughly identify event planes for each event (as in Fig.(6.4)). Then a large number of events can be combined for each choice of ϕ_0 to maximize the difference between the two plots. This can be done by systematically changing the event plane for each event, until the all-event-sum histograms (as in Fig.(6.3)) lead to maximum difference between the two histograms.

6.5 Discussion

In this chapter we have shown that a shape/size analysis of excursion sets can lead to a completely new way of identifying the event plane in RHICE and to quantify the magnitude of flow anisotropies. This method is novel, and completely independent of other conventional methods. This technique can, thus, be used to cross-check the results obtained by other conventional techniques. Further, the entire distribution of sizes of excursion sets, as shown in Fig.(6.2), will contain valuable information about nature of fluctuations and that of anisotropic flow. Also the width distribution along the rapidity should provide information about the longitudinal scaling of fluctuations. These issues can be probed using hydrodynamic simulations. We mention here that anisotropic expansion of the universe was discussed in ref. [95] using Fourier transform

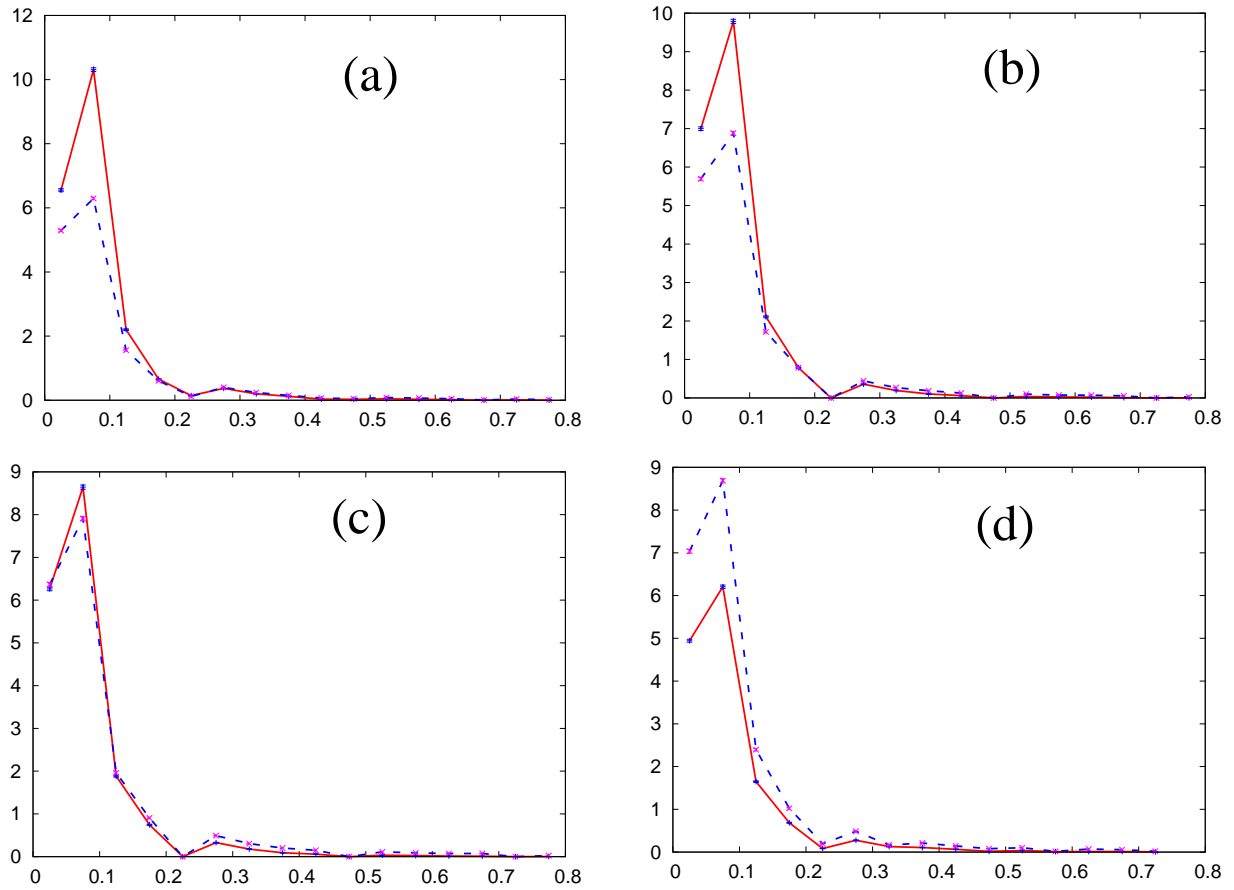


Figure 6.3:
 Plots of histograms (for 500 events each) at $\phi = \phi_0$ (solid curve) and at $\phi_0 + \pi/2$ (dashed curve) for $\phi_0 = 0$ (a), $\pi/16$ (b), $\pi/8$ (c), and $\pi/4$ (d).

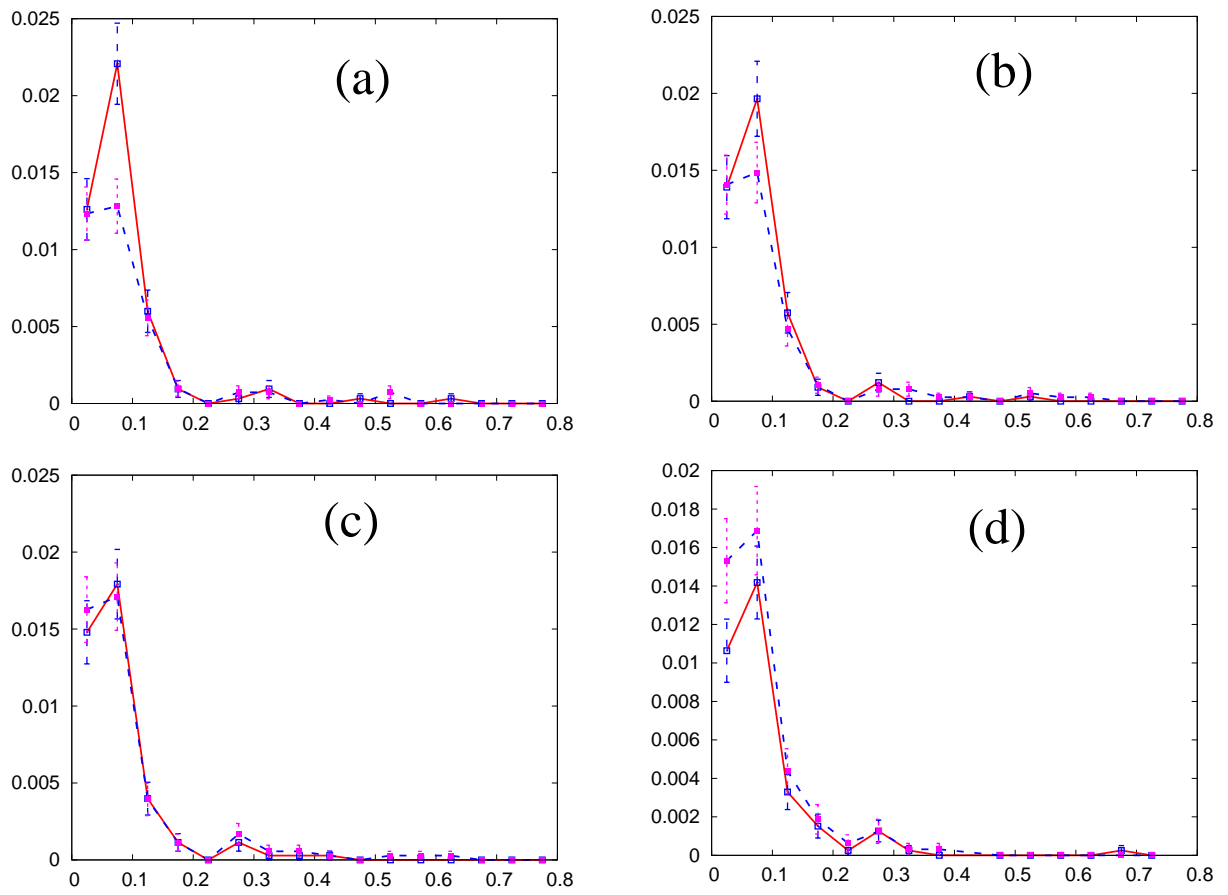


Figure 6.4:
Series of plots as in Fig.(6.3), for single event case each.

technique as well as direct shape analysis of excursion sets. Here we have used the direct shape analysis method for investigating flow anisotropy. It will be useful to also use Fourier transform technique for this purpose. Note that this technique will detect any effects present in the system which lead to anisotropy of momenta. For example the presence of initial strong magnetic field (as well as induced electric field) will lead to anisotropies [100, 101] and should leave imprints on these distributions of widths. Even the presence of any initial anisotropies of fluctuations, such as for deformed nuclei, could be detected in this method. Important issue then will be to distinguish any initial anisotropy (as from a deformed nucleus) from anisotropy resulting from anisotropic flow. In this respect this technique of direct shape analysis seems particularly effective, in comparison to, e.g. the Fourier transform technique, as discussed in detail in ref. [95].

Chapter 7

Summary

In this chapter we will give a brief summary and concluding remarks about the work done in this thesis. $Z(3)$ symmetry arises when one takes the expectation value of Polyakov loop as order parameter for confinement-deconfinement phase transition. $Z(3)$ symmetry is restored below T_c in the confined phase and spontaneously broken in the deconfined phase giving rise to 3 degenerate vacua. In this thesis, we have studied the numerical simulation of evolution of the topological defects i.e $Z(3)$ walls and strings produced in QGP phase in RHICE.

We have studied the confinement-deconfinement phase transition as a first order phase transition which is suitable for higher baryon chemical potential. Here the phase transition takes place due to the nucleation of QGP bubbles and the nucleation probability is very small, at most 5 bubbles are produced in a 20 fm region. We have seen atleast one or two domain walls produced in this case. Study of scattering of quarks from these walls is of interest because it will lead to enhancement of P_t and cp violation etc.

Since strong elliptic flow at RHIC hints towards early thermalisation of QGP state, it is better to view QCD phase transition as a quench rather than an equilibrium phase transition. We see the $Z(3)$ domains produced in this case are of the order of 2-3 fm. However, $Z(3)$ symmetry is explicitly broken giving rise to one true vacuum due to the presence of quarks. The metastable vacuum at $l = 0$ is shifted

little bit along $\theta = 0$ direction. Due to the shifted initial configuration, we don't find $Z(3)$ domains here. We also found that there is huge oscillations of field in this case, so we studied its effect on elliptic flow. We have compared two situations, elliptic flow in equilibrium and quench case. We see huge oscillation in flow anisotropy during quench transition.

Also, we found a surprising result during the quench transition, instead of rolling down of the field (as happens in spinodal decomposition), we see bubble like structure in this case. We don't expect bubble like structure here because there is no metastable barrier between true vacuum and false vacuum. We have studied some fixed potential (not varying with temperature) to understand this. Our current understanding is that these structures appear due to initial random configuration of the field as well as presence of ϕ^3 term in the potential.

Finally, we have studied a different analysis technique to measure the elliptic flow anisotropy. This technique analyzes shapes (sizes) of patches above (below) certain threshold value for transverse energy/particle number (the excursion sets) as a function of the azimuthal angle and rapidity. The histogram of size distribution of fluctuation patches near x-axis and y-axis gives the anisotropy factor. In noncentral collision, due to larger expansion along x-axis, the fluctuation patches which are at y-axis are stretched more. So, there is more large size patches near y axis compared to x axis and more small size patches near x axis compared to y axis.

Bibliography

- [1] E. Hubble, Proc. Natl. Acad. Sci. **15**, 168 (1929).
- [2] A.A. Penzias and R.W Wilson, Astrophys. **J** **142**, 419 (1965); R.H. Dicke, P.J.E. Peebles, P.G. Roll and D.T. Wilkinson, Astrophys. **J** **142**, 414 (1965).
- [3] For a review see, S. Sarkar, Rept. Prog. Phys. **59**, 1493 (1996).
- [4] For a review see, A. Vilenkin and E.P.S. Shellard, "Cosmic strings and other topological defects", (Cambridge University Press, Cambridge, 1994).
- [5] A.H. Guth, Phys. Rev. **D** **23**, 347 (1981).
- [6] S. Dodelson, "Modern Cosmology", (Academic Press, California, 2003).
- [7] H.B. Nielsen and P. Olesen, Nucl. Phys. **B** **61**, 45 (1973).
- [8] N.D. Mermin, Rev. Mod. Phys. **51**, 591 (1979).
- [9] T.W.B. Kibble, J. Phys. **A** **9**, 1387 (1976), Phys. Rep. **67**, 183 (1980).
- [10] W.H. Zurek, Nature **317**, 505 (1985); Phys. Rept. **276**, 177 (1996).
- [11] P.W. Higgs, Phys. Lett. **12**, 132 (1964); Phys. Rev. **L** **13**, 508 (1964); Phys. Rev. **145**, 1156 (1966).
- [12] D.J. Gross and F. Wilczek, Phys. Rev. Lett **30**, 1343, (1973); H.D. Politzer, Phys. Rev. Lett **30**, 1346 (1973).
- [13] T. Hatsuda and T. Kunihiro, Phys. Rept. **247**, 221 (1994); R. Rapp and J. Wambach, Adv. Nucl. Phys. **25**, 1 (2000).

- [14] Y. Aoki, Z. Fodor, S.D. Katz and K.K. Szabo, Phys. Lett. **B 643**, 46 (2006) ; F. Karsch, Lect. Notes Phys. **583**, 209 (2002); F. Karsch, E. Laermann, hep-lat/0305025.
- [15] J.B. Kogut et al., Phys. Rev. Lett. **50**, 393 (1983); M. Fukugita and A. Ukawa, Phys. Rev. Lett. **57**, 503 (1986); F. Karsch and E. Laermann, Phys. Rev. **D 50**, 6954 (1994); S. Aoki et al., Phys. Rev. **D 57**, 3910 (1998); C. Gattringer, P.E. Rakow, A. Schafer and W. Soldner, Phys. Rev. **D 66**, 054502 (2002).
- [16] F. Karsch, E. Laermann and A. Peikert, Nucl. Phys. **B 605**, 579 (2001).
- [17] C.R. Allton et al., Phys. Rev. **D 66**, 074507 (2002).
- [18] J.W. Harris and B. Muller, Ann. Rev. Nucl. Part. Sci. **46**, 71 (1996), B. Muller and J.L. Nagle, Ann. Rev. Nucl. Part. Sci. **56**, 93 (2006).
- [19] Z. Fodor and S.D. Katz, JHEP **0404**, 050 (2004); JHEP **0203**, 014 (2002).
- [20] K. Rajagopal, Comments Nucl. Part. Phys. **A2**, 120 (2002); [arXiv:hep-ph/0009058].
- [21] L.V. Gribov, E.M. Levin, and M.G. Ryskin, Phys. Rept. **100**, 1 (1983).
- [22] A.H. Mueller and J.W. Qiu, Nucl. Phys. **B 268**, 427 (1986).
- [23] L.D. McLerran and R. Venugopalan, Phys. Rev. **D 49**, 2233 (1994).
- [24] Y.V. Kovchegov and A.H. Mueller, Nucl. Phys. **B 529**, 451 (1998).
- [25] R. Glauber and G. Mattaie, Nucl. Phys. **B 21**, 135 (1970); G.-Y. Qin, H. Petersen, S.A. Bass, and B. Muller, Phys. Rev. **C 82**, 064903 (2010).
- [26] J. Kapusta, P. Lichard and D. Siebert, Nucl. Phys. **A 544**, 485 (1992); P.V. Ruuskanen, Nucl. Phys. **A 544**, 169 (1992).
- [27] K. Geiger, Phys. Rept. **258**, 237 (1995).
- [28] D. Molnar and M. Gyulassy, Phys. Rev. **C 62**, 054907 (2000).
- [29] H.T. Elze and U. Heinz, Phys. Rep. **183**, 81 (1989).

- [30] P.F. Kolb and U. Heinz, arXiv:0305084
- [31] J.D. Bjorken, Phys. Rev. **D 27**, 140 (1983).
- [32] J.-Y. Ollitrault, Phys. Rev. **D 46**, 229 (1992).
- [33] A.P. Mishra et al., Phys. Rev. **C 77**, 064902 (2008); Phys. Rev. **C 81**, 034903 (2010).
- [34] R.K. Mohapatra, P.S. Saumia and A.M. Srivastava, Mod. Phys. Lett. **A 27** 1250168 (2012).
- [35] B. Alver et al., Phys. Rev. Lett.**98**, 242302 (2007).
- [36] C. Adler et al., STAR Collaboration, Phys. Rev. **C 66**, 034904 (2002); D. Molnar and S.A. Voloshin, Phys. Rev. Lett. **91**, 092301 (2003); S.A. Voloshin, Nucl. Phys. **A 715**, 379 (2003).
- [37] T. Matsui and H. Satz, Phys. Lett. **B 178**, 416 (1986).
- [38] B. Abelev et al., ALICE Collaboration, Phys. Rev. Lett. **109**, 072301 (2012).
- [39] M. Gyulassy, Nucl. Phys. **B 661**, 637 (1999); Nucl. Phys. **B 571**, 197 (2000).
- [40] J. Rafelski and B. Muller, Phys. Rev. Lett **48**, 1066 (1982) [Erratum-ibid. 56, 2334 (1986).]
- [41] U. S. Gupta, R. K. Mohapatra, A. M. Srivastava and V. K. Tiwari, Phys. Rev.**D 82**, 074020 (2010).
- [42] R.K.Mohapatra and A.M.Srivastava; arXiv:1210.4718.
- [43] S. Digal and R.K. Mohapatra, preprint in preparation
- [44] S. Coleman, Phys. Rev. **D 15**, 2929 (1977); I. Yu. Kobzarev, L.B. Okun and M.B. Voloshin, Sov. Jrnl. Nucl. Phys.**20**, 644 (1975).
- [45] A.D. Linde Nucl. Phys. **B 216**, 421 (1983).
- [46] C.G. Callan and S. Coleman, Phys. Rev. **D 16**, 1762 (1977).

- [47] S.L. Glashow, Nucl. Phys. **22**, 579 (1961); S. Weinberg, Phys. Rev. **L 19**, 1264 (1967); A. Salam, Elementary Particle Physics, (Stockholm: Almquist and Wiksells) Page 367
- [48] Ta-Pei Cheng and Ling-Fong Li, "Gauge Theory of Elementary Particle Physics", (Oxford University Press, Oxford, 1984).
- [49] G.t Hooft, Nucl. Phys. **B 138**, 1 (1978); *ibid.*153, 141, (1979).
- [50] D.J. Gross, R.D. Pisarski and L.G. Yaffe, Rev. Mod. Phys. **53**, 43 (1981); K. Holland and Uwe-jens Wiese, hep-ph/0011193; R.D. Pisarski, hep-ph/0203271; N. Weiss, hep-ph/9311233.
- [51] A.M. Polyakov, Phys. Lett. **B 72**, 477 (1978).
- [52] L. Susskind, Phys. Rev. **D 20**, 2610 (1979).
- [53] L. D. McLerran and B. Svetitsky, Phys. Rev.**D 24**, 450 (1981).
- [54] B. Svetitsky, Phys. Rep. **132** , 1 (1986).
- [55] T. Bhattacharya, A. Gocksch, C. K. Altes, and R. D. Pisarski, Nucl. Phys. **B 383**, 497 (1992); J. Boorstein and D. Kutasov, Phys. Rev. **D 51**, 7111 (1995).
- [56] A. V. Smilga, Ann. Phys. **234**, 1 (1994).
- [57] V.M. Belyaev, Ian I. Kogan, G.W. Semenoff, and N. Weiss, Phys. Lett. **B 277**, 331 (1992).
- [58] C.P. Korthals Altes, hep-th/9402028
- [59] R.D. Pisarski, Phys. Rev. **D 62**, 111501R (2000); *ibid*, hep-ph/0101168.
- [60] A. Dumitru and R.D. Pisarski, Phys. Lett. **B 504**, 282 (2001); Phys. Rev. **D 66**, 096003 (2002); Nucl. Phys. **A 698**, 444 (2002).
- [61] A. Dumitru, D. Roder, and J. Ruppert, Phys. Rev. **D 70**, 074001 (2004).
- [62] A.P. Mishra, A.M. Srivastava, and V.K. Tiwari, Indian J. Phys. **B85**, 1161 (2011).

- [63] B. Layek, A.P. Mishra, A.M. Srivastava, and V.K. Tiwari, Phys. Rev. **D 73**, 103514 (2006).
- [64] O. Scavenius, A. Dumitru and J.T. Lenaghan, Phys. Rev. **C 66**, 034903 (2002).
- [65] G. Boyd, J. Engels, F. Karsch, E. Laermann, C. Legeland, M. Lutgemeier, and B. Petersson, Nucl. Phys. **B 469**, 419 (1996); M. Okamoto et al., Phys. Rev. **D 60**, 094510 (1999).
- [66] A.M. Srivastava Phys. Rev. **D 45**, R3304 (1992); Phys. Rev. **D 46**, 1353 (1992); S. Chakravarty A.M. Srivastava Nucl. Phys. **B 406**,795 (1993).
- [67] J. S. Langer, Ann. Phys. (N. Y.)**54**, 258 (1969); J. S. Langer and L. A. Turski, Phys. Rev. **A 8**, 3230, (1973); L. A. Turski and J. S. Langer, Phys. Rev. **A 22**, 2189 (1980)
- [68] L. P. Csernai and J. I. Kapusta, Phys. Rev. **D 46**, 1379 (1992).
- [69] J.I. Kapusta, A.P. Vischer, and R. Venugopalan, Phys. Rev. **C 51**, 901 (1995)
- [70] P. Danielewicz, Phys. Lett. **146 B**, 168 (1984)
- [71] J. Ignatius, K. Kajantie, and K. Rummukainen, Phys. Rev. Lett. **68**, 737 (1992); V. Dixit and M.C. Ogilvie, Phys. Lett. **B 269**, 353 (1991).
- [72] J. Adams et al. [STAR Collaboration], J. Phys. **G32**, L37,(2006) [arXiv:nucl-ex/0509030]; J.Putschke, Talk at Quark Matter 2006 for STAR collaboration), Shanghai, Nov.2006; S. A. Voloshin, Phys. Lett. **B632**, 490 (2006)[arXiv:nucl-th/0312065].
- [73] A. Dumitru, F. Gelis, L. McLerran, and R. Venugopalan, Nucl. Phys. **A 810**, 91 (2008).
- [74] E. Witten, Phys. Rev. **D 30**, 272 (1984).
- [75] S. Digal, A.M. Srivastava, Phys. Rev. Lett. **80**, 1841 (1998).
- [76] U. S. Gupta, R. K. Mohapatra, A. M. srivastava and V. K. Tiwari, arXiv:1112.1177.

- [77] K. Fukushima, *Phys. Lett.* **B 591** 277 (2004), arXiv:hep-ph/031012; S. Rosner, C. Ratti, and W. Weise, *Phys. Rev.* **D 75** 034007 (2007), arXiv: hep-ph/0609281.
- [78] J.H. Traschen and R.H. Brandenberger, *Phys. Rev.* **D 42**, 2491 (1990); Y. Shtanov, J. Traschen, and R. Brandenberger, *Phys. Rev.* **D 51**, 5438 (1995); L. Kofman, A. Linde, and A.A. Starobinsky, *Phys. Rev.* **D 56**, 3258 (1997).
- [79] A. Atreya, A. Sarkar, and A.M. Srivastava, *Phys. Rev.* **D 85**, 014009 (2012).
- [80] M. Asakawa, S.A. Bass, and B. Muller, arXiv: 1208.2426.
- [81] M. Deka, S. Digal, and A.P. Mishra, arXiv:1009.0739.
- [82] A. Bazavov, B.A. Berg, and A. Dumitru, *Phys. Rev.* **D 78**, 034024 (2008).
- [83] B. Layek, A.P. Mishra, A.M. Srivastava, *Phys. Rev.* **D 71**, 074015 (2005).
- [84] J.-Y. Ollitrault, *Eur. J. Phys.* **29**, 275 (2008); R. S. Bhalerao, J. P. Blaizot, N. Borghini, and J.-Y. Ollitrault, *Phys. Lett.* **B 627**, 49 (2005).
- [85] P.F. Kolb, J. Sollfrank, and U. Heinz, *Phys. Rev.* **C 62**, 054909 (2000).
- [86] Z. Fodor, *Proc. Sci.* 42, LATT2007 (2007) 011; F. Karsch, *Proc. Sci.* 42, LATT2007 (2007) 015.
- [87] O. Scavenius, A. Dumitru and A. D. Jackson, *Phys. Rev. Lett.* **87**, 182302 (2001).
- [88] J. Harris, F. Laue, J. Reid, S. Panitkin, and N. Xu, Talks given at Quark Matter 2001, Jan. 14th – 20th, 2001, Stony Brook, New York; <http://www.rhic.bnl.gov/qm2001>.
- [89] J. Rafelski and J. Letessier, *Phys. Rev. Lett.* **85**, 4695 (2000).
- [90] J. Randrup, *Phys. Rev. Lett.* **92**, 122301 (2001).
- [91] L. P. Csernai and I. N. Mishustin, *Phys. Rev. Lett.* **74**, 5005 (1995).
- [92] O. Scavenius and A. Dumitru, *Phys. Rev. Lett.* **83**, 4697 (1999); O. Scavenius, A. Dumitru, E. S. Fraga, J. T. Lenaghan and A. D. Jackson, *Phys. Rev.* **D 63**, 116003 (2001).

- [93] P. Shukla and A. K. Mohanty, Phys. Rev. **C 64**, 054910 (2001).
- [94] K Rajagopal and F Wilczek, Nucl. Phys. **B 404**, 577 (1993).
- [95] R. K. Mohapatra, P. S. Saumia, and A. M. Srivastava, Int.J.Mod.Phys. **A 27** 1250144 (2012).
- [96] A. M. Poskanzer and S. A. Voloshin, Phys. Rev. **C 58**, 1671 (1998).
- [97] S. Wang et al., Phys. Rev. **C 44**, 1091 (1991).
- [98] N. Borghini, P. M. Dinh and J. Y. Ollitrault, Phys. Rev. **C 64**, 054901 (2001).
- [99] M. Gyulassy, D. H. Rischke, and B. Zhang, Nucl. Phys. **A 613**, 397 (1997).
- [100] R. K. Mohapatra, P. S. Saumia, and A. M. Srivastava, Mod. Phys. Lett. **A 26** 2477 (2011).
- [101] K. Tuchin, arXiv:1108.4394.